Simulating Electronically Nonadiabatic Dynamics and Spectroscopy via Quantum Master Equations That Treats Off-Diagonal Electronic Coupling Perturbatively

by

Yifan Lai

A dissertation submitted in partial fulfillment
of the requirements for the degree of
Doctor of Philosophy
(Chemistry and Scientific Computing)
in the University of Michigan
2022

Doctoral Committee:

Professor Eitan Geva, Chair
Professor Emanuel Gull
Professor Kevin Kubarych
Professor Dominika Zgid

Yifan Lai
laiyifan@umich.edu
ORCID iD: 0000-0002-1005-2512

© Yifan Lai 2022

DEDICATION

To my family, for their love and support.

ACKNOWLEDGMENTS

First and foremost, this dissertation would not be possible without the help and support of Prof. Eitan Geva. His patience and mentorship has been invaluable throughout my degree, allowing me to navigate the long and trying process of pursuing a Ph.D, and to grow both academically and as a scientist. I would also like to thank my committee, Prof. Dominika Zgid, Prof. Kevin Kubarych, and Prof. Emanuel Gull, who have provided helpful insight during this endeavor. Additionally, I would thank my mentors at UC Santa Barbara, Prof. Donald Aue and Prof. Norbert Reich, for inspiring me to pursue theoretical chemistry.

I would like to thank my fellow Geva lab members, both past and present: Dr. Alexander Schubert, Prof. Xiang Sun, Dr. Kyle Williams, Dr. Ellen Mulvihill, Miriam Lenn, Dalia Hassan, Prof. Xing Gao, Yudan Liu, and Dr. Max Saller. Xiang introduced me to FGR and LSC when I first started graduate school, much of the research here would not have been possible without him. Alex gave me invaluable help on working with MCTDH, which turns out to be one of the most important tool for my research. I have enjoyed working with Xing on the simulation of spectroscopy, his talent and hard work played an important role in the project. Yudan has always been a happy presence in the lab, we cooperated briefly on the LSC/SQC project. I am currently working with Max on the cavity project, the many conversations we had about research has always been a source of valuable insight. I was fortunate to have joined in the Compute-to-Learn chemistry education project, where Ellen and Kyle laid most of the foundation. The many Compute-to-Learn workshops I oversaw with Ellen was also a valuable learning experience for myself, for her passion and knowledge inspired me deeply. Miriam and Dalia will be in charge of Compute-to-Learn in the coming years, their immense effort pushed the project forward in the trying time of COVID. I would additionally like to thank Blair Winograd and Alicia Welden for their contributions to the Compute-to-Learn project, and Yanbin Zhou for joining the project in times of dire need.

I would like to express my deepest gratitude to my extended family, for inspiring me to walk the path of science. To my mom, for her love and patience, and for always believing in my abilities. To my dad, for the many life lessons that I cannot even begin to enumerate.

TABLE OF CONTENTS

DEDICATION ii

ACKNOWLEDGMENTS iii

LIST OF FIGURES vi

LIST OF TABLES viii

LIST OF APPENDICES ix

ABSTRACT x

CHAPTER

1 Introduction 1

1.1 Motivation for a Perturbative Reduced Dynamics Method 1
1.2 Quantum Master Equations 4
1.3 Overview of the Dissertation 7

2 Simulating the Reduced Electronic Dynamics via Off-Diagonal Quantum Master Equation 8

2.1 Introduction 8
2.2 Full Density Matrix Off-Diagonal Quantum Master Equation 9
2.3 Population Dynamics Off-Diagonal Quantum Master Equation 10
2.4 The Garg-Onuchic-Ambegaokar Model 12
2.5 Results and Discussion 15
2.6 Concluding Remarks 23

3 Simulating Electronic Absorption Spectrum via Off-Diagonal Quantum Master Equation 24

3.1 Introduction 24
3.2 Molecular Aggregate Hamiltonian and the Simulation of Absorption Spectra . . . 25
3.3 Model Parameters and Method Details 27
3.4 Absorption Spectra 28
3.5 Concluding Remarks 31

4 An Efficient Approach for Calculating Cavity-Enhanced Charge Transfer Rate Constants 33

4.1 Introduction . . . 33
4.2 Model Hamiltonian . . . 34
4.3 Cavity-Enhanced Fermi's Golden Rule Charge Transfer Rate Constant . . . 35
4.4 Concluding Remarks . . . 38

5 Computational Study of Charge-Transfer Dynamics in the Carotenoid–Porphyrin–C_{60} Molecular Triad Solvated in Explicit Tetrahydrofuran . . . 40

5.1 Introduction . . . 40
5.2 Theory . . . 41
5.3 Molecular Model . . . 44
5.4 MD Simulations . . . 48
5.5 Results . . . 48
5.6 Concluding Remarks . . . 54

6 Conclusion . . . 55

6.1 Summary . . . 55
6.2 Outlook . . . 56

APPENDICES . . . 58

BIBLIOGRAPHY . . . 68

LIST OF FIGURES

FIGURE

2.1 Electronic population difference (top row) and coherence (bottom row) as a function of time obtained using f-TNL-OD-QME, p-TNL-OD-QME, f-TL-OD-QME, p-TL-OD-QME for the GOA model with $\Gamma = \{0.01, 0.1, 0.2, 1.0\}$. See Table.2.2 for the values of other parameters. Also shown are numerically exact MCTDH-based results. 16

2.2 Electronic population difference as a function of time obtained using f-TNL-OD-QME, p-TNL-OD-QME, f-TL-OD-QME and p-TL-OD-QME, with $|\omega_{\rm DA}| = \{0.0, 0.1, 0.2, E_r, 0.5, 1.0\}$. See Table.2.2 for the values of other parameters. Also shown are numerically exact MCTDH-based results. 17

2.3 Electronic population difference (top three rows) as a function of time obtained using f-TNL-OD-QME, p-TNL-OD-QME, f-TL-OD-QME and p-TL-OD-QME, for the GOA model with $\beta = \{\infty, 5, 1\}$ and $\omega_{\rm DA} = \{0.0, E_r\}$. See Table.2.2 for the values of the other parameters. The bottom row shows the coherence for the case of $\beta = 1$. Also shown are numerically exact MCTDH-based results. 18

2.4 $\langle \hat{V}_{ij}(t) \rangle$ and $\langle \hat{V}_{ij}(t)\hat{V}_{kl}(\tau) \rangle$ as a function of t and $(t, t-\tau)$, respectively, where $i, j, k, l \in \{D, A\}$, for the GOA model with $\beta = \{5, 2, 1\}$. See Table.2.2 for the values of other parameters. The intensity stands for the modulus, while the hue stands for the phase. The values are normalized so that $\langle \hat{V}_{ij}(0) \rangle = \langle \hat{V}_{ij}(0)\hat{V}_{kl}(0) \rangle = 1$. The diagonal line represents $\tau = 0$, and the lower triangle portion is set to zero by definition. 19

2.5 Electronic population difference as a function of time obtained using f-TNL-OD-QME, p-TNL-OD-QME, f-TL-OD-QME and p-TL-OD-QME, with $y_0 = \{0.25, 0.75, 1.5\}$ and $\beta = 1$. See Table. 2.2 for the values of other parameters. Also shown are numerically exact MCTDH-based results. 20

2.6 $\langle \hat{V}_{ij}(t) \rangle$ and $\langle \hat{V}_{ij}(t)\hat{V}_{kl}(\tau) \rangle$ as a function of t and $(t, t-\tau)$, respectively, where $i, j, k, l \in \{D, A\}$, for the GOA model with $\beta = 1$ and $y_0 = \{1.5, 0.75, 0.25\}$. See Table.2.2 for the values of other parameters. The intensity stands for the modulus, while the hue stands for the phase. The values are normalized so that $\langle \hat{V}_{ij}(0) \rangle = \langle \hat{V}_{ij}(0)\hat{V}_{kl}(0) \rangle = 1$. The diagonal line represents $\tau = 0$, and the lower triangle portion is set to zero by definition. 21

2.7 Schrödinger picture coherences as a function of time obtained by applying Eq. 1.14a and its time convolutionless counterparts to the f-TNL-OD-QME (left column) or p-TNL-OD-QME (right column) with $\beta = \{\infty, 1\}$. See Table.2.2 for the values of other parameters. Also shown are numerically exact MCTDH-based results. 22

3.1 The absorption spectra for the slow bath and low temperature case ($\omega_c = 18\text{cm}^{-1}, T = 72\,\text{K}$). The reduced dynamics is obtained using one of three QMEs, or the numerically exact HEOM. From top row to bottom row, in order: $\Gamma = 5\ \text{cm}^{-1}$, $\Gamma = 25\ \text{cm}^{-1}$, and $\Gamma = 100\ \text{cm}^{-1}$; from left column to right column, in order: $\lambda = 10\ \text{cm}^{-1}$, $\lambda = 100\ \text{cm}^{-1}$, and $\lambda = 1000\ \text{cm}^{-1}$. The spectra are calculated without re-normalization. . 28
3.2 The absorption spectra for the fast bath and low temperature case ($\omega_c = 200\ \text{cm}^{-1}$, $T = 72\ \text{K}$). The reduced dynamics is obtained using one of three QMEs, or the numerically exact HEOM. From top row to bottom row, in order: $\Gamma = 5\ \text{cm}^{-1}$, $\Gamma = 25\ \text{cm}^{-1}$, and $\Gamma = 100\ \text{cm}^{-1}$; from left column to right column, in order: $\lambda = 10\ \text{cm}^{-1}$, $\lambda = 100\ \text{cm}^{-1}$, and $\lambda = 1000\ \text{cm}^{-1}$. The spectra are calculated without re-normalization. 29
3.3 The absorption spectra for the fast bath and high temperature case ($\omega_c = 200\ \text{cm}^{-1}$, $T = 300\ \text{K}$). The reduced dynamics is obtained using one of three QMEs, or the numerically exact HEOM. From top row to bottom row, in order: $\Gamma = 5\ \text{cm}^{-1}$, $\Gamma = 25\ \text{cm}^{-1}$, and $\Gamma = 100\ \text{cm}^{-1}$; from left column to right column, in order: $\lambda = 10\ \text{cm}^{-1}$, $\lambda = 100\ \text{cm}^{-1}$, and $\lambda = 1000\ \text{cm}^{-1}$. The spectra are calculated without re-normalization. 30

4.1 Cavity-enhanced Fermi's golden rule CT rate constants for (left) Model I and (right) Model II, compared to the cavity-free rates. 38

5.1 Schematic view of the relationship between the average donor–acceptor energy gap, $\langle U \rangle_D^{\text{Cl,eq}}$, the reorganization energy, E_r, and the reaction free energy, ΔE, in the normal (upper panel) and inverted (lower panel) regions (see Eq. 5.9). 45
5.2 Molecular structure of the linear (A) and bent (B) conformations of the carotenoid–porphyrin–C_{60} molecular triad solvated in liquid THF. The triad is in ball-and-stick representation; the carbon, oxygen, and nitrogen atoms are in gray, red, and blue, respectively. For visibility, the hydrogen atoms are not shown and solvent THF molecules within 20 Å of the triad are shown. The figure was generated using Visual Molecular Dynamics (VMD) package. 46
5.3 Comparison between the probability densities (black) of the donor–acceptor energy gaps, U, and the corresponding Gaussian approximations (red), for the flexible (upper panels) and rigid (lower panels) bent conformation. 51
5.4 Comparison between the probability densities (black) of the donor–acceptor energy gaps, U, and the corresponding Gaussian approximations (red), for the flexible (upper panels) and rigid (lower panels) linear conformation. 52

LIST OF TABLES

TABLE

2.1 Shorthands for the four types of OD-QMEs under consideration in the current dissertation 9
2.2 GOA model parameters (in atomic units) 15

4.1 Field mode frequency and light-matter coupling parameters for two CT in cavity Hamiltonians under consideration. 35

5.1 Donor-to-Acceptor rate constants for the triad in the bent conformation 49
5.2 Donor-to-Acceptor rate constants for the triad in the linear conformation 49
5.3 Squared electronic coupling coefficients (Γ_{DA}^2), average ($\langle U \rangle_D^{\mathrm{Cl,eq}}$) and variance ($(\sigma_D^{\mathrm{Cl,eq}})^2$ (eV^2)) of Donor-Acceptor energy gap, reorganization energy (E_r), reaction free energy (ΔE), and activation energy (E_A) for a flexible triad in the bent conformation 51
5.4 Squared electronic coupling coefficients (Γ_{DA}^2), average ($\langle U \rangle_D^{\mathrm{Cl,eq}}$) and variance ($(\sigma_D^{\mathrm{Cl,eq}})^2$ (eV^2)) of Donor-Acceptor energy gap, reorganization energy (E_r), reaction free energy (ΔE), and activation energy (E_A) for a rigid triad in the bent conformation 52
5.5 Squared electronic coupling coefficients (Γ_{DA}^2), average ($\langle U \rangle_D^{\mathrm{Cl,eq}}$) and variance ($(\sigma_D^{\mathrm{Cl,eq}})^2$ (eV^2)) of Donor-Acceptor energy gap, reorganization energy (E_r), reaction free energy (ΔE), and activation energy (E_A) for a flexible triad in the linear conformation 53
5.6 Squared electronic coupling coefficients (Γ_{DA}^2), average ($\langle U \rangle_D^{\mathrm{Cl,eq}}$) and variance ($(\sigma_D^{\mathrm{Cl,eq}})^2$ (eV^2)) of Donor-Acceptor energy gap, reorganization energy (E_r), reaction free energy (ΔE), and activation energy (E_A) for a rigid triad in the linear conformation 53

LIST OF APPENDICES

A Evaluation of the bath correlation functions for the spin-boson model 58

B Bath discretization procedure 62

C The 4th-order Runge-Kutta algorithm for solving TNL-OD-QMEs 64

D Dynamics in the rotating frame 66

ABSTRACT

The simulation of electronically nonadiabatic dynamics and spectroscopy remains as a central challenge in computational chemistry. Amongst the reduced dynamic methods, various forms of the perturbative quantum master equation (QME) including Fermi's golden rule (FGR), Redfield equation, and Marcus theory enjoy widespread use for their efficiency in the perturbative regime, and provides important physical intuition for the underlying dynamics.

In the first chapter of this dissertation, the accuracy of various QMEs that treat off-diagonal electronic coupling perturbatively (OD-QME) will be examined on a spin-boson model. OD-QME works in the interaction picture, limiting its application to population dynamics. A novel way of retrieving Schrodinger picture coherences from interaction picture dynamics will be introduced, and the resulting dynamics will be compared against the numerically exact multi-configuration time dependent Hartree method. It will be shown that OD-QME can generate accurate population and coherence in appropriate parameter ranges, and that the time-nonlocal QME is more accurate than time-local QME, especially if the QME uses a population only projection.

In the second chapter, the aforementioned method of calculating electronic coherence via OD-QME is applied to the simulation of absorption spectra. The result will be compared against the numerically exact hierarchical equations of motion, as well as the Redfield time-local QME which is widely applied in the context of spectroscopy. It will be shown that OD-QME exhibits comparable accuracy to Redfield QME over a wide parameter range. Both QMEs fail to predict the spectra accurately in the case of a high-frequency bath at a low temperature, and this error is likely to be linked to the quantum behavior of the bath.

In the third chapter, the FGR rates of electronically nonadiabatic reactions enhanced by a micro-cavity is calculated. It will be shown that the cavity-enhanced reaction rates can be evaluated from the cavity-free FGR correlation function with minimum additional effort, and this method will be applied to a model CT reaction. While a high-frequency cavity enhances reactions in the Marcus inverted region selectively, a low-frequency cavity enhances reactions in all regions uniformly.

In the fourth chapter, the FGR charge transfer rate constants for a molecular triad system solvated in explicit solvent is calculated via linear semiclassical (LSC) approach. A Marcus-like expression can be derived after applying a hierarchy of approximations. The validity of such approximations will be confirmed for the triad model. It will also be shown that the charge transfer

rate depends deeply on the conformation of the molecule, the fluctuation between which is the rate-limiting step of the charge transfer.

CHAPTER 1

Introduction

1.1 Motivation for a Perturbative Reduced Dynamics Method

Defined in the broadest sense, chemical dynamics is the study of particle, charge, and energy transfer processes in molecular systems. Quantum dynamical effects play an important role for both the electronic and the nuclear degrees of freedom (DOF),[1–3] hence the only way to obtain the exact dynamics is to treat all DOF fully quantum mechanically.

The well-known time dependent Schrödinger equation is the equation of motion (EOM) for a ket vector $|\Psi(t)\rangle$ in the Hilbert space. It is however inadequate for many relevant systems because they are *open systems*. A system being open, as opposed to being *closed*, means that it is coupled to an outside environment, or in other words, a sub-system of a closed overall system.

The state of an open system can be represented by a density operator $\hat{\rho}(t)$ which is equivalent to a vector in Liouville space. A density operator takes the general form $\hat{\rho}(t) = \sum_{jk} \rho_{jk}(t)|\psi_j\rangle\langle\psi_k|$ where $\{|\psi_j\rangle\}$ is an orthonormal basis spanning the Hilbert space, and the density operator is represented by a *density matrix* in that basis, with its jk-th element given by $\rho_{jk}(t)$. Density operators have several properties: A) The trace of the density operator is unity $\mathrm{Tr}[\hat{\rho}] = \sum_j \rho_{jj} = 1$; B) All populations (the diagonal elements of the density matrix) are positive $\rho_{jj} \geq 0$; C) The density operator is hermitian $\hat{\rho}^\dagger = \hat{\rho}$.

The dynamics of a density operator is described by the Liouville equation

$$\frac{\mathrm{d}}{\mathrm{d}t}\hat{\rho}(t) = -\frac{i}{\hbar}\Big[\hat{H}, \hat{\rho}\Big] = -\frac{i}{\hbar}\mathcal{L}\hat{\rho}\,, \tag{1.1}$$

where $\mathcal{L}$ is the Liouvillian superoperator (throughout this thesis, superoperators will be symbolized by calligraphic letters $\mathcal{A}, \mathcal{B}, \cdots$, whereas ordinary operators by carets $\hat{A}, \hat{B}, \cdots$). To obtain the expectation value of an observable $\hat{O}$, a trace is performed $\langle O\rangle(t) = \mathrm{Tr}[\hat{\rho}(t)\hat{O}]$.

A pure state $|\Psi(t)\rangle$ also corresponds to a density operator of the form $\hat{\rho}(t) = |\Psi(t)\rangle\langle\Psi(t)|$, which has the special property of being idempotent $\hat{\rho}\hat{\rho} = \hat{\rho}$. The pure state has otherwise the

same properties as a generic density operator, and the Schrödinger equation is a special case of the Liouville equation.

In the current dissertation, we focus on observables that only depends on the electronic DOF. Such observables are used to describe such processes as electronic relaxation, exciton transfer, and charge transfer, which are central to many technologically and biologically relevant processes such as photovoltaics and photosynthesis. The expectation value of such an observable $\hat{O}_e$ can be simplified into

$$\langle O_e \rangle(t) = \mathrm{Tr}_e\Big[\mathrm{Tr}_N[\hat{\rho}(t)]\hat{O}_e\Big] = \mathrm{Tr}_e\Big[\hat{\sigma}(t)\hat{O}_e\Big] \,, \tag{1.2}$$

where $\mathrm{Tr}_e[\cdot]$ ($\mathrm{Tr}_N[\cdot]$) are the trace over electronic (nuclear) DOF, and $\hat{\sigma} = \mathrm{Tr}_N[\hat{\rho}]$ is the reduced electronic density operator.

Although $\hat{\sigma}(t)$ describes dynamics involving only the electronic DOF, its dynamics is still impacted by the system's non-electronic DOF coupled to it. The cost of simulating the dynamics of the entire systems (electronic and non-electronic DOF) scales exponentially with the number of DOF, thus fully quantum mechanical simulation is only possible for a small subset of models that are of limited sizes or take specific forms,[4–8] and is generally infeasible for realistic molecular Hamiltonians.

A popular strategy for tackling this scaling challenge is to treat the relevant electronic DOFs (also referred to as the *system* DOF) as an open system, and restrict the treatment of the remaining DOFs (also referred to as the *bath* DOF) to the minimum necessary in order to account for their effect on the electronic dynamics. (For the rest of this dissertation we will use "electronic (nuclear) DOF" and "system (bath) DOF" interchangeably.) Such approaches include mixed quantum-classical and semiclassical methods that treat the bath DOF at a more approximate, and thereby more cost-effective, level[9–42] and methods based on performing *reduced* dynamics in the space of system DOFs only, formulating the input on the bath DOF necessary in order to account for their effect on the reduced dynamics in terms of compact quantities such as time correlation functions, spectral densities, memory and friction kernels, and influence functionals.[1,1,43–50,50–74]

Projection-based methods provide a general framework for formulating reduced dynamics. Through the use of a projection superoperator, the overall density operator is projected onto a subspace that effectively eliminates the dynamics of bath DOF, the propagation is then performed for the projected state, which would only include information about the electronic dynamics. The effect of the bath DOF on the dynamics of the electronic DOF of interest in terms of compact reduced quantities such as memory kernels, population relaxation and dephasing rate coefficients, etc. Different types of projection-based methods have been proposed over the years. On the highest end in terms of approximations, the time-nonlocal (TNL) Nakajima-Zwanzig generalized quantum master equation (GQME)[61–68,71,72,75–85] and its time-local (TL, also referred to as time convolution-less in some contexts) analogue[86–89] provide formally exact EOM for the projected state. However,

calculating the GQME memory kernel requires performing dynamics in the overall (system + bath) space, which again relies somewhat on either costly exact methods, or approximate quasi-classical methods. Still, GQME tends to out-perform the underlying dynamics methods used to calculate its inputs, because the memory kernel tends to vanish on a timescale smaller than the sought-after dynamics.

Quantum master equations (QMEs) is a perturbative approach to the projection-based dynamics, where the Hamiltonian $\hat{H} = \hat{H}_0 + \hat{H}_\mathrm{I}$ is treated as the sum of a zeroth-order Hamiltonian $\hat{H}_0$ and a small perturbation $\hat{H}_\mathrm{I}$. As a result, the QME memory kernels, relaxation rate constants and so on depend on bath-only correlation functions, which are easier to calculate than in the case of GQME. Depending on the way $\hat{H}_\mathrm{I}$ is chosen, two major types of QMEs exist. Redfield-type QME is the case where $\hat{H}_0$ is separable to a system part and a bath part, i.e. all system-bath coupling is contained in the interaction $\hat{H}_\mathrm{I}$. With the addition of the Markovian limit (i.e. time-independent rate constants) and usually the secular approximation, TL Redfield QME reduces to the well-known Redfield equation.[56,60,90–95]

In the present dissertation, we focus on the other kind of QMEs based on treating the off-diagonal coupling terms between electronic states as a small perturbation, within the framework of second-order perturbation theory. In what follows, these QMEs will be referred to as *off-diagonal QMEs (OD-QMEs)*. An important characteristic of OD-QME is that its definition changes with different choices of the electronic basis being used, since what counts as "off-diagonal" depends on the basis. In the eigenbasis of the bare electronic Hamiltonian (e.g. the delocalized exciton basis in the context of aggregate systems), OD-QME is more widely known as modified Redfield theory, first developed as a less approximated alternative to Redfield theory.[50,59,94,96–99] Choosing the local excitation basis (i.e. site basis) leads to another type of OD-QME sometimes referred to as QME in the Förster regime,[50,98] limiting the perturbative treatment to the Coulombic coupling between local excited states, which reduces to the well-known Fermi's golden rule (FGR) in the Markovian limit,[43,45,100–102] and further to Marcus theory in the case of harmonic potential energy surface (PES).

Historically, direct application of OD-QME has been limited to the dynamics of electronic populations $\sigma_{jj}(t) = \langle j|\hat{\sigma}(t)|j\rangle$, and the coherence $\sigma_{jk}(t) = \langle j|\hat{\sigma}(t)|k\rangle$ were excluded. What makes the direct application of OD-QME challenging for the dynamics of the coherence is the fact that while GQME and Redfield QME are formulated in the Schrödinger picture, OD-QMEs are formulated in the interaction picture, and the transformation between the pictures alters the coherence but not the populations. Recently, a projection-based technique was proposed to retrieve the Schrödinger picture coherence from population dynamics,[50] which we generalized into a technique that can take any interaction picture reduced dynamics and yield the corresponding Schrödinger picture density.[103]

1.2 Quantum Master Equations

Consider a system whose dynamics is governed by a Hamiltonian $\hat{H} = \hat{H}_0 + \hat{H}_\mathrm{I}$, split into a zeroth-order Hamiltonian $\hat{H}_0$ and an interaction Hamiltonian $\hat{H}_\mathrm{I}$ to be treated perturbatively. The density operator, Hamiltonian and Liouville equation in the interaction picture are given by:

$$\begin{aligned} \tilde{\rho}(t) &= e^{\frac{i}{\hbar}\hat{H}_0 t}\hat{\rho}(t)e^{-\frac{i}{\hbar}\hat{H}_0 t} \\ \tilde{H}_\mathrm{I}(t) &= e^{\frac{i}{\hbar}\hat{H}_0 t}\hat{H}_\mathrm{I}e^{-\frac{i}{\hbar}\hat{H}_0 t} \end{aligned} \tag{1.3a}$$

$$\frac{\mathrm{d}}{\mathrm{d}t}\tilde{\rho}(t) = -\frac{i}{\hbar}\left[\tilde{H}_\mathrm{I}(t), \tilde{\rho}(t)\right] = -\frac{i}{\hbar}\mathcal{L}_\mathrm{I}(t)\tilde{\rho}(t) \tag{1.3b}$$

It should be noted that $\mathcal{L}_\mathrm{I}(t)$ is the (explicitly time-dependent) interaction Liouvillian in the interaction picture, not to be confused with $\mathcal{L}_\mathrm{I}$, which is the (time-independent) Liouvillian in the Schrödinger picture.

We now consider the interaction picture dynamics of a projected state. A projection is defined by its projection superoperator $\mathcal{P}$ which satisfies $\mathcal{P}\mathcal{P} = \mathcal{P}$. The complimentary projection is defined by $\mathcal{Q} = 1 - \mathcal{P}$, it is easy to show that $\mathcal{P}\mathcal{Q} = \mathcal{Q}\mathcal{P} = 0$. To eliminate the bath DOF with the projection, the projection operator is defined as

$$\mathcal{P}\tilde{\rho}(t) = \hat{\rho}_N(0) \otimes \mathcal{P}_e \mathrm{Tr}_N\left[\tilde{\rho}(t)\right], \tag{1.4}$$

where the initial density operator of the overall system $\hat{\rho}(0) = \hat{\rho}_N(0) \otimes \hat{\sigma}(0)$ is assumed to be factorizable into the tensor product of an initial bath density operator $\hat{\rho}_N(0)$ and an initial system density $\hat{\sigma}(0)$. $\mathcal{P}_e$ is a system projection superoperator that filters out irrelevant elements of the reduced density matrix, chosen such that $\mathcal{P}_e\hat{\sigma}(0) = \hat{\sigma}(0)$. In this dissertation we consider two cases: the *full* case where $\mathcal{P}_e = 1$ and the *population only* case where $\mathcal{P}_e\hat{\zeta} = \sum_j |j\rangle\langle j|\langle j|\hat{\zeta}|j\rangle$.

As is well known, the dynamics of the projected state, $\mathcal{P}\tilde{\rho}(t)$, is given by the *Nakajima-Zwanzig equation*:[1,86,94,104,105]

$$\begin{aligned} \frac{\mathrm{d}}{\mathrm{d}t}\mathcal{P}\tilde{\rho}(t) = &-\frac{i}{\hbar}\mathcal{P}\mathcal{L}_\mathrm{I}(t)\mathcal{P}\tilde{\rho}(t) \\ &-\frac{1}{\hbar^2}\int_0^t \mathrm{d}\tau\, \mathcal{P}\mathcal{L}_\mathrm{I}(t)\mathcal{G}(t,\tau)\mathcal{Q}\mathcal{L}_\mathrm{I}(\tau)\mathcal{P}\tilde{\rho}(\tau) \end{aligned} \tag{1.5a}$$

$$\mathcal{G}(t,\tau) \equiv \exp_+\left[-\frac{i}{\hbar}\int_\tau^t \mathrm{d}t'\,\mathcal{Q}\mathcal{L}_\mathrm{I}(t')\right]. \tag{1.5b}$$

Here, the inhomogeneous term vanishes because the projection superoperator was chosen such that

$$\mathcal{P}\tilde{\rho}(0) = \tilde{\rho}(0)\,. \tag{1.6}$$

An alternative route that leads to a *TL* EOM is based on recasting the Nakajima-Zwanzig equation in a TL form, which we will refer to as the *Shibata equation*, by introducing the operator $\Sigma(t)$:[86–89]

$$\begin{aligned}\frac{\mathrm{d}}{\mathrm{d}t}\mathcal{P}\tilde{\rho}(t) = &-\frac{i}{\hbar}\mathcal{P}\mathcal{L}_{\mathrm{I}}(t)\mathcal{P}\tilde{\rho}(t) \\ &-\frac{i}{\hbar}\mathcal{P}\mathcal{L}_{\mathrm{I}}(t)\left[1-\Sigma(t)\right]^{-1}\Sigma(t)\mathcal{P}\tilde{\rho}(t)\end{aligned} \tag{1.7a}$$

$$\Sigma(t) \equiv -\frac{i}{\hbar}\int_0^t \mathrm{d}\tau\, \mathcal{G}(t,\tau)\mathcal{Q}\mathcal{L}_{\mathrm{I}}(\tau)\mathcal{P}\bar{\mathrm{G}}(\tau,t) \tag{1.7b}$$

$$\bar{\mathrm{G}}(\tau,t) \equiv \exp_-\left[\frac{i}{\hbar}\int_\tau^t \mathrm{d}t'\mathcal{L}_{\mathrm{I}}(t')\right], \tag{1.7c}$$

Here, $\bar{\mathrm{G}}(\tau,t)$ is the interaction picture backward time evolution operator from time t to time τ.

Expanding the Nakajima-Zwanzig equation, Eq. (1.5a), to second order in $\mathcal{L}_{\mathrm{I}}(t)$, which is equivalent to setting $\mathcal{G}(t,\tau) = \mathcal{I}$, followed by substituting in the definition of projection $\mathcal{P}$, Eq. 1.4, yields the TNL quantum master equation (TNL-QME), which is an EOM for the projected reduced density matrix in the interaction picture $\tilde{\sigma}_{\mathcal{P}}(t) = \mathcal{P}_e\tilde{\sigma}(t)$:

$$\frac{\mathrm{d}}{\mathrm{d}t}\tilde{\sigma}_{\mathcal{P}}(t) = -\frac{i}{\hbar}\langle\mathcal{L}_{\mathrm{I}}(t)\rangle_{\mathcal{P}}\tilde{\sigma}_{\mathcal{P}}(t) - \frac{1}{\hbar^2}\int_0^t \mathrm{d}\tau\, \mathcal{K}_{\mathcal{P}}(t,\tau)\tilde{\sigma}_{\mathcal{P}}(\tau)\,, \tag{1.8}$$

where the effective Liouvillian superoperator $\langle\mathcal{L}_{\mathrm{I}}\rangle_{\mathcal{P}}$ and the memory kernel $\mathcal{K}_{\mathcal{P}}$ are defined as

$$\langle\mathcal{L}_{\mathrm{I}}(t)\rangle_{\mathcal{P}} = \mathcal{P}_e\mathrm{Tr}_N\Big[\mathcal{L}_{\mathrm{I}}(t)\hat{\rho}_N(0)\Big] \tag{1.9a}$$

$$\mathcal{K}_{\mathcal{P}}(t,\tau) = \mathcal{P}_e\mathrm{Tr}_N\Big[\mathcal{L}_{\mathrm{I}}(t)\mathcal{Q}\mathcal{L}_{\mathrm{I}}(\tau)\hat{\rho}_N(0)\Big] \tag{1.9b}$$

The above procedure can also be applied to the Shibata equation, Eq. (1.7a), yielding a TL quantum master equation (TL-QME) with a very similar form to the TNL case:

$$\frac{\mathrm{d}}{\mathrm{d}t}\tilde{\sigma}_{\mathcal{P}}(t) = -\frac{i}{\hbar}\langle\mathcal{L}_{\mathrm{I}}(t)\rangle_{\mathcal{P}}\tilde{\sigma}_{\mathcal{P}}(t) - \frac{1}{\hbar^2}\Big[\int_0^t \mathrm{d}\tau\, \mathcal{K}_{\mathcal{P}}(t,\tau)\Big]\tilde{\sigma}_{\mathcal{P}}(t)\,, \tag{1.10}$$

where the same definitions for the superoperators, Eq. 1.9 are applied. The similarity between TL and TNL QME is the coincidental result of the second-order perturbative treatment, and is not generally true for higher than second order.

Now armed with a reduced dynamics method in the interaction picture, our next step is to obtain the Schrödinger picture reduced dynamics from the interaction picture one. This is trivial in the case of Redfield QME, where the zeroth-order Hamiltonian $\hat{H}_0^{\mathrm{red}} = \hat{H}_e + \hat{H}_N$ is separable into an

electronic and a nuclear Hamiltonian:

$$\begin{aligned}\hat{\sigma}(t) &= \mathrm{Tr}_N\left[e^{-\frac{i}{\hbar}\hat{H}_e t}e^{-\frac{i}{\hbar}\hat{H}_N t}\tilde{\rho}^{\mathrm{red}}(t)e^{\frac{i}{\hbar}\hat{H}_N t}e^{\frac{i}{\hbar}\hat{H}_e t}\right]\\ &= e^{-\frac{i}{\hbar}\hat{H}_e t}\mathrm{Tr}_N\left[e^{\frac{i}{\hbar}\hat{H}_N t}e^{-\frac{i}{\hbar}\hat{H}_N t}\tilde{\rho}^{\mathrm{red}}(t)\right]e^{\frac{i}{\hbar}\hat{H}_e t}\,,\\ &= e^{-\frac{i}{\hbar}\hat{H}_e t}\tilde{\sigma}^{\mathrm{red}}(t)e^{\frac{i}{\hbar}\hat{H}_e t}\end{aligned} \tag{1.11}$$

this is however not true in the general case where the zeroth order Hamiltonian is not separable, and the Schrödinger picture dynamics $\hat{\sigma}(t)$ has to be obtained with the help of approximations.

We start by expressing $\hat{\sigma}(t)$ formally in terms of the projected states in the interaction picture:

$$\hat{\sigma}(t) = \mathrm{Tr}_N\left[e^{-\frac{i}{\hbar}\mathcal{L}_0 t}\tilde{\rho}(t)\right] = \mathrm{Tr}_N\left[e^{-\frac{i}{\hbar}\mathcal{L}_0 t}\mathcal{P}\tilde{\rho}(t)\right] + \mathrm{Tr}_N\left[e^{-\frac{i}{\hbar}\mathcal{L}_0 t}\mathcal{Q}\tilde{\rho}(t)\right], \tag{1.12}$$

where $\mathcal{P}\tilde{\rho}(t) = \hat{\rho}_N(0)\otimes\tilde{\sigma}_{\mathcal{P}}(t)$ is already obtained by definition, as for $\mathcal{Q}\tilde{\rho}(t)$ we substitute in its formal solution:

$$\hat{\sigma}(t) = \mathrm{Tr}_N\left[e^{-\frac{i}{\hbar}\mathcal{L}_0 t}\mathcal{P}\tilde{\rho}(t)\right] - \frac{i}{\hbar}\int_0^t \mathrm{d}\tau\ \mathrm{Tr}_N\left[e^{-\frac{i}{\hbar}\mathcal{L}_0 t}\mathcal{G}(t,\tau)\mathcal{Q}\mathcal{L}_{\mathrm{I}}(\tau)\mathcal{P}\tilde{\rho}(\tau)\right]. \tag{1.13}$$

Truncating the second term to the *first* order of $\hat{H}_{\mathrm{I}}$ yields an expression for $\hat{\sigma}(t)$ in terms of $\tilde{\sigma}_{\mathcal{P}}(t)$:

$$\hat{\sigma}(t) = \langle\mathcal{G}_0(t)\rangle\tilde{\sigma}_{\mathcal{P}}(t) - \frac{i}{\hbar}\int_0^t \mathrm{d}s\ \bar{\mathcal{K}}(t,s)\tilde{\sigma}_{\mathcal{P}}(s) \tag{1.14a}$$

$$\langle\mathcal{G}_0(t)\rangle = \mathrm{Tr}_N\left[e^{-\frac{i}{\hbar}\mathcal{L}_0 t}\hat{\rho}_N(0)\right] \tag{1.14b}$$

$$\bar{\mathcal{K}}(t,\tau) = \mathrm{Tr}_N\left[e^{-\frac{i}{\hbar}\mathcal{L}_0 t}\mathcal{Q}\mathcal{L}_{\mathrm{I}}(\tau)\hat{\rho}_N(0)\right] \tag{1.14c}$$

A few important observations can be made regarding Eq. 1.14a. It is first-order, and is therefore more approximate than the second order TNL-QME. However, the underlying perturbative truncation in both cases amounts to setting $\mathcal{G}(t,\tau) = \mathcal{I}$. The *full* Schrödinger picture reduced density is retrieved from a *projected* interaction picture density, meaning the dynamics of the electronic coherences can potentially be retrieved from only the populations. A 'TL' version of Eq. 1.14a can be produced by replacing the $\tilde{\sigma}_{\mathcal{P}}(s)$ term with $\tilde{\sigma}_{\mathcal{P}}(t)$. This however leads to little improvements in terms of performance, since Eq. 1.14a is not an integro-differential equation like TNL-QME.

To summarise the derivations up to this point, TNL- and TL-QME are perturbative EOMs for the reduced density matrix. To obtain the Schrödinger picture reduced dynamics, one needs to calculate four superoperators: $\langle\mathcal{L}_{\mathrm{I}}(t)\rangle_{\mathcal{P}}$, $\mathcal{K}_{\mathcal{P}}(t,\tau)$, $\langle\mathcal{G}_0(t)\rangle$, and $\bar{\mathcal{K}}(t,\tau)$, where all information of the bath DOF are contained.

1.3 Overview of the Dissertation

The rest of this dissertation will be organized as follows.

In chapter 2, the off-diagonal QME (OD-QME) is introduced and applied to a spin-boson benchmark model, where the effect of time-nonlocality and the choice of electronic projection will be discussed.

In chapter 3, OD-QME is applied to the calculation of electronic absorption spectra for a benchmark system, where the projection-based method of obtaining the Schrödinger picture dynamics is applied to yield the inter-band coherence. The results are compared to a Redfield TL-QME as well as a numerically exact spectra.

In chapter 4, Fermi's golden rule (FGR), which is equivalent to OD-QME in the Markovian limit, is applied to a cavity-enhanced charge transfer model system to yield the transfer rate constant. This leads to a potential method of obtaining the cavity-enhanced charge transfer rates from only the cavity-free rate constants with minimal potential effort.

In chapter 5, FGR is applied to a molecular triad system to generate the charge transfer rate constants. The underlying correlation functions required to construct the rate constants, unavailable in closed form for a complex molecular model, were obtained via the linearized semiclassical (LSC) method.

A short summary of the dissertation and outlook for future projects with the OD-QME will be given in chapter 6.

CHAPTER 2

Simulating the Reduced Electronic Dynamics via Off-Diagonal Quantum Master Equation

This chapter is based on ref. 103.

2.1 Introduction

As mentioned in the previous chapter, QMEs are perturbative methods where the overall Hamiltonian $\hat{H} = \hat{H}_0 + \hat{H}_{\rm I}$ is split into a zeroth-order reference Hamiltonian $\hat{H}_0$ and a weak interaction $\hat{H}_{\rm I}$. The current dissertation is focused on the *off-diagonal* QME (OD-QME), where the electronic off-diagonal coupling of the Hamiltonian is treated as the weak interaction, i.e.

$$\hat{H}_0 = \sum_j \hat{H}_j |j\rangle\langle j| \tag{2.1a}$$

$$\hat{H}_{\rm I} = \sum_{j\neq k} \hat{V}_{jk} |j\rangle\langle k| \, . \tag{2.1b}$$

Here, $\hat{H}_j = \hat{\mathbf{P}}^2/2 + V_j(\hat{\mathbf{R}})$ is the nuclear Hamiltonian when the system is in one of N_e diabatic electronic states (within a diabatic basis of one's choice $\{|j\rangle; j = 1, ..., N_e\}$), $\hat{\mathbf{R}} = (\hat{R}_1, ..., \hat{R}_N)$ and $\hat{\mathbf{P}} = (\hat{P}_1, ..., \hat{P}_N)$ are the mass-weighted position and momentum operators of the N nuclear DOF, and $\{\hat{V}_{jk} = V_{jk}(\hat{\mathbf{R}})\}$ are the off-diagonal coupling terms between electronic states [$V_{jk}(\hat{\mathbf{R}})$ can become independent of $\hat{\mathbf{R}}$ under the Condon approximation].

In addition to the difference between TNL and TL OD-QME, the difference caused by the choice of the electronic projection $\mathcal{P}_e$ is also put to test. Specifically, two choices of $\mathcal{P}_e$ will be studied: the *full density matrix* $\mathcal{P}_e = \mathcal{I}$ where all matrix elements are propagated in the interaction picture, and the *population dynamics only* $\mathcal{P}_e = \sum_j |j\rangle\langle j|{\rm Tr}[|j\rangle\langle j|\cdot] \equiv \mathcal{P}_P$ where only the populations are propagated in the interaction picture. For the rest of this dissertation, these four OD-QMEs will be referred to by shorthands as shown in Table. 2.1.

Table 2.1: Shorthands for the four types of OD-QMEs under consideration in the current dissertation

	$\mathcal{P}=\mathcal{I}$	$\mathcal{P}=\mathcal{P}_P$
Time-nonlocal	f-TNL-OD-QME	p-TNL-OD-QME
Time-local	f-TL-OD-QME	p-TL-OD-QME

2.2 Full Density Matrix Off-Diagonal Quantum Master Equation

In the case of f-TNL-OD-QME and f-TL-OD-QME, the QME superoperators $\langle\mathcal{L}_{\rm I}(t)\rangle_{\mathcal{P}}$, $\mathcal{K}_{\mathcal{P}}(t,\tau)$, $\langle\mathcal{G}_0(t)\rangle$, and $\bar{\mathcal{K}}(t,\tau)$ are given explicitly by

$$\langle\mathcal{L}_{\rm I}(t)\rangle_{\mathcal{P}}\,\hat{\zeta}=\mathrm{Tr}_N\Big[\mathcal{L}_{\rm I}(t)\hat{\rho}_N(0)\,\hat{\zeta}\Big] \tag{2.2a}$$

$$\mathcal{K}_{\mathcal{P}}(t,\tau)\,\hat{\zeta}=\mathrm{Tr}_N\Big[\mathcal{L}_{\rm I}(t)\mathcal{L}_{\rm I}(\tau)\hat{\rho}_N(0)\,\hat{\zeta}\Big]-\mathrm{Tr}_N\Big[\mathcal{L}_{\rm I}(t)\hat{\rho}_N(0)\,\mathrm{Tr}_N\big[\mathcal{L}_{\rm I}(\tau)\hat{\rho}_N(0)\,\hat{\zeta}\big]\Big] \tag{2.2b}$$

$$\langle\mathcal{G}_0(t)\rangle\,\hat{\zeta}=\mathrm{Tr}_N\Big[e^{-\frac{i}{\hbar}\mathcal{L}_0 t}\hat{\rho}_N(0)\,\hat{\zeta}\Big] \tag{2.2c}$$

$$\bar{\mathcal{K}}(t,\tau)\,\hat{\zeta}=\mathrm{Tr}_N\Big[e^{-\frac{i}{\hbar}\mathcal{L}_0 t}\mathcal{L}_{\rm I}(\tau)\hat{\rho}_N(0)\,\hat{\zeta}\Big]-\mathrm{Tr}_N\Big[e^{-\frac{i}{\hbar}\mathcal{L}_0 t}\hat{\rho}_N(0)\,\mathrm{Tr}_N\big[\mathcal{L}_{\rm I}(\tau)\hat{\rho}_N(0)\,\hat{\zeta}\big]\Big]\,. \tag{2.2d}$$

Substituting in the definition of the zeroth order and the interaction Hamiltonian, we arrive at the explicit matrix elements of the superoperators $\mathcal{F}_{jk,mn}\equiv\langle k|(\mathcal{F}|m\rangle\langle n|)|j\rangle$:

$$\big\langle\mathcal{L}_{\rm I}(t)\big\rangle_{jk,mn}=\delta(k,n)\big\langle\hat{V}_{jm}(t)\big\rangle-\delta(j,m)\big\langle\hat{V}_{nk}(t)\big\rangle \tag{2.3a}$$

$$\begin{aligned}\mathcal{K}_{jk,mn}(t,\tau)=\delta(k,n)\sum_{l\neq j,m}\big\langle\delta\hat{V}_{jl}(t)\delta\hat{V}_{lm}(\tau)\big\rangle+\delta(j,m)\sum_{l\neq k,n}\big\langle\delta\hat{V}_{kl}(t)\delta\hat{V}_{ln}(\tau)\big\rangle^*\\-\big\langle\delta\hat{V}_{nk}(t)\delta\hat{V}_{jm}(\tau)\big\rangle-\big\langle\delta\hat{V}_{mj}(t)\delta\hat{V}_{kn}(\tau)\big\rangle^*\end{aligned} \tag{2.3b}$$

$$\big\langle\mathcal{G}_0(t)\big\rangle_{jk,mn}=\delta(j,m)\delta(k,n)\big\langle\hat{S}_{kj}(t)\big\rangle \tag{2.3c}$$

$$\bar{\mathcal{K}}_{jk,mn}(t,\tau)=\delta(n,k)\big\langle\delta\hat{S}_{kj}(t)\delta\hat{V}_{jm}(\tau)\big\rangle-\delta(j,m)\big\langle\delta\hat{S}_{jk}(t)\delta\hat{V}_{kn}(\tau)\big\rangle^*\,, \tag{2.3d}$$

where $\langle\cdots\rangle=\mathrm{Tr}_N[\cdots\hat{\rho}_N(0)]$, and

$$\hat{V}_{kl}(t)=e^{\frac{i}{\hbar}\hat{H}_k t}\hat{V}_{kl}e^{-\frac{i}{\hbar}\hat{H}_l t}=\mathrm{Tr}_e\Big[|l\rangle\langle k|\tilde{H}_{\rm I}(t)\Big] \tag{2.4a}$$

$$\hat{S}_{kl}(t)=e^{\frac{i}{\hbar}\hat{H}_k t}e^{-\frac{i}{\hbar}\hat{H}_l t} \tag{2.4b}$$

$$\delta\hat{A}=\hat{A}-\big\langle\hat{A}\big\rangle\,, \tag{2.4c}$$

such that

$$\left\langle \delta\hat{A}\delta\hat{B}\right\rangle = \left\langle \hat{A}\hat{B}\right\rangle - \left\langle \hat{A}\right\rangle\left\langle \hat{B}\right\rangle . \tag{2.4d}$$

As a result, all information regarding the bath DOF needed to solve the reduced EOM f-TNL-OD-QME and f-TL-OD-QME are contained in the two-time bath correlation functions

$$\left\langle \hat{V}_{jk}(t)\hat{V}_{mn}(\tau)\right\rangle = \mathrm{Tr}_N\left[e^{\frac{i}{\hbar}\hat{H}_j t}\hat{V}_{jk}e^{-\frac{i}{\hbar}\hat{H}_k t}\, e^{\frac{i}{\hbar}\hat{H}_m \tau}\hat{V}_{mn}e^{-\frac{i}{\hbar}\hat{H}_n \tau}\,\hat{\rho}_N(0)\right], \tag{2.5}$$

whereas the single-time correlation function $\langle\hat{V}_{jk}(t)\rangle$ is the special case of $\tau = 0$, and $\langle\hat{S}_{jk}(t)\hat{V}_{mn}(\tau)\rangle$ can be thought of as the special case of setting $\hat{V}_{jk} = 1$.

We now pay a closer look to the superoperators Eq. 2.3a, 2.3b responsible for the interaction picture dynamics. The first order term Eq. 2.3a, as well as the first two terms of the memory kernel term Eq. 2.3b, couple electronic density matrix elements within the same row or column, thereby allowing only for population-to-coherence and coherence-to-population transfer, while the remaining two terms of Eq. 2.3b couple matrix elements across different rows and columns, becoming the only source of population-to-population and coherence-to-coherence transfer, within the framework of the f-OD-QMEs.

The other two superoperators Eq. 2.3c, 2.3d are utilized to evaluate the Schrödinger picture dynamics. Eq. 2.3c originates from the first term in Eq. 1.13, which is *zeroth* order in $\hat{H}_{\mathrm{I}}$. This term corresponds to the case where the interaction vanishes, and only couples each matrix element to itself. Eq. 2.3d corresponds to the term that is first order in $\hat{H}_{\mathrm{I}}$, and couples density matrix elements within the same row or column. It is easy to show that under the transformation of Eq. 1.14a, the population dynamics remains invariant. i.e. $\langle\mathcal{G}_0\rangle_{jj,jj} = 1$ and $\bar{\mathcal{K}}_{jj,jk} = 0$

2.3 Population Dynamics Off-Diagonal Quantum Master Equation

Since the electronic populations are invariant in the transformation to and from the interaction picture, OD-QMEs was historically applied mostly to obtain populations dynamics. As a result, the *population dynamics only* projection $\mathcal{P}_e = \mathcal{P}_P$ has been a popular choice of projection for previous studies employing OD-QME.[51,86,98,106–109] This corresponds to p-TNL-OD-QME and p-TL-OD-QME, where the QME superoperators $\langle\mathcal{L}_{\mathrm{I}}(t)\rangle_{\mathcal{P}}$, $\mathcal{K}_{\mathcal{P}}(t,\tau)$, $\langle\mathcal{G}_0(t)\rangle$, and $\bar{\mathcal{K}}(t,\tau)$ are given

explicitly by

$$\langle \mathcal{L}_{\mathrm{I}}(t)\rangle_{\mathcal{P}} = 0 \tag{2.6a}$$

$$\mathcal{K}_{\mathcal{P}}(t,\tau)\ \hat{\zeta} = \mathcal{P}_P \mathrm{Tr}_N\Big[\mathcal{L}_{\mathrm{I}}(t)\mathcal{L}_{\mathrm{I}}(\tau)\hat{\rho}_N(0)\ \mathcal{P}_P\hat{\zeta}\Big] \tag{2.6b}$$

$$\langle \mathcal{G}_0(t)\rangle = \mathcal{P}_P \tag{2.6c}$$

$$\bar{\mathcal{K}}(t,\tau)\ \hat{\zeta} = \mathrm{Tr}_N\Big[e^{-\frac{i}{\hbar}\mathcal{L}_0 t}\mathcal{L}_{\mathrm{I}}(\tau)\hat{\rho}_N(0)\ \mathcal{P}_P\hat{\zeta}\Big]\ . \tag{2.6d}$$

In this case of population transfer only dynamics, most matrix elements of the superoperators vanish except for those involving population transfer:

$$\begin{aligned}\mathcal{K}_{jj,mm}(t,\tau) = {}& \delta(j,m)\sum_{l\neq j}\big\langle \hat{V}_{jl}(t)\hat{V}_{lj}(\tau)\big\rangle + \delta(j,m)\sum_{l\neq j}\big\langle \hat{V}_{jl}(t)\hat{V}_{lj}(\tau)\big\rangle^* \\ & - \big\langle \hat{V}_{mj}(t)\hat{V}_{jm}(\tau)\big\rangle - \big\langle \hat{V}_{mj}(t)\hat{V}_{jm}(\tau)\big\rangle^*\end{aligned} \tag{2.7a}$$

$$\big\langle \mathcal{G}_0(t)\big\rangle_{jj,mm} = \delta(j,m) \tag{2.7b}$$

$$\bar{\mathcal{K}}_{jk,mm}(t,\tau) = \delta(m,k)\big\langle \hat{S}_{kj}(t)\hat{V}_{jk}(\tau)\big\rangle - \delta(j,m)\big\langle \hat{S}_{jk}(t)\hat{V}_{kj}(\tau)\big\rangle^*\ . \tag{2.7c}$$

Here, the first two terms of $\mathcal{K}_{jj,mm}$ are the self-couplings of the electronic populations, whereas the remaining two terms are the population transfer between states. $\langle \mathcal{G}_0(t)\rangle$ corresponds to a trivial transformation where all electronic populations are unchanged, and $\bar{\mathcal{K}}$ corresponds to a transformation where an electronic coherence σ_{jk} in the Schrödinger picture is obtained from the corresponding two populations σ_{jj}, σ_{kk}.

One advantage population-only dynamics has over full density matrix dynamics is that the full matrix dynamics requires one to evaluate the correlation function $\langle \hat{V}_{jk}(t)\hat{V}_{mn}(\tau)\rangle$ for all combinations of $j \neq k, m \neq n$, which for a generic system with N_e electronic states is $N_e^2(N_e-1)^2$ correlation function in total; while the population-only case, on the other hand, requires only $N_e(N_e-1)$ correlation functions in the form of $\langle \hat{V}_{jk}(t)\hat{V}_{kj}(\tau)\rangle$. Since the number of bath DOF usually far exceeds that of the electronic system, the evaluation of the correlation functions takes up the majority of effort in OD-QME. As a result, population-only dynamics effectively reduces the effort of OD-QME, even in the minimum case of a two level systems where the number of correlation functions to be evaluated is halved.

It should be noted that the p-TNL-OD-QME Eq. 2.6b has the same form as what some previous studies referred to as the generalized master equation (GME).[52,106,110,111] p-TL-OD-QME, on the other hand, is deeply related to the well-known Fermi's golden rule (FGR). To see that, we first

notice that p-TL-OD-QME can be cast into a Pauli-type rate equation:

$$\frac{\mathrm{d}}{\mathrm{d}t}\sigma_{jj}(t) = \sum_{k\neq j} k_{jk}(t)\sigma_{kk}(t) - \sum_{k\neq j} k_{kj}(t)\sigma_{jj}(t)\,, \tag{2.8a}$$

where the rate constants

$$k_{jk}(t) = \frac{2}{\hbar^2}\mathrm{Re}\int_0^t \mathrm{d}\tau\, \left\langle \hat{V}_{kj}(t)\hat{V}_{jk}(\tau)\right\rangle \tag{2.8b}$$

coincides with the well known non-equilibrium FGR expression.[43,44,46,48,112] To arrive at the more widely used Markovian FGR where the rate constants are not time-dependent, two approximations are made, the first of which assumes that

$$\begin{aligned}\left\langle \hat{V}_{jk}(t)\hat{V}_{kj}(\tau)\right\rangle &= \mathrm{Tr}_N\left[e^{-\frac{i}{\hbar}\hat{H}_j t}\hat{\rho}_N(0)e^{\frac{i}{\hbar}\hat{H}_j t}\,\hat{V}_{jk}\,e^{-\frac{i}{\hbar}\hat{H}_k(t-\tau)}\hat{V}_{kj}e^{\frac{i}{\hbar}\hat{H}_j(t-\tau)}\right]\\ &\approx \mathrm{Tr}_N\left[\hat{\rho}_j^{eq}\,e^{\frac{i}{\hbar}\hat{H}_j(t-\tau)}\hat{V}_{jk}e^{-\frac{i}{\hbar}\hat{H}_k(t-\tau)}\,\hat{V}_{kj}\right] = \left\langle \hat{V}_{jk}(t-\tau)\hat{V}_{kj}\right\rangle,\end{aligned} \tag{2.9}$$

where the two-time correlation function becomes a one-time correlation function that depends on $t-\tau$ instead of $\{t,\tau\}$. This can be achieved by either starting from the thermal equilibrium of state j, $\hat{\rho}_j^{eq} = \exp(-\beta\hat{H}_j)/Z$, or assuming that $\exp(-i\hat{H}_j t/\hbar)\hat{\rho}_N(0)\exp(i\hat{H}_j t/\hbar)$ relaxes to $\hat{\rho}_j^{eq}$ in a short-enough time scale. This is followed by a second assumption that $\langle\hat{V}_{jk}(t-\tau)\hat{V}_{kj}\rangle$ decays to zero in a short time scale, such that the integral in Eq. 2.8b can be extended to infinity,

$$k_{jk} = \frac{2}{\hbar^2}\mathrm{Re}\int_0^\infty \mathrm{d}t\, \left\langle \hat{V}_{kj}(t)\hat{V}_{jk}\right\rangle, \tag{2.10}$$

which is the fully Markovian FGR in its classical form, referred to *equilibrium* FGR in some contexts.

2.4 The Garg-Onuchic-Ambegaokar Model

In this chapter, we compare and contrast the dynamics of the electronic populations and coherences obtained via the four types of OD-QMEs outlined in Sec. 2.1 (see Table 2.1). We do so in the context of the Garg-Onuchic-Ambegaokar (GOA) benchmark model for charge transfer in the condensed phase.[113] Within this model, a donor (D) and an acceptor (A) diabatic electronic state are coupled to a primary nuclear mode. The potential energy surface (PES) for this primary mode is assumed to be harmonic, with the equilibrium geometry and energy in the donor and acceptor states shifted relative to one another. The primary mode is also bilinearly coupled to a thermal bath consisting of a large number of secondary harmonic modes whose PESs are electronic-state-

independent.

The Hamiltonian for the GOA model is given by

$$\begin{aligned}\hat{H} =& \Gamma\hat{\sigma}_x + \frac{\hbar\omega_{\mathrm{DA}}}{2}\hat{\sigma}_z + \frac{\hat{P}_y^2}{2} + \frac{1}{2}\Omega^2(\hat{y} + y_0\hat{\sigma}_z)^2 \\ &+ \sum_{\alpha=1}^{N-1}\Big[\frac{\hat{p}_\alpha^2}{2} + \frac{1}{2}\omega_\alpha^2\big(\hat{x}_\alpha + \frac{c_\alpha\hat{y}}{\omega_\alpha^2}\big)^2\Big]\end{aligned} \tag{2.11}$$

Here, $\hat{\sigma}_x = |D\rangle\langle A| + |A\rangle\langle D|$ and $\hat{\sigma}_z = |D\rangle\langle D| - |A\rangle\langle A|$, where $|D\rangle$ and $|A\rangle$ at the donor and acceptor diabatic electronic states, respectively; Γ is the electronic coupling coefficient (assumed to be constant); $-\hbar\omega_{\mathrm{DA}}$ is the donor-to-acceptor charge transfer reaction free energy; $\{\hat{y}, \hat{P}_y, \Omega\}$ and $\{\hat{x}_\alpha, \hat{p}_\alpha, \omega_\alpha\}$ are the mass-weighed coordinates, momenta and frequencies for the primary and secondary modes, respectively; $\{c_\alpha\}$ are the coupling coefficients between the primary mode and secondary modes; the equilibrium positions of the primary mode in the donor and acceptor states are shifted relative to each other by $2y_0$, such that the reorganization energy is $E_r = 2\Omega^2 y_0^2$. The secondary modes are described by an Ohmic spectral density with exponential cutoff

$$J(\omega) \equiv \frac{\pi}{2}\sum_{\alpha=1}^{N}\frac{c_\alpha^2}{\omega_\alpha}\delta(\omega - \omega_\alpha) = \eta\omega e^{-\omega/\omega_c}\,. \tag{2.12}$$

Here, ω_c is the cutoff frequency, and η determines the coupling strength between the primary and secondary modes.

Since the primary and secondary modes are harmonic and bilinearly coupled, the GOA Hamiltonian can be expressed in terms of normal modes. Instead of using the asymptotic effective spectral density for the normal modes, which is only known in closed form in the limit of $\Omega >> \omega_c$,[114] we obtained the normal modes by diagonalizing the Hessian matrix.[46] In terms of normal modes, the GOA Hamiltonian has the same form as Eq. (2.1) with $N_e = 2$:

$$\hat{H} = \hat{H}_D|D\rangle\langle D| + \hat{H}_A|A\rangle\langle A| + \hat{V}_{DA}|D\rangle\langle A| + \hat{V}_{AD}|A\rangle\langle D|\,, \tag{2.13a}$$

with

$$\begin{aligned}\hat{H}_D =& \sum_{j=1}^{N}\frac{\hat{P}_j^2}{2} + \frac{1}{2}\sum_{j=1}^{N}\tilde{\omega}_j^2\hat{R}_j^2 + \hbar\omega_{DA} \\ \hat{H}_A =& \sum_{j=1}^{N}\frac{\hat{P}_j^2}{2} + \frac{1}{2}\sum_{j=1}^{N}\tilde{\omega}_j^2\big(\hat{R}_j - R_j^{eq}\big)^2\end{aligned} \tag{2.13b}$$

and $\hat{V}_{DA} = \hat{V}_{AD} = \Gamma$. Here, $\{\hat{R}_j, \hat{P}_j, \tilde{\omega}_j\}$ are the normal mode coordinates, momenta and frequencies, respectively, and $\{R_j^{eq}\}$ are the equilibrium donor-to-acceptor shift in equilibrium geometry

along the j-th normal mode coordinates (the reader is referred to Ref.[46] for more details on those quantities). In this form, the Hamiltonian is very similar to a spin-boson model, where the PESs for the two diabatic states are harmonic and identical except for a shift in equilibrium energy and equilibrium geometry. Importantly, the correlation functions $\langle \hat{V}_{jk}(t) \rangle$, $\langle \hat{V}_{ij}(t)\hat{V}_{kl}(\tau) \rangle$, $\langle \hat{S}_{jk}(t) \rangle$, and $\langle \hat{S}_{ij}(t)\hat{V}_{kl}(\tau) \rangle$ can be evaluated exactly for this kind of system. For the rest of this dissertation, we will use the term *spin-boson* loosely to refer to this kind of harmonic systems.

The system is assumed to start at the donor state with the nuclear DOF in thermal equilibrium on the donor PES. Thus, $\hat{\rho}(0) = \hat{\rho}_N(0) \otimes |D\rangle\langle D|$, and $\hat{\rho}_B(0) = e^{-\beta \hat{H}_D} / \operatorname{Tr}_B[e^{-\beta \hat{H}_D}]$.

The OD-QMEs for the GOA model under consideration here are based on defining the off-diagonal coupling in terms of the $\{|D\rangle, |A\rangle\}$ basis, so that $\hat{H}_I = \Gamma[|D\rangle\langle A| + |A\rangle\langle D|]$. Since $\hat{H}_I$ is a purely electronic (or system) operator in this case, treating it as a small perturbation is not the same as assuming weak system-bath coupling. Again, it should also be noted that other choices of diabatic basis would lead to different types of OD-QMEs.

quantum-mechanically exact expressions for $\langle \hat{V}_{jk}(t) \rangle$, $\langle \hat{V}_{ij}(t)\hat{V}_{kl}(\tau) \rangle$, $\langle \hat{S}_{jk}(t) \rangle$, and $\langle \hat{S}_{ij}(t)\hat{V}_{kl}(\tau) \rangle$ can be obtained in closed form for a spin-boson model (for derivation, see Appendix A):

$$\Big\langle \hat{V}_{DA}(t)\hat{V}_{AD}(\tau) \Big\rangle = \Gamma^2 e^{i\omega_{\mathrm{DA}}(t-\tau)} \exp\Bigg\{ \sum_j \frac{\tilde{\omega}_j (R_j^{eq})^2}{2\hbar} \coth(\frac{1}{2}\beta\hbar\tilde{\omega}_j) \Big[\cos\left(\tilde{\omega}_j(t-\tau)\right) - 1 \Big] \Bigg\}$$
$$\exp\Bigg\{ -i \sum_j \frac{\tilde{\omega}_j (R_j^{eq})^2}{2\hbar} \sin\left(\tilde{\omega}_j(t-\tau)\right) \Bigg\} \tag{2.14a}$$

$$\Big\langle \hat{V}_{AD}(t)\hat{V}_{DA}(\tau) \Big\rangle = \Gamma^2 e^{-i\omega_{\mathrm{DA}}(t-\tau)} \exp\Bigg\{ \sum_j \frac{\tilde{\omega}_j (R_j^{eq})^2}{2\hbar} \coth(\frac{1}{2}\beta\hbar\tilde{\omega}_j) \Big[\cos\left(\tilde{\omega}_j(t-\tau)\right) - 1 \Big] \Bigg\}$$
$$\exp\Bigg\{ i \sum_j \frac{\tilde{\omega}_j (R_j^{eq})^2}{\hbar} \Big[\sin\left(\tilde{\omega}_j t\right) - \sin\left(\tilde{\omega}_j \tau\right) - \frac{1}{2}\sin\left(\tilde{\omega}_j(t-\tau)\right) \Big] \Bigg\} \tag{2.14b}$$

$$\Big\langle \hat{V}_{DA}(t)\hat{V}_{DA}(\tau) \Big\rangle = \Gamma^2 e^{i\omega_{\mathrm{DA}}(t+\tau)} \exp\Bigg\{ \sum_j \frac{\tilde{\omega}_j (R_j^{eq})^2}{\hbar} \coth(\frac{1}{2}\beta\hbar\tilde{\omega}_j) \Big[\cos\left(\tilde{\omega}_j t\right) + \cos\left(\tilde{\omega}_j \tau\right) \Big] \Bigg\}$$
$$\exp\Bigg\{ -\sum_j \frac{\tilde{\omega}_j (R_j^{eq})^2}{2\hbar} \coth(\frac{1}{2}\beta\hbar\tilde{\omega}_j) \Big[3 + \cos\left(\tilde{\omega}_j(t-\tau)\right) \Big] \Bigg\} \tag{2.14c}$$
$$\exp\Bigg\{ i \sum_j \frac{\tilde{\omega}_j (R_j^{eq})^2}{\hbar} \Big[\frac{1}{2}\sin\left(\tilde{\omega}_j(t-\tau)\right) - \sin\left(\tilde{\omega}_j t\right) \Big] \Bigg\}$$

$$\left\langle \hat{V}_{DA}(t) \right\rangle = \left\langle \hat{V}_{DA}(t)\hat{V}_{AD}(0) \right\rangle \Gamma^{-1} \tag{2.14d}$$

$$\left\langle \hat{V}_{AD}(t)\hat{V}_{AD}(\tau) \right\rangle = \left\langle \hat{V}_{DA}(\tau)\hat{V}_{AD}(t) \right\rangle^{*} \tag{2.14e}$$

$$\left\langle \hat{S}_{DA}(t) \right\rangle = \left\langle \hat{V}_{DA}(t) \right\rangle \Gamma^{-1} \tag{2.14f}$$

$$\left\langle \hat{S}_{ij}(t)\hat{V}_{kl}(\tau) \right\rangle = \left\langle \hat{V}_{ij}(t)\hat{V}_{kl}(\tau) \right\rangle \Gamma^{-1} \tag{2.14g}$$

2.5 Results and Discussion

In this section, we report results obtained via the four types of OD-QMEs (see Table 2.1) for the GOA model. If not otherwise stated, the values of the model parameters used are as in Table 2.2. The frequencies and coupling coefficients for the secondary modes, $\{\omega_\alpha, c_\alpha\}$, were generated from the spectral density (see Eq. (2.12)) using the numerical discretization procedure described in Appendix B, where the number of secondary modes N was chosen such that the OD-QME dynamics converge. The numerical solution of the TNL-QMEs (Eq. 1.8) was obtained using a 4th-order Runge-Kutta algorithm for integro-differential equations developed by Lubich, described in Appendix C.[115] Unless stated otherwise, Eq. 1.14a with the projection operator chosen to match the OD-QME is used to calculate the schrödinger picture coherence. The OD-QMEs results are also compared to numerically exact results that were obtained via the ML-MCTDH method.[116]

Table 2.2: GOA model parameters (in atomic units)

model parameters			bath parameters				numerical parameter
Γ	ω_{DA}	β	ω_c	η	Ω	y_0	N
0.2	0.0	∞	1.0	1.0	0.5	0.75	50

In Fig. 2.1, we show the electronic population difference (top row) and coherence (bottom row) as a function of time, for different electronic coupling strengths, $\Gamma = \{0.01, 0.1, 0.2, 1.0\}$. For the weakest electronic coupling ($\Gamma = 0.01$), all four OD-QMEs are seen to produce highly accurate electronic populations and coherences, which can be attributed to the fact that the OD-QMEs are based on treating the electronic coupling perturbatively, and thereby expected to be accurate when the electronic coupling is sufficiently weak. Not surprisingly, discrepancies are observed when the electronic coupling is made stronger. However, the deviations from the exact results with increasing electronic coupling strength is seen to be highly sensitive to the type of OD-QME. More specifically, while the two TNL-OD-QMEs (f-TNL-OD-QME and p-TNL-OD-

QME) remain rather accurate throughout the entire electronic coupling range, this is not the case for the TL-OD-QMEs (f-TL-OD-QME and p-TL-OD-QME). This is particularly true for the OD-QMEs based on the populations-only projection superoperator, where the p-TL-OD-QME is seen to become highly inaccurate at stronger electronic coupling, while the p-TL-OD-QME remains accurate.

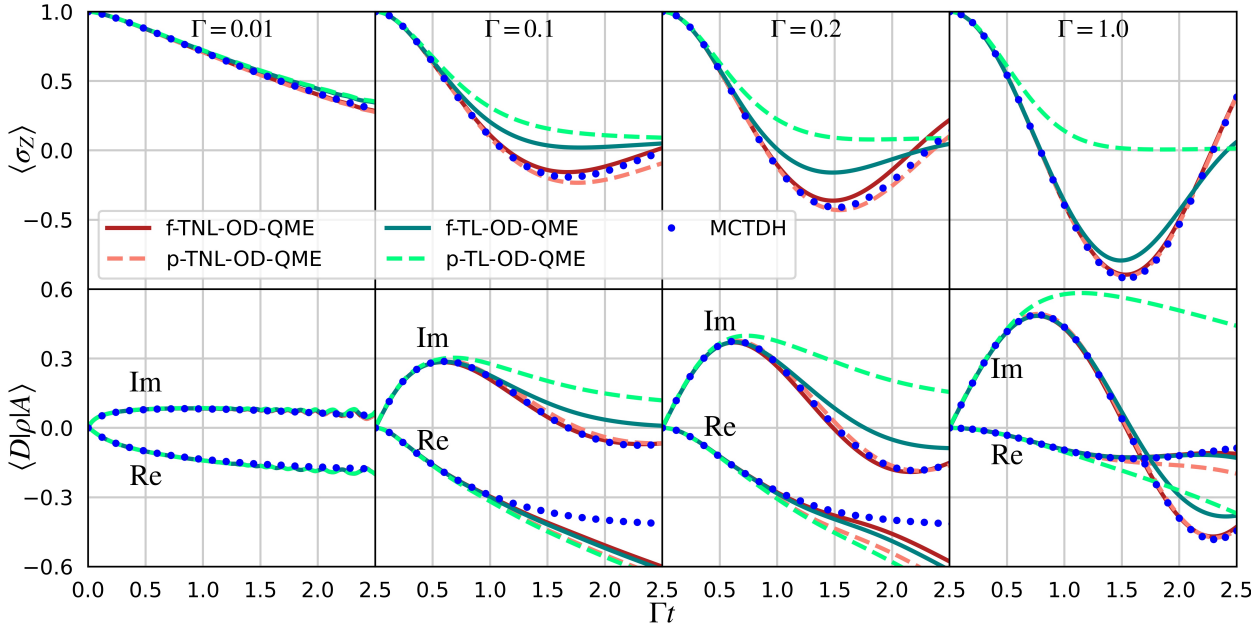


Figure 2.1: Electronic population difference (top row) and coherence (bottom row) as a function of time obtained using f-TNL-OD-QME, p-TNL-OD-QME, f-TL-OD-QME, p-TL-OD-QME for the GOA model with $\Gamma = \{0.01, 0.1, 0.2, 1.0\}$. See Table.2.2 for the values of other parameters. Also shown are numerically exact MCTDH-based results.

Those trends suggest that the combination of projecting out the coherences with the convolutionless approximation can have a significant negative effect on the accuracy of the OD-QME. This is likely due to the fact that projecting out the electronic coherences implies that their effect is accounted for perturbatively, via the memory kernel, which becomes less valid with increasing electronic coupling strength. This is not the case for the f-density-matrix OD-QMEs (f-TNL-OD-QME and f-TL-OD-QME), where the populations and coherences are treated on the same footing. As a result the difference between f-TNL-OD-QME and f-TL-OD-QME is significantly smaller.

It should also be noted that the discrepancies that emerge between the OD-QMEs and exact results with increasing electronic coupling strength are larger for the coherence than for the population difference. This can be attributed to the fact that the procedure for obtaining the Schrödinger picture coherences is based on first-order perturbation theory, whereas the populations are obtained within the framework of second-order perturbation theory.

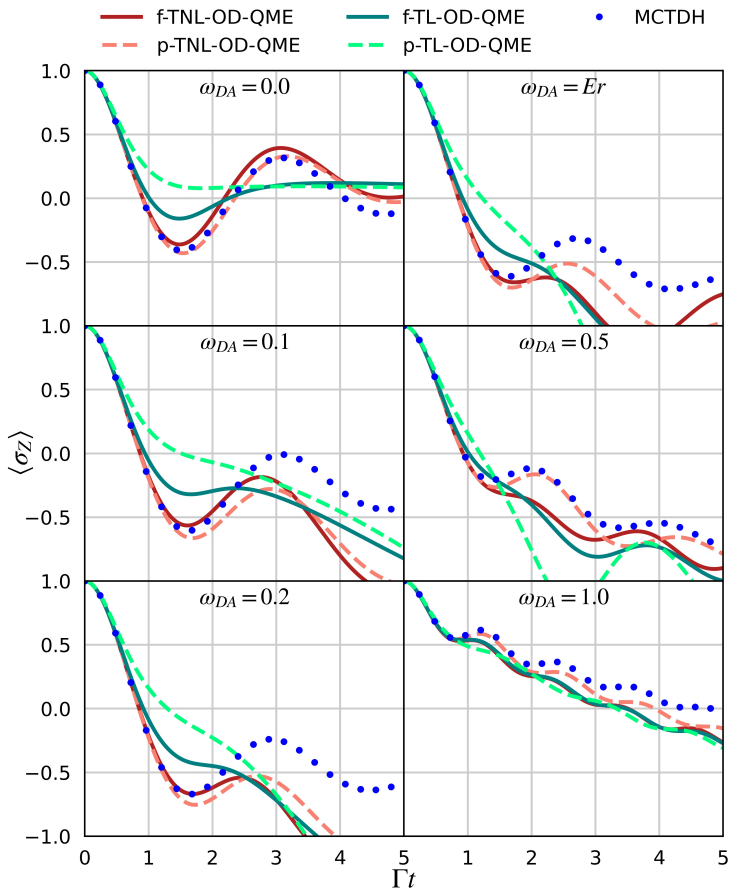


Figure 2.2: Electronic population difference as a function of time obtained using f-TNL-OD-QME, p-TNL-OD-QME, f-TL-OD-QME and p-TL-OD-QME, with $|\omega_{\rm DA}| = \{0.0, 0.1, 0.2, E_r, 0.5, 1.0\}$. See Table.2.2 for the values of other parameters. Also shown are numerically exact MCTDH-based results.

In Fig. 2.2, we show the electronic population difference as a function of time for different values of the charge transfer reaction free energy, $|\omega_{\rm DA}| = \{0.0, 0.1, 0.2, E_r, 0.5, 1.0\}$ ($|\omega_{\rm DA}| = E_r$ correspond to the inversion point between the normal and inverted regions, where $E_r = 0.28$). While the accuracy of the different types of OD-QMEs is seen to follow the same trends as in Fig. 2.1, the discrepancies are seen to be a non-monotonic function of $|\omega_{\rm DA}|$. More specifically, the discrepancies are seen to be largest in the vicinity of the inversion point between the Marcus normal and inverted regions ($|\omega_{\rm DA}| = E_r$), and becomes smaller as one goes deeper into either the normal ($|\omega_{\rm DA}| < E_r$) or inverted ($|\omega_{\rm DA}| > E_r$) regions. This can be attributed to the fact that treating the electronic coupling as weak is less valid in the vicinity of the inversion point, when the charge transfer process is barrier-less, than further away from it (either in the normal or inverted regions), which corresponds to increasing barrier height, and thereby weaker effective electronic coupling.

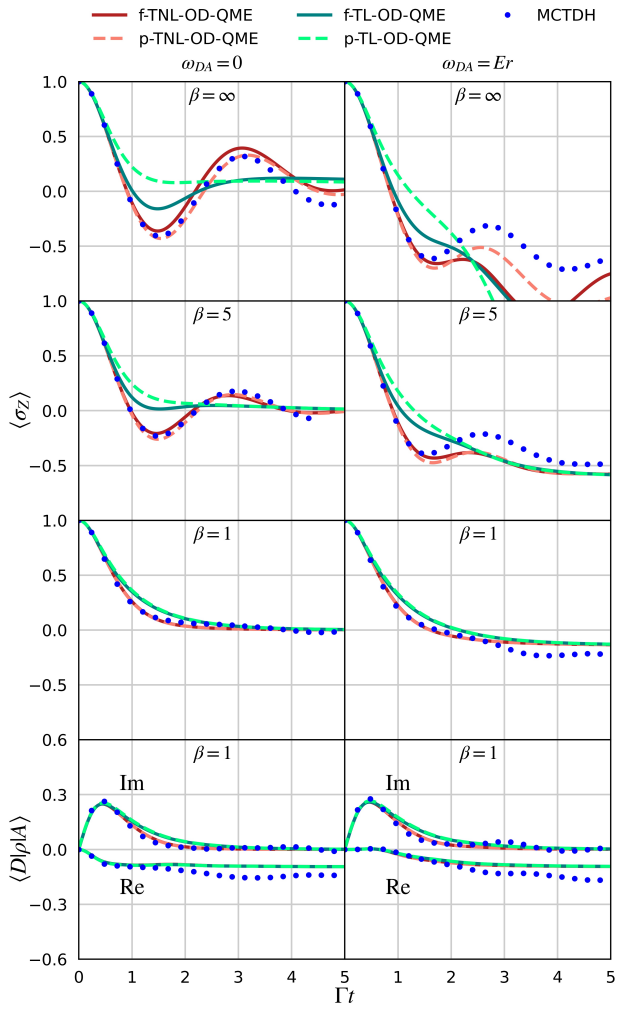


Figure 2.3: Electronic population difference (top three rows) as a function of time obtained using f-TNL-OD-QME, p-TNL-OD-QME, f-TL-OD-QME and p-TL-OD-QME, for the GOA model with $\beta = \{\infty, 5, 1\}$ and $\omega_{\rm DA} = \{0.0, E_r\}$. See Table.2.2 for the values of the other parameters. The bottom row shows the coherence for the case of $\beta = 1$. Also shown are numerically exact MCTDH-based results.

In Fig. 2.3, we show the electronic population difference (top three rows) as a function of time for different inverse temperatures, $\beta = \{\infty, 5, 1\}$ and $|\omega_{\rm DA}| = \{0.0, E_r\}$. Also included is the coherence at the highest absolute temperature, $\beta = 1$ (bottom row). The OD-QMEs are seen to become more accurate with increasing absolute temperature (decreasing β). Here too, the deviations between he exact and OD-QME-based results, which increase with decreasing absolute temperature, are seen to be sensitive to the type of OD-QME,following the same above mentioned trends.

The improved accuracy of OD-QMEs with increasing temperature, and particularly so for the

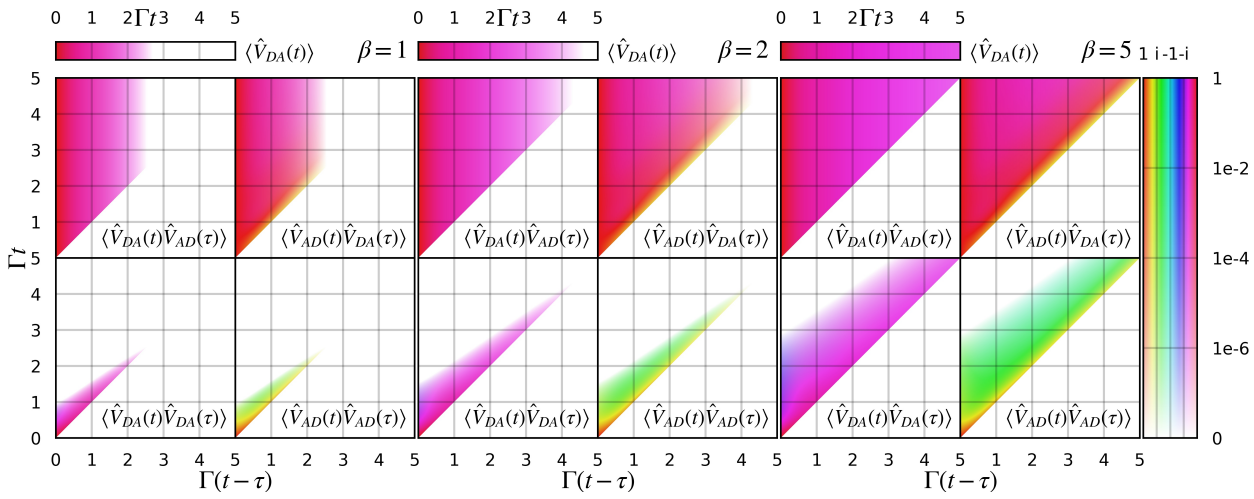


Figure 2.4: $\langle \hat{V}_{ij}(t) \rangle$ and $\langle \hat{V}_{ij}(t)\hat{V}_{kl}(\tau) \rangle$ as a function of t and $(t, t-\tau)$, respectively, where $i, j, k, l \in \{D, A\}$, for the GOA model with $\beta = \{5, 2, 1\}$. See Table.2.2 for the values of other parameters. The intensity stands for the modulus, while the hue stands for the phase. The values are normalized so that $\langle \hat{V}_{ij}(0) \rangle = \langle \hat{V}_{ij}(0)\hat{V}_{kl}(0) \rangle = 1$. The diagonal line represents $\tau = 0$, and the lower triangle portion is set to zero by definition.

TL-OD-QMEs, can be traced back to the temperature dependence of $\langle \hat{V}_{jk}(t) \rangle$ and $\langle \hat{V}_{jk}(t)\hat{V}_{mn}(\tau) \rangle$ (see Fig. 2.4). More specifically, those quantities, and as a result the memory kernel, become shorter lived with increasing temperature, thereby making the convolutionless approximation more valid. This may also be the reason for previously made claims regarding the accuracy of the time-local approximation,[51,86] since this approximation does indeed become valid at sufficiently high temperatures.

In Fig. 2.5, we show the electronic population difference as a function of time for different values of the shift in primary mode equilibrium position between the donor and acceptor states, y_0. The differences between the predictions of the four different OD-QMEs is seen to diminish with increasing y_0. This can be traced back to the fact that $\langle \hat{V}_{jk}(t) \rangle$ and $\langle \hat{V}_{jk}(t)\hat{V}_{mn}(\tau) \rangle$ become shorter-lived with increasing y_0, which corresponds to stronger coupling between the electronic system and nuclear bath DOF (see Fig. 2.6).

We now consider the temporal behavior of $\langle \hat{V}_{DA}(t) \rangle$, $\langle \hat{V}_{DA}(t)\hat{V}_{AD}(\tau) \rangle$, $\langle \hat{V}_{AD}(t)\hat{V}_{DA}(\tau) \rangle$, $\langle \hat{V}_{DA}(t)\hat{V}_{DA}(\tau) \rangle$, and $\langle \hat{V}_{AD}(t)\hat{V}_{AD}(\tau) \rangle$, depicted in Figs. 2.4 and 2.6. We start with $\langle \hat{V}_{DA}(t) \rangle$, which is explicitly given by $\langle \hat{V}_{DA}(t) \rangle = \Gamma^2 \mathrm{Tr}_{\mathrm{B}}[\hat{\rho}_{\mathrm{B}}(0) e^{i\hat{H}_D t/\hbar} e^{-i\hat{H}_A t/\hbar}]$. The lifetime of this quantity is determined by the time scale of electronic dephasing, which we will denote by τ_d. As expected, τ_d becomes longer with decreasing temperature and coupling strength between the electronic DOFs and the primary mode (see Figs. 2.4 and 2.6, top row).

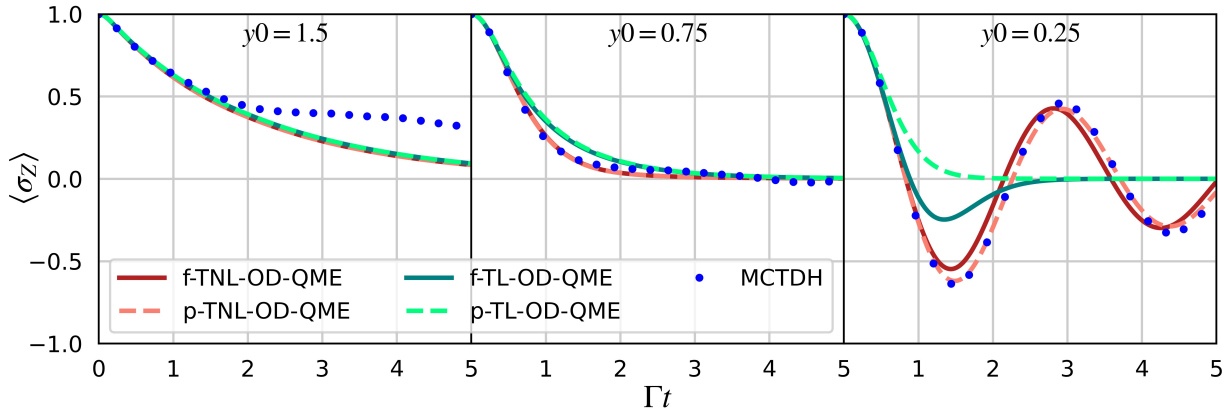


Figure 2.5: Electronic population difference as a function of time obtained using f-TNL-OD-QME, p-TNL-OD-QME, f-TL-OD-QME and p-TL-OD-QME, with $y_0 = \{0.25, 0.75, 1.5\}$ and $\beta = 1$. See Table. 2.2 for the values of other parameters. Also shown are numerically exact MCTDH-based results.

Next consider $\langle \hat{V}_{DA}(t)\hat{V}_{AD}(\tau)\rangle$, which is explicitly given by

$$\begin{aligned} &\langle \hat{V}_{DA}(t)\hat{V}_{AD}(\tau)\rangle \\ &= \Gamma^2 \mathrm{Tr}_\mathrm{B}\left[\left(e^{-\frac{i}{\hbar}\hat{H}_D t}\hat{\rho}_\mathrm{B}(0)e^{\frac{i}{\hbar}\hat{H}_D t}\right)\left(e^{-\frac{i}{\hbar}\hat{H}_A(t-\tau)}e^{\frac{i}{\hbar}\hat{H}_D(t-\tau)}\right)\right] \end{aligned} \tag{2.15}$$

In our case $\hat{\rho}_\mathrm{B}(0) = e^{-\beta\hat{H}_D}/Z_D$, which implies that $e^{-i\hat{H}_D t/\hbar}\hat{\rho}_\mathrm{B}(0)e^{i\hat{H}_D t/\hbar} = \hat{\rho}_\mathrm{B}(0)$, consistent with the fact that $\langle \hat{V}_{DA}(t)\hat{V}_{AD}(\tau)\rangle$ is independent of t (see Figs. 2.4 and 2.6). At the same time, and similarly to $\langle \hat{V}_{DA}(t)\rangle$, the lifetime of $\langle \hat{V}_{DA}(t)\hat{V}_{AD}(\tau)\rangle$ along the $t-\tau$ axis is determined by the electronic dephasing time scale τ_d due to the $e^{-i\hat{H}_A(t-\tau)/\hbar}e^{i\hat{H}_D(t-\tau)/\hbar}$ term, which is also confirmed by the results (see Figs. 2.4 and 2.6).

Next consider $\langle \hat{V}_{AD}(t)\hat{V}_{DA}(\tau)\rangle$, which is given by

$$\begin{aligned} &\langle \hat{V}_{AD}(t)\hat{V}_{DA}(\tau)\rangle \\ &= \Gamma^2 \mathrm{Tr}_\mathrm{B}\left[\left(e^{-\frac{i}{\hbar}\hat{H}_A t}\hat{\rho}_\mathrm{B}(0)e^{\frac{i}{\hbar}\hat{H}_A t}\right)\left(e^{-\frac{i}{\hbar}\hat{H}_D(t-\tau)}e^{\frac{i}{\hbar}\hat{H}_A(t-\tau)}\right)\right] \end{aligned} \tag{2.16}$$

In this case $e^{-i\hat{H}_A t/\hbar}\hat{\rho}_\mathrm{B}(0)e^{i\hat{H}_A t/\hbar} \neq \hat{\rho}_\mathrm{B}(0)$ is time dependent, consistent with the fact that $\langle \hat{V}_{AD}(t)\hat{V}_{DA}(\tau)\rangle$ is t-dependent during the time period in which the system relaxes to its equilibrium state on the acceptor PES, $e^{-\beta\hat{H}_A}/Z_A$ (see Figs. 2.4 and 2.6). Denoting the time scale for this relaxation process as τ_r, we see that like τ_d, τ_r increases with decreasing temperature and coupling strength between the electronic and nuclear DOFs. For example, $\Gamma\tau_r \sim 3$ for $y_0 = 1.5$, while

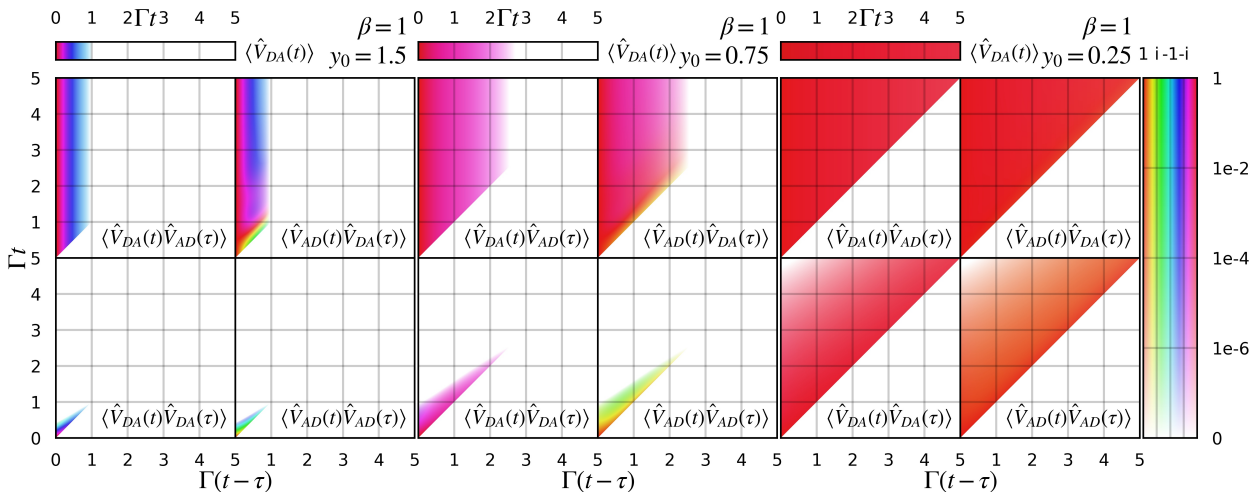


Figure 2.6: $\langle \hat{V}_{ij}(t) \rangle$ and $\langle \hat{V}_{ij}(t)\hat{V}_{kl}(\tau) \rangle$ as a function of t and $(t, t-\tau)$, respectively, where $i, j, k, l \in \{D, A\}$, for the GOA model with $\beta = 1$ and $y_0 = \{1.5, 0.75, 0.25\}$. See Table.2.2 for the values of other parameters. The intensity stands for the modulus, while the hue stands for the phase. The values are normalized so that $\langle \hat{V}_{ij}(0) \rangle = \langle \hat{V}_{ij}(0)\hat{V}_{kl}(0) \rangle = 1$. The diagonal line represents $\tau = 0$, and the lower triangle portion is set to zero by definition.

$\Gamma\tau_r \sim 4$ for $y_0 = 0.75$ (see Fig. 2.4). Similarly to $\hat{V}_{DA}(t)\hat{V}_{AD}(\tau)\rangle$, the lifetime of $\langle \hat{V}_{AD}(t)\hat{V}_{DA}(\tau) \rangle$ along the $t - \tau$ axis is determined by the electronic dephasing time scale τ_d.

Finally, consider $\langle \hat{V}_{DA}(t)\hat{V}_{DA}(\tau) \rangle$ and $\langle \hat{V}_{AD}(t)\hat{V}_{AD}(\tau) \rangle$, which are explicitly given by

$$\langle \hat{V}_{DA}(t)\hat{V}_{DA}(\tau) \rangle \tag{2.17}$$
$$= \Gamma^2 \mathrm{Tr}_\mathrm{B} \left[\hat{\rho}_\mathrm{B}(0) \left(e^{\frac{i}{\hbar}\hat{H}_D t} e^{-\frac{i}{\hbar}\hat{H}_A t} \right) \left(e^{\frac{i}{\hbar}\hat{H}_D \tau} e^{-\frac{i}{\hbar}\hat{H}_A \tau} \right) \right]$$
$$\langle \hat{V}_{AD}(t)\hat{V}_{AD}(\tau) \rangle \tag{2.18}$$
$$= \Gamma^2 \mathrm{Tr}_\mathrm{B} \left[\hat{\rho}_\mathrm{B}(0) \left(e^{\frac{i}{\hbar}\hat{H}_A t} e^{-\frac{i}{\hbar}\hat{H}_D t} \right) \left(e^{\frac{i}{\hbar}\hat{H}_A \tau} e^{-\frac{i}{\hbar}\hat{H}_D \tau} \right) \right]$$

The lifetimes of those quantities along the t and $t - \tau$ axes are similar, and given by τ_d. This is also consistent with the fact that, unlike $\langle \hat{V}_{DA}(t)\hat{V}_{AD}(\tau) \rangle$ and $\langle \hat{V}_{AD}(t)\hat{V}_{DA}(\tau) \rangle$, $\langle \hat{V}_{DA}(t)\hat{V}_{DA}(\tau) \rangle$ and $\langle \hat{V}_{AD}(t)\hat{V}_{AD}(\tau) \rangle$ decay slower along the $\tau = 0$ line (see Figs. 2.4 and 2.6).

The observations regarding the temporal behavior of $\langle \hat{V}_{DA}(t) \rangle$, $\langle \hat{V}_{DA}(t)\hat{V}_{AD}(\tau) \rangle$, $\langle \hat{V}_{AD}(t)\hat{V}_{DA}(\tau) \rangle$, $\langle \hat{V}_{DA}(t)\hat{V}_{DA}(\tau) \rangle$, and $\langle \hat{V}_{AD}(t)\hat{V}_{AD}(\tau) \rangle$ described above imply that the

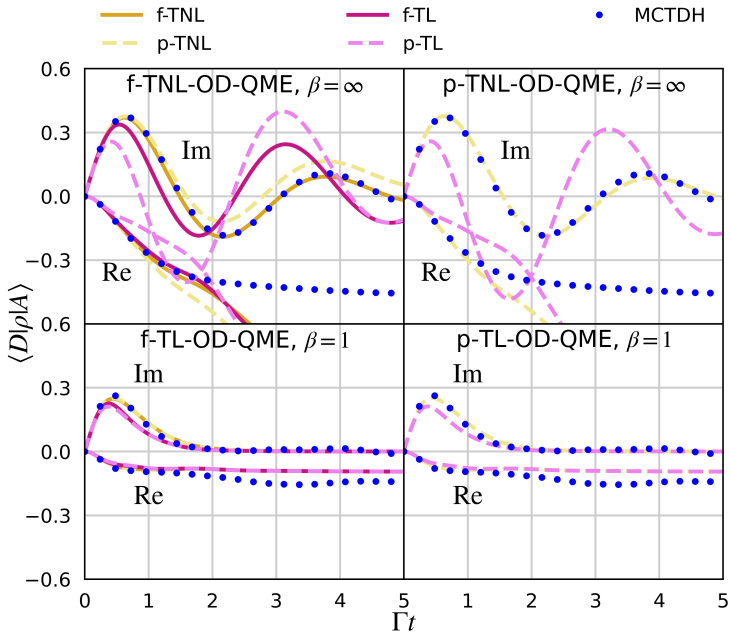


Figure 2.7: Schrödinger picture coherences as a function of time obtained by applying Eq. 1.14a and its time convolutionless counterparts to the f-TNL-OD-QME (left column) or p-TNL-OD-QME (right column) with $\beta = \{\infty, 1\}$. See Table.2.2 for the values of other parameters. Also shown are numerically exact MCTDH-based results.

TNL- and TL-OD-QMEs can be written in the following form at long times $t > \tau_d, \tau_r$:

$$\frac{\mathrm{d}}{\mathrm{d}t}\tilde{\sigma}(t > \tau_d, \tau_r) = -\frac{1}{\hbar^2}\int_0^\infty \mathrm{d}s\, \mathcal{K}(s)\tilde{\sigma}(t-s) \tag{2.19}$$

$$\frac{\mathrm{d}}{\mathrm{d}t}\tilde{\sigma}(t > \tau_d, \tau_r) = -\frac{1}{\hbar^2}\left(\int_0^\infty \mathrm{d}s\, \mathcal{K}(s)\right)\tilde{\sigma}(t) \tag{2.20}$$

Here $\mathcal{K}(s)$ is the late-time memory kernel that depends only on $s = t - \tau$. It should be noted that Eqs. 2.19 and 2.20 are stationary, since the rates do not depend explicitly on t. The accuracy of other QMEs in this stationary regime has been reported previously to be inconsistent with the short-time accuracy,[117,118] and has been shown to be of lower order than the short-time dynamics in the case of Redfield QMEs.[118] We see a similar behavior in the case of OD-QME, where the four OD-QMEs are seen to coincide in the stationary regime, but residual errors remain (see Fig. 2.3, 3rd and 4th row; and Fig. 2.5, left panel).

Lastly, in Fig. 2.7, we compare the full-density-matrix and the population-only variations of Eqs. 1.14a, and their convolutionless counterparts, regarding their ability to reproduce Schrödinger picture coherence from interaction picture electronic inputs generated by either full-tc-OD-QME or p-tc-OD-QME, at absolute zero ($\beta = \infty$) or at a relatively high temperature ($\beta = 1$). The results in this figure confirm previously discussed trends, namely the superior accuracy of predictions

based on the time-nonlocal methods compared to their time-local counterparts, the superior accuracy of predictions based on the full-density-matrix methods compared to their population-only counterparts, and an overall improved accuracy with increasing temperature.

2.6 Concluding Remarks

In this chapter, we focused on a family of OD-QMEs, which are based on treating the coupling between electronic states (in the localized exciton basis) as a small perturbation, within the framework of second-order perturbation theory. Combining the choices of projection operators (full reduced density matrix vs. electronic populations), and the choice between the TNL and TL forms, four different OD-QMEs are tested here (see Table 2.1).

The accuracy of the different types of OD-QMEs and the procedure for obtaining Schrödinger-picture electronic coherences from interaction-picture electronic inputs was tested on the GOA benchmark model for charge transfer in the condensed phase, across a relatively wide parameter range. The results show that TNL-OD-QMEs can produce significantly more accurate predictions for both electronic populations and Schrödinger-picture coherences than their TL counterparts, particularly when the electronic observables of interest are chosen as the electronic populations. The discrepancy between the TNL- and TL-OD-QMEs can be traced back to increasing memory times with decreasing temperature (see Fig. 2.4) or decreasing coupling between the electronic system and the primary mode (see Fig. 2.6). It should be noted that previous studies found that TL-QMEs are not always less accurate than their TNL counterparts.[94,119] However, we find that this is the case in the case of the OD-QMEs under consideration in this paper, at least for the GOA model.

CHAPTER 3

Simulating Electronic Absorption Spectrum via Off-Diagonal Quantum Master Equation

3.1 Introduction

Electronic spectroscopy is one of the main experimental probes of electronic observables..[2,120–145] In the context of reduced electronic dynamics, simulating spectra calls for simulating the dynamics of electronic coherence in the Schrödinger picture. As a result, previous applications of projection-based methods to simulate spectra has been restricted to either Redfield-type TNL-QME which propagates in the Schrödinger picture and therefore can be applied directly, or in the case of OD-QME, it is applied only to generate the population transfer tensor (or its TNL analogue), whereas the coherences are extracted with the help of further approximations such as the secular approximation.[97,99,146,147]

Our recently proposed and tested projection-based technique to retrieve Schrödinger picture coherences from the interaction picture inputs, Eq. 1.14a,[103] made it possible to simulate electronic spectra via OD-QME directly. In this chapter, we take the first step towards achieving this goal by applying TNL- and TL-OD-QME to simulate the electronic absorption spectra for a biexciton model system, the results are compared against a Redfield-style TL-QME and numerically exact hierarchy equation of motion (HEOM) method.

3.2 Molecular Aggregate Hamiltonian and the Simulation of Absorption Spectra

In this chapter, we consider a molecular aggregate system made out of two-state molecules described by the Frenkel-exciton Hamiltonian

$$\hat{H} = \sum_j \hat{H}_j^g \hat{B}_j \hat{B}_j^\dagger + \sum_j \left(\Delta_j + \hat{H}_j^e\right) \hat{B}_j^\dagger \hat{B}_j + \sum_{j \neq k} \Gamma_{jk} \hat{B}_j^\dagger \hat{B}_k \,, \tag{3.1}$$

where $\hat{B}_j^\dagger(\hat{B}_j)$ are exciton creation (annihilation) operators for the j-th molecule, which satisfy $[\hat{B}_j, \hat{B}_k^\dagger] = \delta_{jk}(1 - 2\hat{B}_j^\dagger \hat{B}_j)$ and $\hat{B}_j \hat{B}_j = 0$. The band gap $\hbar\omega_0$ is omitted from the Hamiltonian because we are working in a rotating frame of the same frequency, see appendix D. Similar to Chpt. 2, we again assume that the Condon approximation is valid such that Γ_{jk} are constant and correspond to the only coupling between localized excitons. $\hat{H}_j^g(\hat{H}_j^e)$ are the nuclear Hamiltonian for the ground (excited) state of the j-th molecule.

The electronic absorption lineshape function, $I(\omega)$, can be obtained from the dipole-dipole correlation function $C(t)$:

$$I(\omega) = \mathrm{Re} \int_0^\infty \mathrm{d}t \, C(t) e^{i\omega t} \tag{3.2a}$$

$$C(t) = \mathrm{Tr}\left[\hat{\mu}_\mathrm{u} e^{-\frac{i}{\hbar}\hat{H}t} \hat{\mu} \hat{\rho}^\mathrm{eq} e^{\frac{i}{\hbar}\hat{H}t}\right] . \tag{3.2b}$$

Here, $\hat{\rho}^\mathrm{eq} = \prod_j Z^{-1} \exp(-\beta \hat{H}_j^g) \hat{B}_j \hat{B}_j^\dagger$ is the ground state equilibrium density operator. The polarization operator is $\hat{\mu} = \hat{\mu}_\mathrm{u} + \hat{\mu}_\mathrm{u}^\dagger$, where $\hat{\mu}_\mathrm{u} = \sum_j \mu_j \hat{B}_j$. The introduction of $\hat{\mu}_\mathrm{u}$ results from the rotating frame and the rotating wave approximation (RWA) (see appendix. D), where the band gap is assumed to be much larger than the detuning and electronic coupling.

Since the dipole operator is purely electronic, we can cast the correlation function into the form $C(t) = \mathrm{Tr}_e[\hat{\mu}_\mathrm{u} \hat{\zeta}(t)]$, where a reduced operator $\hat{\zeta}(t) = \mathrm{Tr}_N[\exp(-i\hat{H}t\hbar^{-1}) \hat{\mu} \hat{\rho}^\mathrm{eq} \exp(i\hat{H}t\hbar^{-1})]$ is propagated using OD-QME. For the purpose of QME, it would be convenient to define an electronic basis, which in the context of absorption spectrum would only include the ground state $|0\rangle$, as well as the one-exciton states $\{|j\rangle\}$ where $|j\rangle$ corresponds to the j-th site excited while the remaining sites are in the ground state. For the rest of the current chapter, we will be working in this site-local basis. As required by OD-QME, the off-diagonal part of the Hamiltonian, Eq. 3.1, is treated as a small perturbation:

$$\hat{H}_\mathrm{I} = \sum_{j \neq k} \Gamma_{jk} \hat{B}_j^\dagger \hat{B}_k = \sum_{j \neq k} \Gamma_{jk} |j\rangle\langle k| \tag{3.3}$$

To calculate the correlation function, Eq. 3.2b, we notice that only the lower-triangle inter-band coherences $|j\rangle\langle 0|$ are populated immediately after interacting with the dipole,

$$\hat{\zeta}(0) = \hat{\mu}|0\rangle\langle 0| = \sum_j \mu_j |j\rangle\langle 0| \,, \tag{3.4}$$

hence only f-TNL-OD-QME and f-TL-OD-QME are used to evaluate the correlation function, because the initial state condition Eq. 1.6 is not fulfilled in the case of population-only projection.

To obtain the inter-band coherence using OD-QME, previously reported methods[99,146,147] separate the broadening of lineshape into broadening due to population transfer, which can be obtained using OD-QME, and pure dephasing. The latter is approximated to be the relaxation of coherence under the influence of only $\hat{H}_0$, i.e. without population transfer. This introduces further approximations including the secular approximation, the assumption that $\exp(-\frac{i}{\hbar}\hat{H}_j^g t)\exp(\frac{i}{\hbar}\hat{H}_j^e t) = 1$, and the Markovian limit.

Since the field-free Hamiltonian, Eq. 3.1, does not include inter-band coupling, the lower-triangle inter-band coherences $\zeta_{j0}(t)$ remain the only non-vanishing matrix elements throughout the time span of the dynamics. As a result, the relevant matrix elements of the QME superoperators $\langle\mathcal{L}_{\rm I}(t)\rangle_{\mathcal{P}}$, $\mathcal{K}_{\mathcal{P}}(t,\tau)$, $\langle\mathcal{G}_0(t)\rangle$, and $\bar{\mathcal{K}}(t,\tau)$ are limited to the couplings between lower-triangle inter-band coherences, explicitly given by

$$\langle\mathcal{L}_{\rm I}(t)\rangle_{j0,k0} = \Gamma_{jk} C_j^*(t) C_k(t) \tag{3.5a}$$

$$\mathcal{K}_{j0,k0}(t,\tau) = \sum_{l\neq j,k} \Gamma_{j,l}\Gamma_{l,k}\Big[C_l(t-\tau) - C_l(t)C_l^*(\tau)\Big] C_j^*(t) C_k(\tau) \tag{3.5b}$$

$$\langle\mathcal{G}_0(t)\rangle_{j0,k0} = \delta_{j,k} C_j(t) \tag{3.5c}$$

$$\bar{\mathcal{K}}_{j0,k0}(t,s) = \Gamma_{jk}\Big[C_j(t-\tau) - C_j(t)C_j^*(\tau)\Big] C_k(\tau) \,. \tag{3.5d}$$

Hence, all superoperators can be obtained from the single-molecule correlation functions

$$C_j(t) = e^{-\frac{i}{\hbar}\Delta_j t}\Big[e^{\frac{i}{\hbar}\hat{H}_j^g t} e^{-\frac{i}{\hbar}\hat{H}_j^e t}\frac{1}{Z} e^{-\beta\hat{H}_j^g}\Big] \,. \tag{3.6}$$

In the current chapter, the nuclear Hamiltonians $\hat{H}_j^g$, $\hat{H}_j^e$ are assumed to take harmonic forms

$$\hat{H}_j^g = \frac{1}{2}\sum_\alpha \hat{p}_{j,\alpha}^2 + \omega_{j,\alpha}^2 \hat{q}_{j,\alpha}^2 \tag{3.7a}$$

$$\hat{H}_j^e = \frac{1}{2}\sum_\alpha \hat{p}_{j,\alpha}^2 + \omega_{j,\alpha}^2 \Big(\hat{q}_{j,\alpha} - R_{j,\alpha}\Big)^2 \,, \tag{3.7b}$$

where the frequencies $\{\omega_\alpha\}$ and excitation displacement $\{R_\alpha\}$ are defined via the spectral density

$$J_j(\omega) = \frac{\pi}{2}\sum_\alpha \omega_{j,\alpha}^3 R_{j,\alpha}^2 \delta\Big(\omega - \omega_{j,\alpha}\Big) \,. \tag{3.7c}$$

Given the harmonic form of $\hat{H}_j^g$ and $\hat{H}_j^e$, the single-molecule correlation functions, Eq. 3.6, can be calculated in a closed form utilizing multidimensional Gaussian integrals:[45,103,114] (the molecule index subscript j is omitted on the RHS)

$$\begin{aligned} C_j(t) = e^{-\frac{i}{\hbar}\Delta t} \exp\Big\{ -i\sum_\alpha \frac{\omega_\alpha R_\alpha^2}{2\hbar}\sin(\omega_\alpha t)\Big\} \\ \exp\Big\{\sum_\alpha \frac{\omega_\alpha R_\alpha^2}{2\hbar}\coth(\frac{1}{2}\beta\hbar\omega_\alpha)[\cos(\omega_\alpha t) - 1]\Big\} \,. \end{aligned} \tag{3.8}$$

3.3 Model Parameters and Method Details

In this section, we compare the absorption spectra , Eq. 3.2a for a Frenkel biexciton model, calculated using TNL- and TL-OD-QME, as well as a Redfield-type TL-QME and a numerically exact method.

The Frenkel biexciton model consists of two molecules, resulting in three electronic states (one ground state and two singly-excited states). The two transition dipole dipole vectors are assumed to be anti-parallel, such that $\mu_1/\mu_2 = -5$. The detunings are set to be $\Delta_1 = 100\ \mathrm{cm}^{-1}$ and $\Delta_2 = -100\,\mathrm{cm}^{-1}$

We assume the two molecules to have identical spectral density, which is chosen to be of Ohmic form with Lorentzian cutoff,

$$J_1(\omega) = J_2(\omega) = 2\lambda\frac{\omega_c\omega}{\omega_c^2 + \omega^2} \,, \tag{3.9}$$

where λ is the reorganization energy of single-molecule excitation, and ω_c is the cutoff frequency. Each molecule is discretized to have 50 modes, following the discretization procedure outlined in appendix B (see also Ref. 148), resulting a total of 100 molecular DOF.

In the following section two types of molecule will be examined: a slow case $\omega_c = 18\ \mathrm{cm}^{-1}$ and a fast case $\omega_c = 200\,\mathrm{cm}^{-1}$. For both settings, we will explore the parameter space for λ, which corresponds to the coupling between electronic and nuclear DOF (i.e. system-bath coupling), as well as the electronic coupling, $\Gamma_{12} \equiv \Gamma$.

Aside from TNL-OD-QME and TL-OD-QME, results from a TL Redfield QME and the numerically exact hierarchy of equations of motion (HEOM) method are included for comparison. Both the Redfield QME (referred to as the TCL method in the package) and HEOM are generated

using the open-source pyrho package.[149]

3.4 Absorption Spectra

We start from the case of slow bath $\omega_c = 18\ \mathrm{cm}^{-1}$ at $T = 72\ \mathrm{K}$, for which the frequency-domain absorption spectra is shown in Fig. 3.1. The reorganization energy λ increases from left column to right column, while the electronic coupling Γ increases from top row to bottom row.

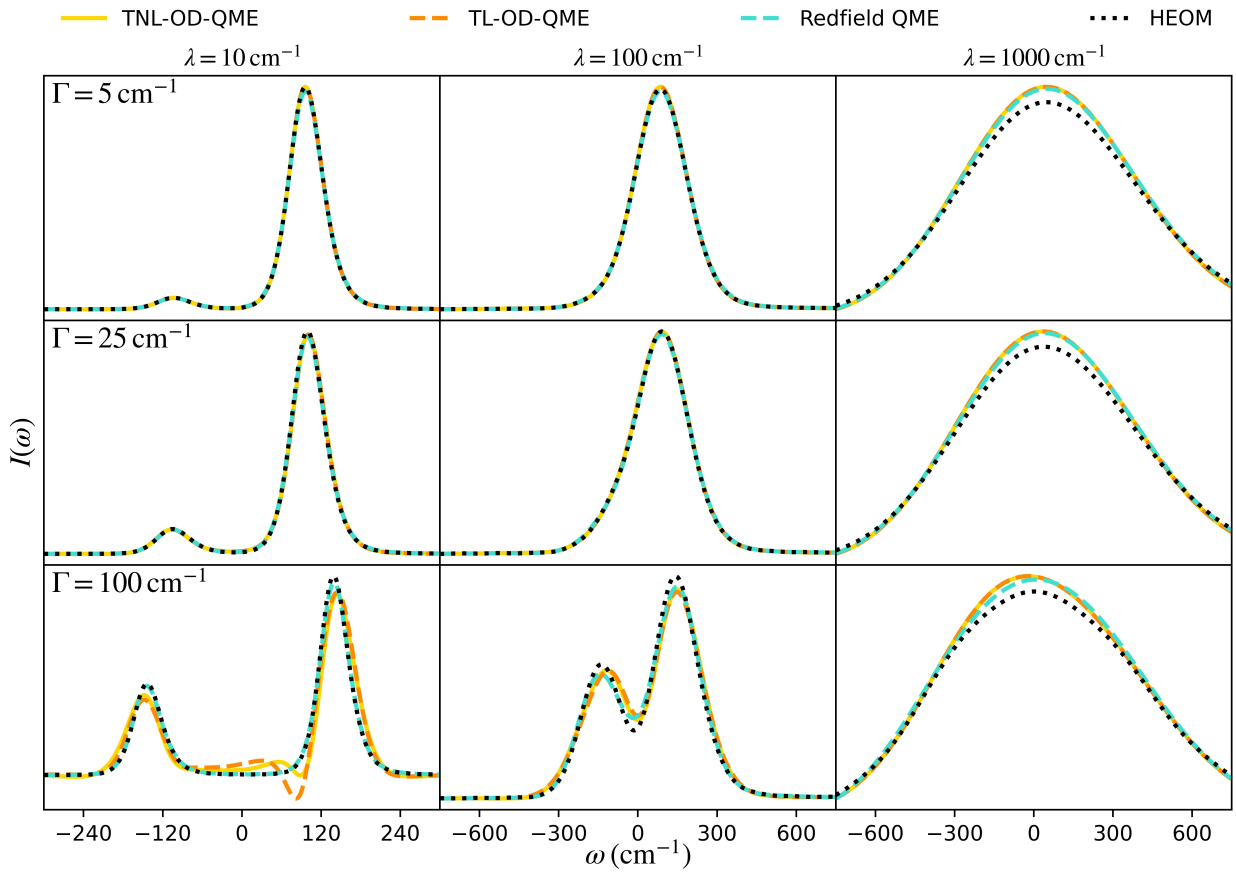


Figure 3.1: The absorption spectra for the slow bath and low temperature case ($\omega_c = 18\ \mathrm{cm}^{-1}$, $T = 72\ \mathrm{K}$). The reduced dynamics is obtained using one of three QMEs, or the numerically exact HEOM. From top row to bottom row, in order: $\Gamma = 5\ \mathrm{cm}^{-1}$, $\Gamma = 25\ \mathrm{cm}^{-1}$, and $\Gamma = 100\ \mathrm{cm}^{-1}$; from left column to right column, in order: $\lambda = 10\,\mathrm{cm}^{-1}$, $\lambda = 100\,\mathrm{cm}^{-1}$, and $\lambda = 1000\,\mathrm{cm}^{-1}$. The spectra are calculated without re-normalization.

Unsurprisingly, the correlation function becomes more damped and shorter-lived as λ becomes larger, which corresponds to stronger system-bath coupling, leading to faster decoherence and broader absorption peaks. The smaller left peak, which corresponds to the weaker transition $0 \to 2$,

becomes more prominent as the electronic coupling Γ becomes stronger, and better facilitates the coherence transfer from σ_{10} to σ_{20}.

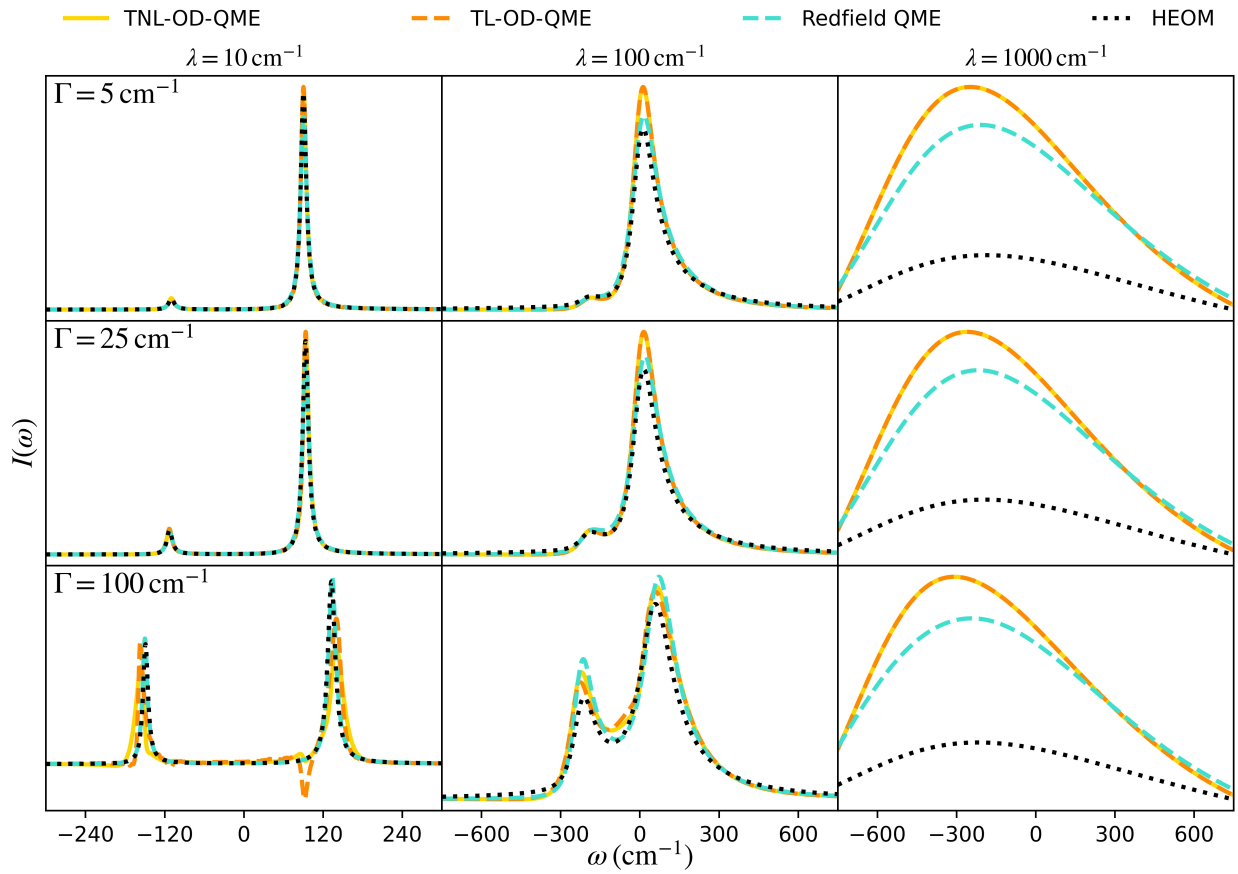


Figure 3.2: The absorption spectra for the fast bath and low temperature case ($\omega_c = 200\ \mathrm{cm}^{-1}$, $T = 72\ \mathrm{K}$). The reduced dynamics is obtained using one of three QMEs, or the numerically exact HEOM. From top row to bottom row, in order: $\Gamma = 5\ \mathrm{cm}^{-1}$, $\Gamma = 25\ \mathrm{cm}^{-1}$, and $\Gamma = 100\ \mathrm{cm}^{-1}$; from left column to right column, in order: $\lambda = 10\,\mathrm{cm}^{-1}$, $\lambda = 100\,\mathrm{cm}^{-1}$, and $\lambda = 1000\,\mathrm{cm}^{-1}$. The spectra are calculated without re-normalization.

The lineshape predicted by TL Redfield QME agrees well with the exact result, even in the case of strong system-bath coupling, which the Redfield theory treats as a small perturbation. It has been previously shown that the *Markovian* Redfield theory leads to much broader spectra than expected in the case of a slow bath,[150,151] this shows that the source of this error is almost entirely the non-Markovianity of the slow bath, instead of the system-bath coupling.

The lineshape predicted by both TL- and TNL-OD-QME also agrees well with the exact result along all of the examined parameter space, and only deviates slightly from the exact spectra in the case of strong electronic coupling $\Gamma = 100\ \mathrm{cm}^{-1}$, which OD-QME treats perturbatively. Additionally, TNL-OD-QME and TN-OD-QME spectra differ slightly in the weak system-bath and

strong electronic coupling case (Fig. 3.1, lower left panel). In chapter 2, it is shown that weaker system-bath coupling leads to longer-living single-molecule correlation functions, Eq. 3.6 and 3.8, which strengthens the time-nonlocality of the EOM, leading to a discrepancy between TNL- and TL-OD-QME.[103] Inspecting the explicit form of the EOM, Eq. 3.5, we notice that since the electronic coupling Γ acts as a prefactor in the superoperators, the time-locality induced difference in $C_j(t)$ is magnified by the electronic coupling.

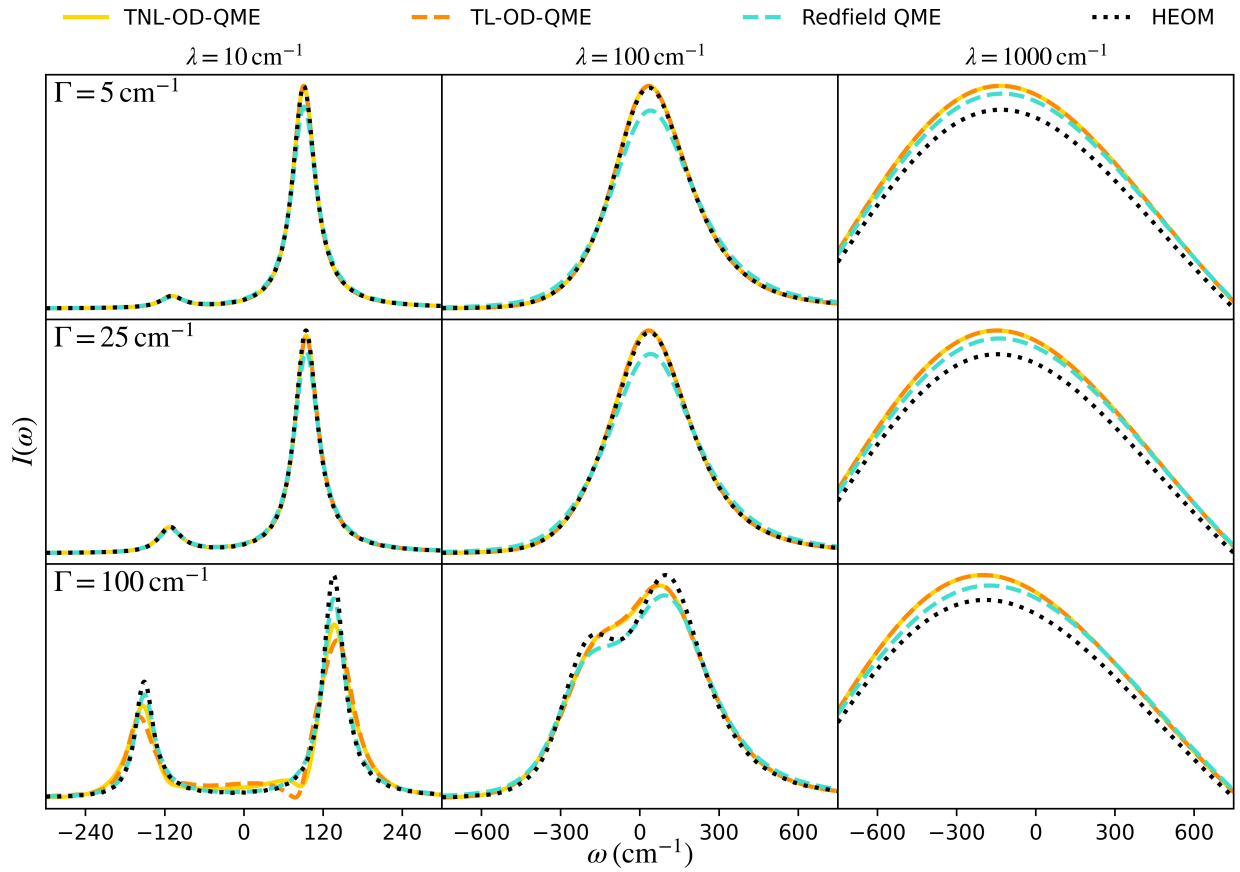


Figure 3.3: The absorption spectra for the fast bath and high temperature case ($\omega_c = 200\ \mathrm{cm}^{-1}$, $T = 300\,\mathrm{K}$). The reduced dynamics is obtained using one of three QMEs, or the numerically exact HEOM. From top row to bottom row, in order: $\Gamma = 5\ \mathrm{cm}^{-1}$, $\Gamma = 25\ \mathrm{cm}^{-1}$, and $\Gamma = 100\ \mathrm{cm}^{-1}$; from left column to right column, in order: $\lambda = 10\,\mathrm{cm}^{-1}$, $\lambda = 100\,\mathrm{cm}^{-1}$, and $\lambda = 1000\,\mathrm{cm}^{-1}$. The spectra are calculated without re-normalization.

We next consider the case of fast bath $\omega_c = 200\ \mathrm{cm}^{-1}$ at $T = 72\ \mathrm{K}$, for which the frequency-domain absorption spectra is shown in Fig. 3.2. The fast bath turns out to be more challenging for the QMEs. In the case of weak and intermediate system-bath coupling ($\lambda = 10\ \mathrm{cm}^{-1}$ and $100\ \mathrm{cm}^{-1}$), all three QMEs capture the shapes of peaks rather well, albeit not as accurate as the slow bath case. As expected, both OD-QME are more accurate when the electronic coupling Γ is

weak, while the aforementioned time-locality induced error, i.e. the discrepancy between TL- and TNL-OD-QME, again manifests with strong electronic coupling (Fig. 3.2, lower left panel).

In the case of strong system-bath coupling ($\lambda = 1000\ \mathrm{cm}^{-1}$, see Fig. 3.2, left column), all three QMEs significantly overestimates the strength of the peak. This is especially surprising for OD-QME, because this error shows no dependence on its perturbative parameter Γ, and a strong system-bath coupling leads to highly time-local dynamics, rendering time-locality induced error unlikely.

Lastly, consider the case of fast bath at a high temperature $\omega_\mathrm{c} = 200\ \mathrm{cm}^{-1}$ at $T = 300\ \mathrm{K}$, for which the frequency-domain absorption spectra is shown in Fig. 3.3. Unsurprisingly, the higher temperature leads to inhomogeneous broadening of the spectra. On the other hand, lineshapes predicted by all three QMEs agree well with the exact result, this includes the strong system-bath coupling case ($\lambda = 1000\ \mathrm{cm}^{-1}$, see Fig. 3.3, left column), which the QMEs are wildly inaccurate at low temperature. The fact that this error manifests at low temperature and high bath frequency suggests that strong coupling to a quantum bath affects the accuracy of QMEs, although they require no classical treatment to the bath EOM.

Overall, there is no case in which OD-QME significantly outperforms Redfield QME, even when system-bath coupling is strong. In other words, the OD-QME seems to be more sensitive to increasing electronic coupling than Redfield is to system-bath coupling. The possible reason to this behavior is that while both OD- and Redfield QME are second order in terms of the respective interactions $\hat{H}_\mathrm{I}$, for OD-QME an extra step, Eq. 1.14a, was added to retrieve the Schrödinger picture, which is *first* order in $\hat{H}_\mathrm{I}$, making OD-QME less resistant to increasing electronic coupling.

3.5 Concluding Remarks

Quantum master equations are known to be a useful family of reduced dynamics methods in the simulation of electronic spectra, which in the dipole approximation relies heavily on simulating the dynamics of inter-band coherences. Redfield-type QMEs, which treat the system-bath coupling as a perturbation, is performed in the Schrödinger picture and generates coherence dynamics directly. OD-QME, including modified Redfield theory and QME in the Förster regime, treats the off-diagonal part of the Hamiltonian as a perturbation and hence propagates in the interaction picture. As a result, OD-QME can only be used to obtain population dynamics directly, and the coherence has to be extracted by applying further approximations.

In this chapter, we apply the projection-based technique that generates Schrödinger picture dynamics from interaction picture dynamics,[50,103] to simulate electronic absorption spectrum via TNL- and TL-OD-QME. A harmonic Frenkel biexciton model is used as the benchmark system, and the OD-QME spectra is compared to a non-Markovian TL Redfield QME, and numerically

exact HEOM. Overall, OD-QME shows comparable accuracy to Redfield QME, its error increases somewhat with increasing electronic coupling strength, but OD-QME stays rather accurate even in the presence in strong electronic coupling. Using TNL-OD-QME instead of TL-OD-QME provides little improvement in most cases, with the only exception being the case of weak system-bath coupling and strong electronic coupling, where TNL-OD-QME is slightly more accurate. We believe this is the combined result of weak system-bath coupling leading to a longer living memory kernel, and strong electronic coupling magnifying this time-nonlocality induced difference. All three QMEs fail to capture the lineshape with a high-frequency bath at a low temperature. The cause of this error is unlikely to be either the perturbative nature of the method, or the time-nonlocality of the dynamics. We conclude that this error may be linked to the quantum behavior of the bath, further investigation of this phenomenon in QME remains an open question.

CHAPTER 4

An Efficient Approach for Calculating Cavity-Enhanced Charge Transfer Rate Constants

This work is done in collaboration with Dr. Max Saller

4.1 Introduction

Recent experiments have demonstrated that chemical reactions can be controlled by performing them inside of micro-cavities, taking advantage of the strong[152–157] or ultra-strong[158–161] coupling between the optical modes of the electromagnetic micro-cavities[162–165] and the molecular matter placed inside the cavity. Such ability suggests a wide range of potential utilities, including energy and charge transfer, photochemistry and catalysis, as well as manipulating optical and electrical properties, nonlinear optical response and reactivity.[156,158,166–200]

These experimental advances call for the development of accurate and cost-effective computational methods for simulating the dynamics of molecular matter inside cavities. In this chapter, the cavity-induced enhancement of charge transfer (CT) rates for a benchmark model is studied using equilibrium Fermi's golden rule (EFGR, Eq. 2.10), which is the Markovian limit of p-TL-OD-QME. While a straightforward approach to this problem would involve propagating the material system together with the cavity DOF to evaluate the correlation functions Eq. 2.7a, we found that the cavity-enhanced CT rate constant can be expressed by a sum of the cavity-free rate constant and a correction term, which can be obtained from the cavity-free rate constant where the energy gap of the reaction is shifted by the cavity frequency. Hence, the cavity-enhanced CT rate constant can be evaluated from the cavity-free rate constant with minimal additional effort.

4.2 Model Hamiltonian

In the current chapter, we consider the benchmark model Hamiltonian of a molecular system undergoing CT while being coupled to a single cavity mode that was recently studied by Huo *et al.*[201]

The full light-matter Hamiltonian is given by

$$\begin{aligned}\hat{H} = &-\varepsilon|A\rangle\langle A| + \Delta\big(|D\rangle\langle A| + |A\rangle\langle D|\big) \\ &+ \frac{\hat{P}_{\mathrm{s}}^2}{2M_{\mathrm{s}}} + \sum_{\alpha\in\{D,A\}} \frac{1}{2}M_{\mathrm{s}}\omega_{\mathrm{s}}^2\big(\hat{R}_{\mathrm{s}} - R_{\alpha,0}\big)^2|\alpha\rangle\langle\alpha| + \hat{H}_{\mathrm{SB}} + \hat{H}_{\mathrm{F}}\,,\end{aligned} \tag{4.1}$$

where $\varepsilon = \hbar\omega_{DA}$ is the energy gap between the diabatic donor (D) and acceptor (A) state, $\Delta = 5$ meV is the electronic coupling between the two diabatic states.

$\hat{R}_{\mathrm{s}}$, $\hat{P}_{\mathrm{s}}$, $M_{\mathrm{s}} = 0.265\,\mathrm{ps}^2$ and $\omega_{\mathrm{s}} = 9.5\,\mathrm{meV}$ correspond to the position, momentum, mass and frequency, respectively, of the primary solvent DOF which is directly coupled to the electronic DOF.

$R_{\mathrm{D},0} = 0$ and $R_{\mathrm{A},0} = \sqrt{2\lambda/f_0}$ correspond to the equilibrium geometry displacements of this DOF in the donor and acceptor states, respectively. Here, $\lambda = 950$ meV is the reorganization energy and $f_0 = 55.7$ is the force constant. $\hat{H}_{\mathrm{SB}}$ corresponds to the Hamiltonian of the bath of secondary solvent DOF, which are coupled to the primary solvent DOF, and is given by:

$$\hat{H}_{\mathrm{SB}} = \sum_{j=1}^{B}\Big[\frac{\hat{P}_j^2}{2M_j} + \frac{M_j\omega_j^2}{2}\big(\hat{R}_j - \frac{c_j}{M_j\omega_j^2}\hat{R}_{\mathrm{s}}\big)^2\Big]\,, \tag{4.2}$$

where $B = 100$ is the number of bath DOF. The position, momentum, and mass of the jth bath mode are given by R_j, P_j, and $M_j = M_{\mathrm{s}}$, respectively, and the frequency and coupling coefficient ω_j, c_j are obtained from discretizing an Ohmic spectral density of the form

$$J(\omega) = \frac{\pi}{2}\sum_{j=1}^{B}\frac{c_j^2}{M_j\omega_j}\delta(\omega-\omega_j) = \eta\omega\mathrm{e}^{-\frac{\omega}{\omega_c}}\,, \tag{4.3}$$

where $\omega_c = 9.5$ meV and $\eta = 1.066\times10^6$ a.u. are the characteristic frequency of the bath and the friction coefficient, respectively. Following Ref. 201, we adopt the discretization scheme from Ref. 202. Finally, $\hat{H}_{\mathrm{F}}$ is the field-matter Hamiltonian which is given by

$$\hat{H}_{\mathrm{F}} = \hbar\omega_{\mathrm{F}}a_{\mathrm{F}}^\dagger a_{\mathrm{F}} + \hbar g_{\mathrm{F}}\Big(|D\rangle\langle A| + |A\rangle\langle D|\Big)\Big(a_{\mathrm{F}}^\dagger + a_{\mathrm{F}}\Big)\,, \tag{4.4}$$

where ω_{F} is the frequency of the single field mode coupled to the electronic DOF of the mate-

	Model I	Model II
$\hbar g_{\mathrm{F}}$	3 meV	5 meV
$\hbar \omega_{\mathrm{F}}$	10 meV	200 meV

Table 4.1: Field mode frequency and light-matter coupling parameters for two CT in cavity Hamiltonians under consideration.

rial system, and $a_{\mathrm{F}}^{\dagger}$ and a_{F} are the corresponding photonic creation and annihilation operators, respectively. The field-matter coupling strength is given by

$$\hbar g_{\mathrm{F}} = \sqrt{\frac{\hbar \omega_{\mathrm{F}}}{2\epsilon_0 L}} \mu_{\mathrm{DA}} \, , \tag{4.5}$$

where ϵ_0 and L are the vacuum permittivity and the length of the cavity, respectively, and $\mu_{\mathrm{DA}} = \mu_{\mathrm{AD}}$ is the electronic transition dipole moment. Following Ref. 201, we present results that correspond to a temperature of $T = 300$K and for two different sets of field parameters, which correspond to the CT process following rate kinetics,[201] which will be referred to as Model I and Model II (see Table 4.1).

4.3 Cavity-Enhanced Fermi's Golden Rule Charge Transfer Rate Constant

The cavity-enhanced process of donor-to-acceptor charge-transfer is probed using EFGR (Eq. 2.10), which is p-TL-OD-QME in the Markovian limit such that the rate constant is no longer time-dependent. The FGR rate constant is given by

$$k_{DA} = \frac{1}{\hbar^2} \int_{-\infty}^{\infty} \mathrm{d}t \, C_{\mathrm{FGR}}(t) \, , \tag{4.6}$$

where the FGR correlation function is given by

$$C_{\mathrm{FGR}}(t) = \mathrm{Tr}_{NP} \left[\hat{H}_{\mathrm{I,AD}} \hat{\rho}_{\mathrm{D}}^{eq} \mathrm{e}^{\mathrm{i}\hat{H}_{\mathrm{D}} t} \hat{H}_{\mathrm{I,DA}} \mathrm{e}^{-\mathrm{i}\hat{H}_{\mathrm{A}} t} \right] \, , \tag{4.7}$$

where $\mathrm{Tr}_{NP} = \mathrm{Tr}_N \mathrm{Tr}_P$ is the trace over nuclear (that is, the primary solvent mode and the second bath modes) and photonic DOF. Following the previous applications of OD-QME, the Hamiltonian is divided into the diagonal component $\hat{H}_{\alpha} = \langle \alpha | \hat{H} | \alpha \rangle$ and the off-diagonal component $\hat{H}_{\mathrm{I,DA}} = \langle D | \hat{H} | A \rangle$ which will be treated perturbatively. The nuclear and photonic DOF are assumed to initially be in thermal equilibrium at the donor state, such that $\hat{\rho}(0) = |D\rangle\langle D| \otimes \hat{\rho}_{\mathrm{D}}^{eq}$ and $\hat{\rho}_{\mathrm{D}}^{eq} =$

$\exp(-\beta\hat{H}_{\mathrm{D}})Z^{-1}$.

We notice that the nuclear and photonic DOFs do not couple to each other directly. Hence, $\hat{H}_{\mathrm{D}}, \hat{H}_{\mathrm{A}}$, and $\hat{H}_{\mathrm{I,DA}}$ can be separated into nuclear and photonic terms:

$$\hat{H}_{\mathrm{D}} = \hat{H}_{\mathrm{N,D}} + \hat{H}_{\mathrm{F},0} \tag{4.8a}$$

$$\hat{H}_{\mathrm{A}} = -\varepsilon + \hat{H}_{\mathrm{N,A}} + \hat{H}_{\mathrm{F},0} \tag{4.8b}$$

$$\hat{H}_{\mathrm{I,DA}} = \hat{H}_{\mathrm{I,AD}} = \Delta + \hat{H}_{\mathrm{F,I}} \, . \tag{4.8c}$$

Here, the photonic Hamiltonian is cast into the form of a single harmonic oscillator, such that $\hat{R}_F = \sqrt{\frac{\hbar}{2\omega_F}}\left(\hat{a}_F + \hat{a}_F^\dagger\right)$ and $\hat{P}_F = -i\sqrt{\frac{\hbar\omega_F}{2}}\left(\hat{a}_F - \hat{a}_F^\dagger\right)$ are the photonic coordinate and momentum operators, respectively. As a result, the photonic terms are given by:

$$\hat{H}_{\mathrm{F},0} = \frac{1}{2}\left(\hat{P}_{\mathrm{F}}^2 + \omega_{\mathrm{F}}^2\hat{R}_{\mathrm{F}}^2\right) \tag{4.9a}$$

$$\hat{H}_{\mathrm{F,I}} = \sqrt{2\hbar\omega_{\mathrm{F}}}g_{\mathrm{F}}\hat{R}_{\mathrm{F}} \, . \tag{4.9b}$$

Separating the nuclear and photonic DOF into respective components, the FGR correlation function can be written as:

$$\begin{aligned} C_{\mathrm{FGR}}(t) &= e^{\frac{i}{\hbar}\varepsilon t}\mathrm{Tr}\left[\left(\Delta + \hat{H}_{\mathrm{F,I}}\right)\hat{\rho}_{\mathrm{D}}^{eq}\mathrm{e}^{\mathrm{i}\hat{H}_{\mathrm{D}}t}\left(\Delta + \hat{H}_{\mathrm{F,I}}\right)\mathrm{e}^{-\mathrm{i}\hat{H}_{\mathrm{A}}t}\right] \\ &= C_{\mathrm{FGR}}^{nc}(t) + \frac{1}{\Delta^2}C_{\mathrm{FGR}}^{nc}(t)C_{\mathrm{FGR}}^{c}(t) \end{aligned} \tag{4.10a}$$

$$C_{\mathrm{FGR}}^{nc}(t) = e^{\frac{i}{\hbar}\varepsilon t}\Delta^2\mathrm{Tr}\left[\hat{\rho}_{\mathrm{N,D}}^{eq}\mathrm{e}^{\mathrm{i}\hat{H}_{\mathrm{N,D}}t}\mathrm{e}^{-\mathrm{i}\hat{H}_{\mathrm{N,A}}t}\right] \tag{4.10b}$$

$$C_{\mathrm{FGR}}^{c}(t) = \mathrm{Tr}\left[\hat{H}_{\mathrm{F,I}}\hat{\rho}_{\mathrm{F},0}^{eq}\mathrm{e}^{\mathrm{i}\hat{H}_{\mathrm{F},0}t}\hat{H}_{\mathrm{F,I}}\mathrm{e}^{-\mathrm{i}\hat{H}_{\mathrm{F},0}t}\right] , \tag{4.10c}$$

where $C_{\mathrm{FGR}}^{nc}(t)$ is the *cavity-free* FGR correlation function, i.e.

$$k_{DA}^{nc} = \frac{1}{\hbar^2}\int_{-\infty}^{\infty}\mathrm{d}t\, C_{\mathrm{FGR}}^{nc}(t) \, , \tag{4.11}$$

whereas the cavity-only correlation function $C_{\mathrm{FGR}}^{c}(t)$ is a one-mode entity that is available in close form:

$$C_{\mathrm{FGR}}^{c}(t) = \hbar^2 g_{\mathrm{F}}^2\left[\coth(\frac{1}{2}\beta\hbar\omega_{\mathrm{F}})\cos(\omega_{\mathrm{F}}t) - i\sin(\omega_{\mathrm{F}}t)\right] . \tag{4.12}$$

The main result of the current chapter is obtained by substituting Eq. 4.12 into Eq. 4.10a, and

performing the integration:

$$k_{DA} = k_{DA}^{nc} + \frac{\hbar^2 g_{\mathrm{F}}^2}{2\Delta^2}\Big[\coth(\frac{1}{2}\beta\hbar\omega_{\mathrm{F}}) - 1\Big]k_{DA}^{nc}(\omega_{\mathrm{F}}) + \frac{\hbar^2 g_{\mathrm{F}}^2}{2\Delta^2}\Big[\coth(\frac{1}{2}\beta\hbar\omega_{\mathrm{F}}) + 1\Big]k_{DA}^{nc}(-\omega_{\mathrm{F}})\,, \quad (4.13)$$

where the frequency-shifted cavity-free rate constant is defined as:

$$k_{DA}^{nc}(\omega) = \frac{1}{\hbar^2}\int_{-\infty}^{\infty} \mathrm{d}t\, C_{\mathrm{FGR}}^{nc}(t)\, e^{i\omega t}\,. \quad (4.14)$$

The significant utility of Eq. 4.13 is that it allows for the calculation of the cavity-enhanced rate constant k_{DA} from the cavity-free rate constants $k_{DA}^{nc}, k_{DA}^{nc}(\pm\omega_{\mathrm{F}})$ (the latter can be calculated from the same correlation function). That is to say, if one obtains the cavity-free rates from the correlation functions, the cavity-enhanced rates can be evaluated with little additional effort.

For the model system at hand, the cavity-free correlation function $C_{\mathrm{FGR}}^{nc}(t)$ can be obtained in a similar fashion as the GOA model in chapter 2. The Hessian matrix of the nuclear DOFs is diagonalized to yield a Hamiltonian with a spin-boson form, and the correlation function is evaluated via Eq. 2.14.

Figure 4.1 shows the cavity-enhanced CT rate constants obtained via eq. 4.13, as a function of the donor-acceptor energy gap ε, for Model I (left) and Model II (right). With or without the cavity, the rate constants follow a roughly Marcus-like trend, where the rate increases with increasing ε in a normal region where the energy gap is small, reaches maximum CT rate at a inversion point, and decreases with increasing ε in the following inverted region. In Model I where the cavity frequency is low, the introduction of the cavity to the system results in an overall increase of the CT rates by a factor of 2, and does not lead to visible changes to the inversion point. In the high-frequency case of Model II, the enhancement of rates by the cavity clearly favors larger ε, and the inversion point is shifted to the right as a result.

The cavity-induced behavior shown in Fig. 4.1 can be understood by inspecting Eq. 2.14. Firstly, we notice that in this context of rate constant as a function of energy gap, the shifted cavity-free rate constant $k_{DA}^{nc}(\pm\omega_{\mathrm{F}})$ is equivalent to a cavity-free rate constant where the energy gap ε is replaced by $\varepsilon \pm \hbar\omega_{\mathrm{F}}$. Hence, the correction introduced by cavity $k_{DA} - k_{DA}^{nc}$ is a weighted sum of cavity-free rates where the energy gap is shifted to the left or to the right by $\hbar\omega_{\mathrm{F}}$. As a result, the low-frequency cavity of Model I (see table 4.1) can shift the inversion point by *at most* $10\ \mathrm{meV}$, which leads to an almost uniform enhancement of rates at all energy gap values.

Additionally, the weights for the two shifted cavity-free rate constant in Eq. 4.13 are biased towards the right-shifting case, since $\coth(\beta\hbar\omega_{\mathrm{F}}/2) + 1 > \coth(\beta\hbar\omega_{\mathrm{F}}/2) - 1$. This is most

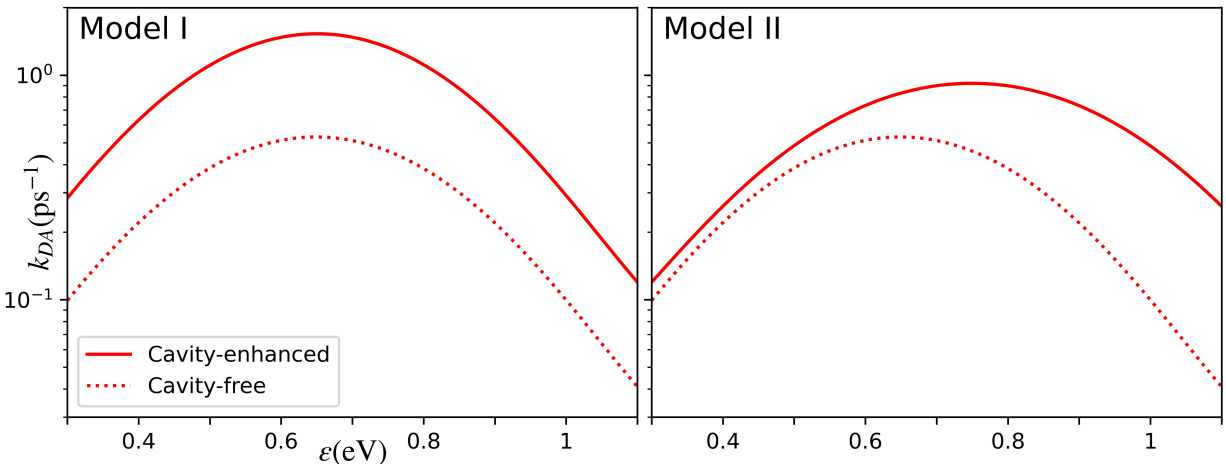


Figure 4.1: Cavity-enhanced Fermi's golden rule CT rate constants for (left) Model I and (right) Model II, compared to the cavity-free rates.

prominent in the high-frequency limit $\beta\hbar\omega_{\mathrm{F}} \gg 1$, where Eq. 4.13 becomes

$$k_{DA} = k_{DA}^{nc} + \frac{\hbar^2 g_{\mathrm{F}}^2}{\Delta^2} k_{DA}^{nc}(-\omega_{\mathrm{F}})\,, \tag{4.15}$$

where the cavity-induced enhancement scales with the right-shifted rate constant $k_{DA}^{nc}(-\omega_{\mathrm{F}})$. This is the case for Model II (see table 4.1) where $\coth(\beta\hbar\omega_{\mathrm{F}}/2) - 1 < 0.001$. As a result, the inverted region is selectively enhanced by the high-frequency cavity.

4.4 Concluding Remarks

The considerable and rapidly growing current interest in controlling molecular processes by coupling molecular matter to cavity modes[152–165] calls for accurate and scalable approximate methods for simulating the dynamics of chemical processes that take place in such systems.

In this chapter, it is shown the cavity-enhanced CT rate constant can be evaluated using the cavity-free rate constants with minimal additional effort. Importantly, no propagation of a system together with the cavity mode is necessary. This method is applied to a model system there the CT reaction is augmented by either a low-frequency or a high-frequency cavity mode. With in this context of FGR, where only the *transition dipole* between *two states* are considered, the introduction of the cavity always results in an enhancement of the FGR CT rate. While a low-frequency cavity leads to a almost uniform enhancement of rates at all energy gap values, a cavity with a higher frequency enhances the inverted region selectively. In order to account for a wider range of cavity-induced phenomenon such as selective suppression of reaction or biased enhancement

in the normal region, a more general picture that includes permanent dipole or non-constant electronic coupling for the cavity-free system has to be utilized. Work on such extensions is currently underway and will be presented in future publications.

CHAPTER 5

Computational Study of Charge-Transfer Dynamics in the Carotenoid–Porphyrin–C_{60} Molecular Triad Solvated in Explicit Tetrahydrofuran

This chapter is based on ref. 49, done in collaboration with Xiang Sun.

5.1 Introduction

The interplay between charge-transfer dynamics and molecular structure is key for processes that are fundamental to life, such as cellular respiration,[203] and photosynthesis,[204] as well as for processes that lie at the heart of important technologies, such as energy storage, photovoltaics, and thermoelectrics.[102,205–209] CT rates are often calculated by and rationalized within the framework of Marcus theory.[210–213] The popularity of Marcus theory can be attributed to the fact that the Marcus CT rate constant can be expressed in terms of three parameters—the electronic coupling coefficient, reorganization energy, and reaction free energy. As such it offers a straightforward pathway for fitting and interpreting experimentally measured CT rate constants. However, the restrictive nature of the assumptions underlying Marcus theory also makes it highly desirable to develop more comprehensive methods for calculating CT rates.[45] In particular, it is highly desirable to develop strategies for calculating CT rates for a system whose Hamiltonian is given in terms of anharmonic force fields in a direct manner and without resorting to mapping it onto an effective harmonic model Hamiltonian.[202,214–216]

One such general and direct approach starts out by applying the linearized semiclassical (LSC) approximation to the equilibrium FGR correlation function for the CT rate constant.[45,217] The classical-like nature of the LSC-based method implies that it can be applied to complex molecular systems governed by anharmonic force fields of one's choice. Additionally, the LSC-based expression for EFGR correlation function has been shown to reproduce the quantum-mechanically exact rate constant when the donor and acceptor potential energy surfaces (PESs) are parabolic and

identical except for shifts in equilibrium geometry and equilibrium energy. It was also shown in ref. 45 that a Marcus-like expression can be obtained from the LSC-based FGR expression, with the help of three major approximations: (1) assuming that the initial sampling of nuclear degrees of freedom (DOF) is based on the classical Boltzmann distribution, instead of the corresponding Wigner distribution called for by the LSC-based FGR expression; (2) assuming that the lifetime of the correlation function underlying FGR is shorter than the timescale of nuclear DOF motion; and (3) assuming that the cumulant expansion of the correlation function underlying FGR can be truncated at second order. The Marcus-like approximation that results from those three approximations is given in terms of the first and second moments of the donor–acceptor energy gap, which can be calculated in a straightforward manner from a classical equilibrium molecular dynamics (MD) simulation on the donor PES. Those first and second moments of the donor–acceptor energy gap can be related to the reaction free energy and reorganization energy of Marcus theory.

The LSC treatment utilized in this chapter closely follows ref. 45, which provides a comprehensive analysis of the above-mentioned LSC-based strategy, starting at the FGR level and going through the progression of approximations that lead to the Marcus-like level. While ref. 45 studied the case of a harmonic benchmark model where the quantum-mechanically exact FGR rate constant is known, in the current chapter, we showcase the main advantage of the LSC-based methodology: its applicability to molecular models, which would typically be governed by anharmonic force fields of one's choice.

In this chapter, we demonstrate this by applying the aforementioned strategy to a molecular model of the carotenoid–porphyrin–C60 triad in explicit tetrahydrofuran (THF) solvent.[218] It should be noted that CT rate constants for this system were previously calculated via another method at the Marcus level of theory.[218] It was also found in ref. 218 that CT dynamics in this system is strongly dependent on the conformation of the triad and is much faster in the linear conformation than in the more thermodynamically favorable bent conformation. In this paper, we go beyond that by testing the validity of the Marcus-like level of theory and showing that CT in this system is dominated by the DOF of the solvent (THF), rather than that of the solute (triad).

5.2 Theory

Consider the fully quantum-mechanical Hamiltonian operator of a two-state donor–acceptor system

$$\hat{H} = \hat{H}_D|D\rangle\langle D| + \hat{H}_A|A\rangle\langle A| + \Gamma_{DA}\big(|D\rangle\langle A| + |A\rangle\langle D|\big)\,. \tag{5.1}$$

Here, $|A\rangle(|D\rangle)$ represents the *diabatic* acceptor (donor) electronic state, $\hat{H}_A = \hat{\mathbf{P}}^2/2 + V_A(\hat{\mathbf{R}})$ and $\hat{H}_D = \hat{\mathbf{P}}^2/2 + V_D(\hat{\mathbf{R}})$ are the corresponding nuclear Hamiltonians, where $V_A(\hat{\mathbf{R}})$ and $V_D(\hat{\mathbf{R}})$

are the PESs, $\hat{\mathbf{R}} = (\hat{\mathbf{R}}_1, \cdots \hat{\mathbf{R}}_N)$ and $\hat{\mathbf{P}} = (\hat{\mathbf{P}}_1, \cdots \hat{\mathbf{P}}_N)$ are the mass-weighted coordinates and momenta of all nuclear DOFs (triad + solvent for the system under consideration in this paper), and Γ_{DA} is the electronic coupling coefficient. Importantly, $V_A(\hat{\mathbf{R}})$ and $V_D(\hat{\mathbf{R}})$ are assumed to be given in terms of anharmonic force fields.

Following Eq. 2.10 and chapter 4, the donor-to-acceptor FGR CT rate constant is given by

$$k_{DA} = \frac{1}{\hbar^2}\Gamma_{DA}^2 \int_{-\infty}^{\infty} \mathrm{d}\tau \, \mathrm{Tr}_N \left[\hat{\rho}_D^{eq} e^{\frac{i}{\hbar}\hat{H}_D \tau} e^{-\frac{i}{\hbar}\hat{H}_A \tau} \right] . \tag{5.2}$$

A fully quantum mechanical expression for k_{DA} can only be derived in closed form when the diabatic PESs are assumed to be harmonic (see appendix A). The LSC approximation for k_{DA} is obtained by rewriting the correlation function in terms of a (still quantum-mechanically exact) real-time Feynman path integral,[219–221] and expanding the forward–backward action to the first order with respect to the difference between the forward and backward trajectories.[217,222,223] The resulting LSC approximation for k_{DA} is given by

$$\begin{aligned} k_{DA}^{\mathrm{W-AV}} &= \frac{1}{\hbar^2}\Gamma_{DA}^2 \int_{-\infty}^{\infty} \mathrm{d}\tau \int \mathrm{d}\mathbf{R}_0 \int \mathrm{d}\mathbf{P}_0 \, \left[\hat{\rho}_D^{eq}\right]_{\mathrm{W}}(\mathbf{R}_0, \mathbf{P}_0) \exp\left(\frac{i}{\hbar}\int_0^{\tau} \mathrm{d}s \, U(\mathbf{R}_s)\right) \\ &= \frac{1}{\hbar^2}\Gamma_{DA}^2 \int_{-\infty}^{\infty} \mathrm{d}\tau \left\langle \exp\left(\frac{i}{\hbar}\int_0^{\tau} \mathrm{d}s \, U(\mathbf{R}_s)\right)\right\rangle_D^{\mathrm{W,eq}} . \end{aligned} \tag{5.3}$$

Here, $U(\mathbf{R}) = V_D(\mathbf{R}) - V_A(\mathbf{R})$ is the donor–acceptor energy gap, $\left[\hat{\rho}_D^{eq}\right]_{\mathrm{W}}(\mathbf{R}_0, \mathbf{P}_0)$ is the Wigner transform[224] of the donor thermal equilibrium state $\hat{\rho}_D^{eq}$, and $\mathbf{R}_s$ is obtained by classical dynamics, starting with $\{\mathbf{R}_0, \mathbf{P}_0\}$ as the initial conditions and propagating on the average PES, $V_{av} = [V_D + V_A]/2$. We label this approximation "W–AV" [Wigner (W) initial sampling with dynamics on average (AV) PES]. Despite its classical-like nature, the W–AV approximation yields the exact quantum mechanical equilibrium FGR CT rate constant when the donor and acceptor PESs are parabolic and identical except for a shift in the equilibrium energy and equilibrium geometry.[45]

The classical Marcus expression can be obtained from Eq. 5.3 by making a number of approximations. First, the Wignerized phase space density, $\left[\hat{\rho}_D^{eq}\right]_{\mathrm{W}}(\mathbf{R}_0, \mathbf{P}_0)$, needs to be replaced by the corresponding classical phase space density, $\rho_{D,\mathrm{Cl}}^{eq}(\mathbf{R}_0, \mathbf{P}_0)$,

$$\begin{aligned} k_{DA}^{\mathrm{C-AV}} &= \frac{1}{\hbar^2}\Gamma_{DA}^2 \int_{-\infty}^{\infty} \mathrm{d}\tau \int \mathrm{d}\mathbf{R}_0 \int \mathrm{d}\mathbf{P}_0 \, \rho_{D,\mathrm{Cl}}^{eq}(\mathbf{R}_0, \mathbf{P}_0) \exp\left(\frac{i}{\hbar}\int_0^{\tau} \mathrm{d}s \, U(\mathbf{R}_s)\right) \\ &= \frac{1}{\hbar^2}\Gamma_{DA}^2 \int_{-\infty}^{\infty} \mathrm{d}\tau \left\langle \exp\left(\frac{i}{\hbar}\int_0^{\tau} \mathrm{d}s \, U(\mathbf{R}_s)\right)\right\rangle_D^{\mathrm{Cl,eq}} . \end{aligned} \tag{5.4}$$

We label this approximation "C–AV" [classical (C) sampling with dynamics on average (AV) PES].

Second, one needs to assume that the correlation function decays faster than the nuclear dy-

namics timescale on which $U(\mathbf{R}_s)$ changes, which leads to the following approximation,

$$\begin{aligned} k_{DA}^{\mathrm{C}-0} &= \frac{1}{\hbar^2}\Gamma_{DA}^2 \int_{-\infty}^{\infty} \mathrm{d}\tau \int \mathrm{d}\mathbf{R}_0 \int \mathrm{d}\mathbf{P}_0 \, \rho_{D,\mathrm{Cl}}^{eq}(\mathbf{R}_0, \mathbf{P}_0) \exp\left(\frac{i}{\hbar} U(\mathbf{R}_0)\tau\right) \\ &= \frac{1}{\hbar^2}\Gamma_{DA}^2 \int_{-\infty}^{\infty} \mathrm{d}\tau \left\langle \exp\left(\frac{i}{\hbar} U(\mathbf{R}_0)\tau\right)\right\rangle_D^{\mathrm{Cl,eq}} \\ &= \frac{2\pi}{\hbar}\Gamma_{DA}^2 \big\langle \delta(U)\big\rangle_D^{\mathrm{Cl,eq}}, \end{aligned} \tag{5.5}$$

where $\delta(U)$ is the Dirac delta. We label this approximation "C–0" [classical (C) sampling and independent of which PES the dynamics takes place on (0)].

It should be noted that $k_{DA}^{\mathrm{C}-0}$ is proportional to the classical probability density of $U(\mathbf{R}_0)$ at $U = 0$. Since $|\langle U/\hbar\rangle_D^{\mathrm{Cl,eq}}|$ is typically significantly larger than zero, calculating $k_{DA}^{\mathrm{C}-0}$ requires being able to obtain an accurate estimate of the tail of the probability density. This becomes computationally more costly with increasing $|\langle U/\hbar\rangle_D^{\mathrm{Cl,eq}}|$ because more sampling will be required to obtain a converged result.

Alternatively, $U(\mathbf{R}_0)$ can be written as $U(\mathbf{R}_0) = \langle U\rangle_D^{\mathrm{Cl,eq}} + \delta U(\mathbf{R}_0)$, where $\delta U(\mathbf{R}_0) = U(\mathbf{R}_0) - \langle U\rangle_D^{\mathrm{Cl,eq}}$ is the fluctuation of $U(\mathbf{R}_0)$ relative to its equilibrium-averaged value ($\langle U\rangle_D^{\mathrm{Cl,eq}}$ is the equilibrium average of U on the donor PES). Substituting this decomposition into Eq. 5.5 yields

$$k_{DA}^{\mathrm{C}-0} = \frac{1}{\hbar^2}\Gamma_{DA}^2 \int_{-\infty}^{\infty} \mathrm{d}\tau \, \exp\left(\frac{i}{\hbar}\langle U\rangle_D^{\mathrm{Cl,eq}}\tau\right)\left\langle \exp\left(\frac{i}{\hbar}\delta U(\mathbf{R}_0)\tau\right)\right\rangle_D^{\mathrm{Cl,eq}}, \tag{5.6}$$

which translates calculating $k_{DA}^{\mathrm{C}-0}$ into evaluating the Fourier transform of $\langle \exp(i\delta U(\mathbf{R}_0)\tau/\hbar)\rangle_D^{\mathrm{Cl,eq}}$ at the frequency $\langle U\rangle_D^{\mathrm{Cl,eq}}/\hbar$. It should be noted that $\langle \exp(i\delta U(\mathbf{R}_0)\tau/\hbar)\rangle_D^{\mathrm{Cl,eq}}$ tends to be a smoothly decaying function compared to $\langle \exp(iU(\mathbf{R}_0)\tau/\hbar)\rangle_D^{\mathrm{Cl,eq}}$, which tends to be a rapidly oscillating function (when $|\delta U| \ll |\langle U\rangle|$). Hence, Eq. 5.6 allows one to efficiently calculate $k_{DA}^{\mathrm{C}-0}$ by using the fast Fourier transform (FFT) method.[225]

Obtaining the Marcus-like expression requires replacing $\langle \exp(i\delta U(\mathbf{R}_0)\tau/\hbar)\rangle_D^{\mathrm{Cl,eq}}$ in Eq. 5.6 by the corresponding second-order cumulant approximation, $\exp(-(\sigma_D^{\mathrm{Cl,eq}})^2\tau^2/2\hbar^2)$, where $(\sigma_D^{\mathrm{Cl,eq}})^2 = \langle U^2\rangle_D^{\mathrm{Cl,eq}} - (\langle U\rangle_D^{\mathrm{Cl,eq}})^2$ is the standard deviation of the donor–acceptor energy gap (at equilibrium on the donor PES). Approximating $\langle \exp(i\delta U(\mathbf{R}_0)\tau/\hbar)\rangle_D^{\mathrm{Cl,eq}}$ as a Gaussian function of time also implies that the probability density of U is assumed to be Gaussian (at least around $U = 0$). In this case, the Fourier transform in Eq. 5.6 can be evaluated analytically to yield:

$$k_{DA}^{\mathrm{M}} = \frac{1}{\hbar}\Gamma_{DA}^2 \sqrt{\frac{2\pi}{(\sigma_D^{\mathrm{Cl,eq}})^2}} \exp\left[-\frac{(\langle U\rangle_D^{\mathrm{Cl,eq}})^2}{2(\sigma_D^{\mathrm{Cl,eq}})^2}\right]. \tag{5.7}$$

It should be noted that Eq. 5.7 can be obtained from Eq. 5.5 by assuming that the probability

density of U is Gaussian: $\rho(U) \approx \exp[-(U - \langle U\rangle_D^{\mathrm{Cl,eq}})^2/2(\sigma_D^{\mathrm{Cl,eq}})^2]/\sqrt{2\pi(\sigma_D^{\mathrm{Cl,eq}})^2}$.

Equating the r.h.s. of Eq. 5.7 to the traditional Marcus expression

$$k_{DA}^{\mathrm{Marcus}} = \frac{1}{\hbar}\Gamma_{DA}^2\sqrt{\frac{\pi}{k_BTE_r}}\exp\left[-\frac{(\Delta E + E_r)^2}{4k_BTE_r}\right] \tag{5.8}$$

leads to the following expressions for the reorganization energy, reaction free energy, and activation energy in terms of $\langle U\rangle_D^{\mathrm{Cl,eq}}$ and $\sigma_D^{\mathrm{Cl,eq}}$:

$$\begin{aligned} E_r &= \frac{(\sigma_D^{\mathrm{Cl,eq}})^2}{2k_BT} \\ \Delta E &= -E_r - \langle U\rangle_D^{\mathrm{Cl,eq}} \\ E_A &= k_BT\frac{(\langle U\rangle_D^{\mathrm{Cl,eq}})^2}{2(\sigma_D^{\mathrm{Cl,eq}})^2}\ . \end{aligned} \tag{5.9}$$

It should be noted that the normal ($|\Delta E| < E_r$) and the inverted ($|\Delta E| > E_r$) Marcus regimes correspond to $\langle U\rangle_D^{\mathrm{Cl,eq}} < 0$ and $\langle U\rangle_D^{\mathrm{Cl,eq}} > 0$, respectively (see Figure 5.1).

One advantage of Eq. 5.7 over Eq. 5.8 is that the latter can be used without explicitly expressing the donor and acceptor PESs in this form. Furthermore, expressing the CT rate constant in terms of $\langle U\rangle_D^{\mathrm{Cl,eq}}$ and $\sigma_D^{\mathrm{Cl,eq}}$ is arguably more convenient because unlike E_r and ΔE, they are straightforward to obtain from an equilibrium MD simulation on the donor PES, when the latter is expressed in terms of anharmonic force fields of one's choice.

5.3 Molecular Model

We consider a triad consisting of covalently linked carotenoid polyene (C), diaryl porphyrin (P), and fullerene (C_{60}),[218,226–228] solvated in explicit THF solvent (see Figure 5.2). The molecular model, which is adopted from ref 218, includes four electronic states: (1) the ground state, CPC_{60}; (2) the P-localized photoexcited $\pi\pi^*$ state, CP^*C_{60}; (3) The excited P-to-C_{60} CT state, $CP^+C_{60}^-$, which we will refer to as CT1; and (4) the excited C-to-C_{60} charge-separated state, $C^+PC_{60}^-$, which we will refer to as CT2. Starting in the ground state, this system is believed to go through the following multistep process, which converts the light energy into electric energy (in the form of charge separation).[218]

$$[\mathrm{CPC_{60}}] \xrightarrow{h\nu} [\mathrm{CP^*C_{60}}] \rightarrow [\mathrm{CP^+C_{60}^-}] \rightarrow [\mathrm{C^+PC_{60}^-}]$$

The PESs that dictate the dynamics of the nuclear DOF (triad + solvent) differ from one electronic state to another and are given in terms of atom–atom pair potentials that include intermolec-

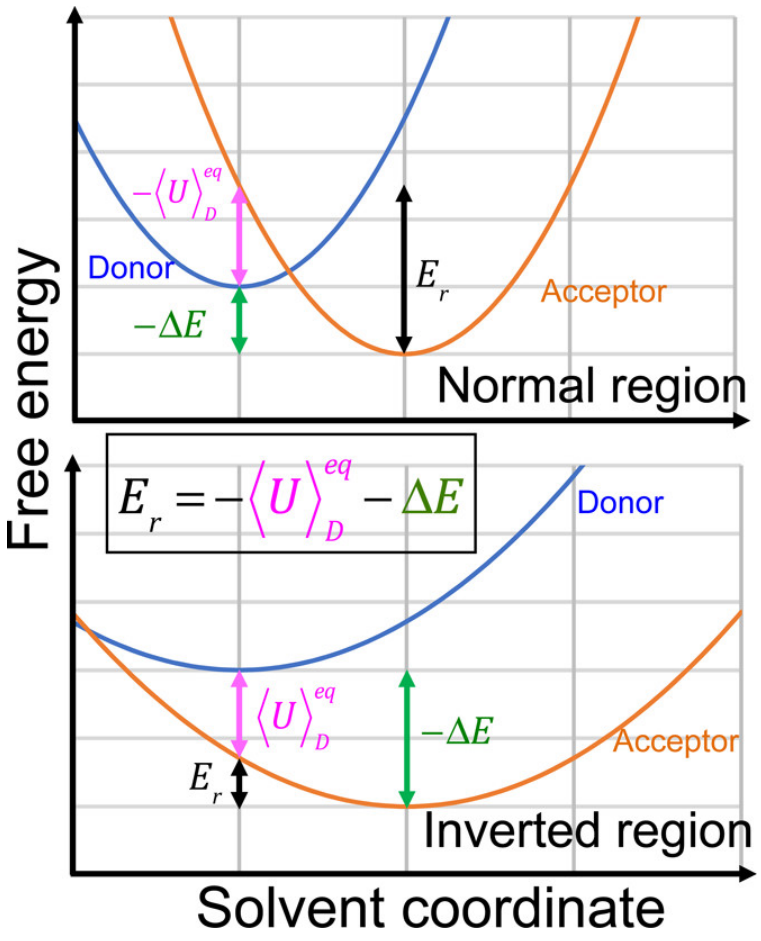


Figure 5.1: Schematic view of the relationship between the average donor–acceptor energy gap, $\langle U \rangle_D^{\mathrm{Cl,eq}}$, the reorganization energy, E_r, and the reaction free energy, ΔE, in the normal (upper panel) and inverted (lower panel) regions (see Eq. 5.9).

ular nonbonding Lennard-Jones and Coulomb interactions, as well as the usual intramolecular bonding interactions (bond length, bond angle, and dihedral angle). The force fields differ from one electronic state to another with respect to the Coulomb terms because the partial charges on the triad atoms differ from one electronic state to another. The model also includes electronic coupling coefficients between the excited electronic states (assumed constant within the Condon approximation and calculated via the fragment charge difference (FCD) method[229]). The partial atomic charges for THF were adopted from ref 230, where they were generated via AM1-BCC.[231] The electronic excitation energies, partial charges, and electronic coupling coefficients for the triad were adopted from ref 218, where they were obtained via time-dependent density functional theory (TD-DFT) using a range-separated hybrid (RSH) functional designed to yield accurate energetics for the CT states.

The rate constants between the initial donor (D) state and final acceptor (A) state, D→A, were

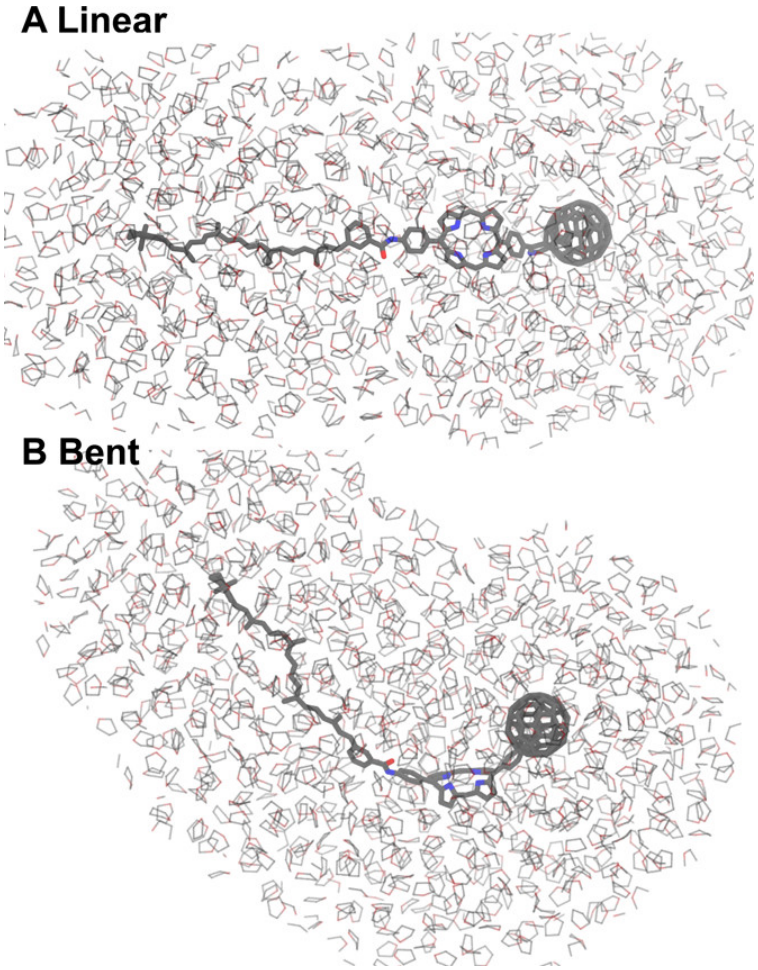


Figure 5.2: Molecular structure of the linear (A) and bent (B) conformations of the carotenoid–porphyrin–C_{60} molecular triad solvated in liquid THF. The triad is in ball-and-stick representation; the carbon, oxygen, and nitrogen atoms are in gray, red, and blue, respectively. For visibility, the hydrogen atoms are not shown and solvent THF molecules within 20 Å of the triad are shown. The figure was generated using Visual Molecular Dynamics (VMD) package.

calculated for the following choices of donor and acceptor states: $\pi\pi^*\rightarrow$CT1, $\pi\pi^*\rightarrow$CT2, and CT1$\rightarrow$CT2. To this end, we define $V_D(\mathbf{R},\mathbf{r})$ and $V_A(\mathbf{R},\mathbf{r})$ to be the PESs that correspond to the D and A states, respectively. Here, $\mathbf{R} = (\mathbf{R}_1, \cdots, \mathbf{R}_N)$ represents the coordinates of the N solvent atoms and $\mathbf{r} = (\mathbf{r}_1, \cdots, \mathbf{r}_N)$ represents the coordinates of the n triad atoms. Thus, the energy gap between the D and A states is given by $U(\mathbf{R},\mathbf{r}) = V_D(\mathbf{R},\mathbf{r}) - V_A(\mathbf{R},\mathbf{r})$.

The force fields used in the MD simulations are electronic-state-dependent and consist of contri-

butions from solvent–solvent (SS), triad–triad (TT), and solvent–triad (ST) potential energy terms:

$$
\begin{aligned}
V_{\alpha,SS}(\mathbf{R},\mathbf{r}) &= V_{SS}^{NE}(\mathbf{R}) + \sum_{J=1}^{N-1}\sum_{J'=J+1}^{N} \frac{1}{4\pi\varepsilon_0}\frac{Q_J Q_{J'}}{|\mathbf{R}_J - \mathbf{R}_{J'}|} \\
V_{\alpha,TT}(\mathbf{R},\mathbf{r}) &= V_{TT}^{NE}(\mathbf{r}) + \sum_{j=1}^{n-1}\sum_{j'=j+1}^{n} \frac{1}{4\pi\varepsilon_0}\frac{q_j^\alpha q_{j'}^\alpha}{|\mathbf{r}_j - \mathbf{r}_{j'}|} \\
V_{\alpha,ST}(\mathbf{R},\mathbf{r}) &= V_{ST}^{NE}(\mathbf{R},\mathbf{r}) + \sum_{J=1}^{N}\sum_{j=1}^{n} \frac{1}{4\pi\varepsilon_0}\frac{Q_J q_j^\alpha}{|\mathbf{R}_J - \mathbf{r}_j|} \,.
\end{aligned}
\tag{5.10}
$$

Here, $\alpha = \{\pi\pi^*, \text{CT1}, \text{CT2}\}$, $V_{SS}^{NE}(\mathbf{R})$, $V_{TT}^{NE}(\mathbf{r})$, and $V_{ST}^{NE}(\mathbf{R},\mathbf{r})$ include the nonelectrostatic bonding and nonbonding interactions (assumed to be independent of the triad's electronic state), $\{Q_J\}$ represents the partial charges assigned to the solvent atoms (assumed to be independent of the triad's electronic state), $\{q_j\}$ represents the partial charges assigned to the triad atoms (assumed to be dependent of the triad's electronic state).

Let the gas-phase energies of the ground, $\pi\pi^*$, CT1, and CT2 electronic states, at the ground-state equilibrium geometry, $\mathbf{r}^{G,eq}$, be given by E_G, $E_{\pi\pi*}$, E_{CT1}, and E_{CT2}, respectively. It should be noted that those energies already include the triad–triad interactions in the ground-state equilibrium geometry. Thus, we need to subtract that interaction energy to avoid double counting. It is also convenient to set the energy origin to E_G (so that $E_G \to 0$). The overall PES in different electronic states is therefore given by

$$
V_\alpha(\mathbf{R},\mathbf{r}) = E_\alpha - E_G - V_{\alpha,TT}(\mathbf{r}^{G,eq}) + V_{\alpha,SS}(\mathbf{R},\mathbf{r}) + V_{\alpha,TT}(\mathbf{R},\mathbf{r}) + V_{\alpha,ST}(\mathbf{R},\mathbf{r}) \,. \tag{5.11}
$$

It should be noted that for the force fields used here, $U(\mathbf{R},\mathbf{r})$ only depends on electrostatic interactions. This is because the nonelectrostatic components of $V_D(\mathbf{R},\mathbf{r})$ and $V_A(\mathbf{R},\mathbf{r})$ are identical and cancel out when one is subtracted from the other. It should also be noted that $V_D(\mathbf{R},\mathbf{r})$, $V_A(\mathbf{R},\mathbf{r})$, and $U(\mathbf{R},\mathbf{r})$ can be written as sums of an intramolecular (triad–triad) and an intermolecular (triad–solvent and solvent–solvent) contribution. Because the solvent–solvent contribution is the same for $V_D(\mathbf{R},\mathbf{r})$ and $V_A(\mathbf{R},\mathbf{r})$, the solvent–solvent contribution to $U(\mathbf{R},\mathbf{r})$ vanishes.

As shown in ref 218, the triad can exist in two different conformations—linear and bent (see Figure 5.2). Although the bent conformation was found to be thermodynamically more favorable, the rate of the CT process CT1→CT2 is found to be faster in the linear conformation.[218] Hence, the CT rate constants need to be calculated separately for each conformation.

5.4 MD Simulations

MD simulations were performed within AMBER14[232] using a 100 Å× 100 Å× 100 Åperiodic cubic simulation box containing one triad molecule and 6741 THF molecules, as described in refs 230 and 233. The general AMBER force field was employed,[234–236] with customized partial atomic charges as described above. After energy minimization using a steepest descent and conjugate gradient method, the system was gradually heated to $300\ \mathrm{K}$. During this process, the triad conformation was maintained by using a harmonic potential of force constant of $100\ \mathrm{kcal\ mol^{-1}\ \AA^{-2}}$ to constrain the distance between the two carbon atoms nearest to the two termini to its characteristic value in the corresponding conformation.

The SHAKE algorithm[237] was used to constrain the covalent bonds involving hydrogen atoms. The integration time step was $1.0\ \mathrm{fs}$. For equilibration, we employed Langevin dynamics with a collision frequency of $1.0\ \mathrm{ps^{-1}}$. A cutoff of 12 Åwas employed for the van der Waals interactions. Particle mesh Ewald summation was used to calculate the electrostatic interactions.[238] Next, we released the constraints on the triad molecule and equilibrated the system at $300\mathrm{K}$ in an NPT ensemble to reach a desired density of THF and an NVT ensemble for $100\ \mathrm{ps}$.

To investigate the impact of intermolecular versus intramolecular DOF on the CT rates, we repeated the calculations with a rigid triad molecule. All atoms of the triad molecule were subjected to a stiff restraint by applying a harmonic force with force constant of $100\ \mathrm{kcal\ mol^{-1}\ \AA^{-2}}$. In total, we performed four different simulations for each of the three CT processes ($\pi\pi$*→CT1, $\pi\pi$*→CT2, and CT1→CT2): (1) rigid triad in linear conformation; (2) rigid triad in bent conformation; (3) flexible triad in linear conformation; and (4) flexible triad in bent conformation. For each of the conditions, we adopted the following procedures. First, starting with a ground-state equilibrium configuration, we carried out MD simulations on the initial excited-state PES, for $2.0\,\mathrm{ns}$, in the NVT ensemble, to reach equilibrium on the initial excited-state PES. Second, we performed an $8.0\ \mathrm{ns}$ long production simulation, where we recorded the donor–acceptor energy gap, $U(\mathbf{R}, \mathbf{r})$, along the trajectories at $5\ \mathrm{fs}$ intervals. Error bars were calculated by splitting the $8.0\ \mathrm{ns}$ long production trajectory into four $2.0\ \mathrm{ns}$ long segments, calculating the rate constants separately for each segment, and equating the error bar to the corresponding standard deviation (uncorrected for sample size).

5.5 Results

The $\pi\pi$*→CT1, $\pi\pi$*→CT2, and CT1→CT2 rate constants, calculated via Eqs. 5.6 and 5.7, in the bent and linear conformations, are presented in Tables 5.1 and 5.2, respectively. Results are shown for the flexible and rigid triad cases. It should be noted that we were unable to obtain a converged

	bent/flexible		bent/rigid	
	k_{DA}^{M} (s^{-1})	$k_{DA}^{\mathrm{C-0}}$ (s^{-1})	k_{DA}^{M} (s^{-1})	$k_{DA}^{\mathrm{C-0}}$ (s^{-1})
$\pi\pi^*\rightarrow$CT1	$(3.0 \pm 0.2) \times 10^{11}$	$(2.9 \pm 0.2) \times 10^{11}$	$(3.6 \pm 0.7) \times 10^{11}$	$(3.9 \pm 0.6) \times 10^{11}$
$\pi\pi^*\rightarrow$CT2	$(8.0 \pm 2.0) \times 10^{6}$	$(8.0 \pm 2.0) \times 10^{6}$	$(9.2 \pm 0.2) \times 10^{6}$	$(9.7 \pm 0.4) \times 10^{6}$
CT1$\rightarrow$CT2	$(2.3 \pm 0.6) \times 10^{2}$	$(2.2 \pm 0.2) \times 10^{2}$	$(3.2 \pm 0.6) \times 10^{2}$	

Table 5.1: Donor-to-Acceptor rate constants for the triad in the bent conformation

value of $k_{DA}^{\mathrm{C-0}}$ for CT1$\rightarrow$CT2 in the bent/rigid case, which is attributed to the exceedingly small value of the Fourier transform in this case (see eq 5.6).

The results in Tables 5.1 and 5.2 follow the same trends reported in ref 218. More specifically, photoinduced CT in this system is observed to occur through a two-step process: $\pi\pi^*\rightarrow$CT1$\rightarrow$CT2, rather than through a direct one-step process, $\pi\pi^*\rightarrow$CT2. This is because the first step, $\pi\pi^*\rightarrow$CT1, is much faster than the direct one-step process, $\pi\pi^*\rightarrow$CT2. Furthermore, the rate of the second step, CT1$\rightarrow$CT2, is observed to be faster in the linear conformation, by a factor of $10^6 - 10^7$, than in the bent conformation. This implies that although the bent conformation is thermodynamically more favorable than the linear conformation, the CT1$\rightarrow$CT2 process is far more likely to occur in the linear conformation. On the basis of those observations, the bent-to-linear conformational reaction is the rate-determining step for CT in this system. This observation highlights the potentially strong correlation between the molecular structure and CT dynamics and thereby the possibility of controlling the latter by modifying the former. It should be noted that, similar to the rate constants reported in ref 218, the rate constants in Tables 5.1 and 5.2 are also in reasonable agreement with the reported experimental estimates for the $\pi\pi^*\rightarrow$CT1 rate constant, $3.3 \times 10^{11}\ \mathrm{s}^{-1}$, and CT1$\rightarrow$CT2 rate constant, $1.5 \times 10^{10}\ \mathrm{s}^{-1}$.[239]

With one exception (CT1$\rightarrow$CT2 in bent/flexible case), the k_{DA}^{M} values for the bent/flexible and linear/flexible cases were found to agree rather well with the corresponding values reported in ref 218. It should be noted that the values of k_{DA} reported in ref 218 were obtained by using the

	linear/flexible		linear/rigid	
	k_{DA}^{M} (s^{-1})	$k_{DA}^{\mathrm{C-0}}$ (s^{-1})	k_{DA}^{M} (s^{-1})	$k_{DA}^{\mathrm{C-0}}$ (s^{-1})
$\pi\pi^*\rightarrow$CT1	$(1.12 \pm 0.04) \times 10^{12}$	$(1.17 \pm 0.04) \times 10^{12}$	$(1.1 \pm 0.1) \times 10^{12}$	$(1.0 \pm 0.1) \times 10^{12}$
$\pi\pi^*\rightarrow$CT2	$(1.9 \pm 0.2) \times 10^{8}$	$(1.86 \pm 0.02) \times 10^{8}$	$(1.90 \pm 0.04) \times 10^{8}$	$(2.0 \pm 0.1) \times 10^{8}$
CT1$\rightarrow$CT2	$(1.0 \pm 0.2) \times 10^{9}$	$(1.1 \pm 0.3) \times 10^{9}$	$(5.8 \pm 0.9) \times 10^{8}$	$(6.0 \pm 1.0) \times 10^{8}$

Table 5.2: Donor-to-Acceptor rate constants for the triad in the linear conformation

standard Marcus expression, Eq. 5.8, with ΔE and E_r given by[203,240,241]

$$\begin{aligned} \Delta E &= \frac{1}{2}\left[\langle V_A - V_D\rangle_D^{\mathrm{Cl,eq}} + \langle V_A - V_D\rangle_A^{\mathrm{Cl,eq}}\right] \\ E_r &= \frac{1}{2}\left[\langle V_A - V_D\rangle_D^{\mathrm{Cl,eq}} - \langle V_A - V_D\rangle_A^{\mathrm{Cl,eq}}\right] . \end{aligned} \tag{5.12}$$

It can be shown that the expressions for ΔE and E_r in Eq. 5.12 would give the same values as the expressions in Eq. 5.9 in the case where the donor and acceptor PESs are given in terms of identical parabolas which are shifted with respect to their equilibrium geometry and equilibrium energy. However, it should also be noted that Eqs. 5.12 and 5.9 need not agree when one deviates from the shifted identical parabolas model. Thus, the agreement between the predictions obtained via Eqs. 5.12 and 5.9 provides further support to the self-consistency of the linear-response-based picture based on which the donor and acceptor PESs can be mapped onto shifted, but otherwise identical, effective parabolas[202,214–216] (although in practice one obviously does not need to explicitly cast the Hamiltonian in this form).

The one exception is observed for the CT1→CT2 rate constant in the bent/flexible case. In this case, our prediction, $k_{DA}^{\mathrm{M}} = (2.3 \pm 0.6) \times 10^2\ \mathrm{s}^{-1}$, is significantly smaller than that reported in ref 218, $k_{DA} = 6.6 \times 10^3\ \mathrm{s}^{-1}$. The difference may be either due to deviations from the shifted but otherwise identical parabola picture or the fact that this rate constant is particularly small and thereby more difficult to converge (no error bars were reported in ref 218).

We next consider the validity of the second-order cumulant approximation by comparing the values of k_{DA}^{M} and $k_{DA}^{\mathrm{C}-0}$. Within error bars, k_{DA}^{M} and $k_{DA}^{\mathrm{C}-0}$ are observed to have the same value in all cases. Furthermore, comparison of the probability densities of the donor–acceptor energy gaps, U, with the corresponding Gaussian approximations reveals excellent agreement across the entire range of U values and not just at the vicinity of $U = 0$ (see Figures 5.3 and 5.4). These observations serve as strong validation of the accuracy of the second-order cumulant approximation for this system and the Marcus-like expression for the rate constant derived based on it (see Eq. 5.7). It should be noted that the ability of the second-order cumulant approximation to produce predictions that are quantitatively indistinguishable from those obtained without making this approximation is not self-evident for a molecular system of the level of complexity of the triad + solvent. Furthermore, the fact that the Marcus-like expression in Eq. 5.7 is consistent with experiment cannot be taken as proof for the validity of the second-order cumulant approximation. However, comparing the effect on the CT rate constants of removing this approximation, as we have done here, can provide such a proof. Thus, following the procedure outlined here provides a practical way of testing the assumptions underlying Marcus theory and avoiding them when they are observed not to be valid.[242]

The validity of the second-order cumulant approximation suggests that the rate constants can be

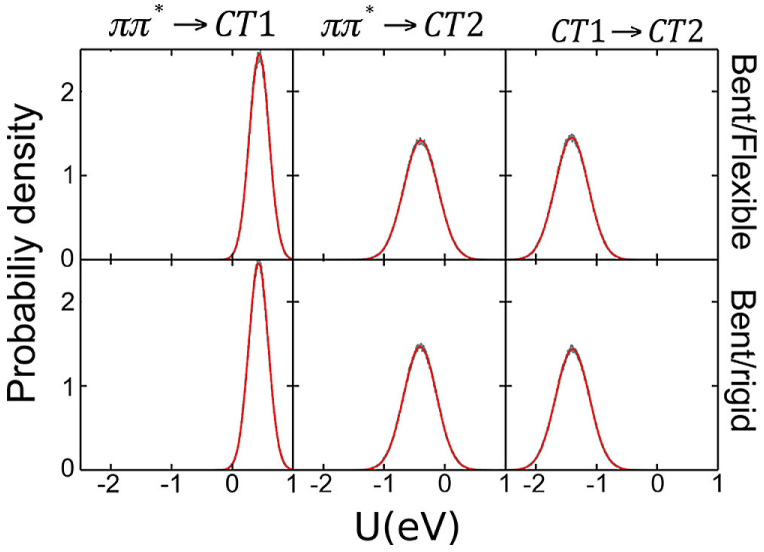


Figure 5.3: Comparison between the probability densities (black) of the donor–acceptor energy gaps, U, and the corresponding Gaussian approximations (red), for the flexible (upper panels) and rigid (lower panels) bent conformation.

rationalized within the framework of Marcus theory. To this end, we calculated the reorganization energies, reaction free energies, and activation energies from the first and second moments of the donor–acceptor energy gap, Eq. 5.9 (see Tables 5.3-5.6). It should be noted that with the exception of $\pi\pi$*→CT1 in the bent conformation, all cases correspond to the Marcus normal regime ($|\Delta E| < E_r$). The fact that $\pi\pi$*→CT1 in the bent conformation correspond to the inverted regime is also manifested by the fact that this is the only case where $\langle U \rangle_D^{\mathrm{Cl,eq}}$ is positive (see comment below Eq. 5.9).

Both $\pi\pi$*→CT1 and $\pi\pi$*→CT2 are seen to have relatively small activation energies. The activation energy for $\pi\pi$*→CT2 is seen to be larger/smaller than that for $\pi\pi$*→CT1 in the linear/bent conformations. Thus, the fact that $\pi\pi$*→CT1 is much faster than $\pi\pi$*→CT2 in both conformations is mostly due to the larger electronic coupling.

The much faster rate of CT1→CT2 in the linear conformation compared to the bent conforma-

	Γ_{DA}^2 (eV^2)	$\langle U \rangle_D^{\mathrm{Cl,eq}}$ (eV)	$(\sigma_D^{\mathrm{Cl,eq}})^2$ (eV^2)	E_r (eV)	ΔE (eV)	E_A (eV)
$\pi\pi$*→CT1	5.8×10^{-4}	0.444	0.027	0.515	−0.959	0.096
$\pi\pi$*→CT2	2.0×10^{-9}	−0.394	0.079	1.531	−1.137	0.025
CT1→CT2	7.4×10^{-9}	−1.410	0.076	1.460	−0.050	0.340

Table 5.3: Squared electronic coupling coefficients (Γ_{DA}^2), average ($\langle U \rangle_D^{\mathrm{Cl,eq}}$) and variance ($(\sigma_D^{\mathrm{Cl,eq}})^2$ (eV^2)) of Donor-Acceptor energy gap, reorganization energy (E_r), reaction free energy (ΔE), and activation energy (E_A) for a flexible triad in the bent conformation

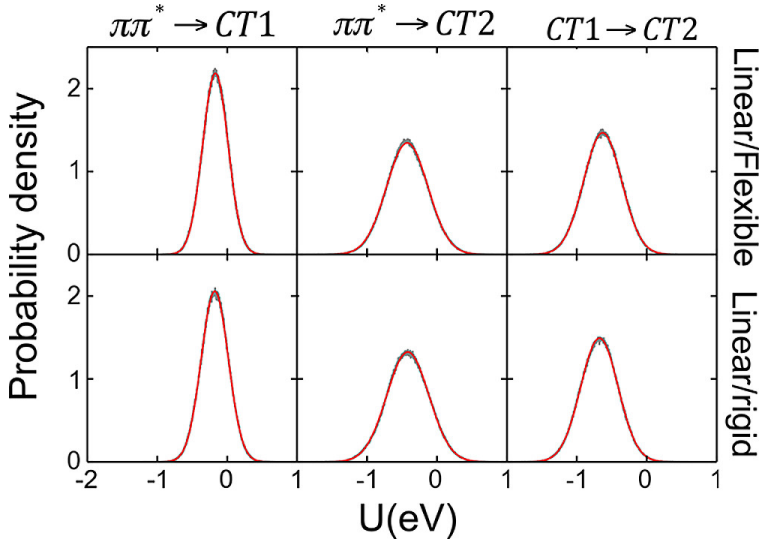


Figure 5.4: Comparison between the probability densities (black) of the donor–acceptor energy gaps, U, and the corresponding Gaussian approximations (red), for the flexible (upper panels) and rigid (lower panels) linear conformation.

tion can also be traced back to both effects (the activation energy in the linear conformation is lower by a factor of 5 and the squared electronic coupling coefficient in the linear conformation is larger by a factor of 135). However, the fact that the CT1→CT2 rate constant in the linear conformation is larger by a factor of $10^6 - 10^7$ suggests that lowering the activation barrier plays the decisive role in this case. Because the reorganization energies for CT1→CT2 in the bent and linear conformations are similar, the lowered activation energy in the linear conformation can be traced back to the corresponding more negative value of ΔE. Alternatively, the same effect can also be rationalized by noting that while the width of the U distribution, $\sigma_D^{\mathrm{Cl,eq}}$, is similar for both conformations, the average of U squared, $(\langle U\rangle_D^{\mathrm{Cl,eq}})^2$, is larger by a factor of 5 in the bent conformation.

The values of $(\sigma_D^{\mathrm{Cl,eq}})^2$ in Tables 5.3-5.6 can also be used to test the validity of the assumption that $\langle \exp(\frac{i}{\hbar}\int_0^\tau \mathrm{d}s\, \delta U(\mathbf{R}_s))\rangle_D^{\mathrm{Cl,eq}}$ decays faster than the nuclear dynamics timescale on which $U(\mathbf{R}_s))$ changes, which was employed to obtain Eq. 5.5 from 5.4. To this end, we

	Γ_{DA}^2 (eV^2)	$\langle U\rangle_D^{\mathrm{Cl,eq}}$ (eV)	$(\sigma_D^{\mathrm{Cl,eq}})^2$ (eV^2)	E_r (eV)	ΔE (eV)	E_A (eV)
ππ*→CT1	5.8×10^{-4}	0.432	0.026	0.511	−0.943	0.091
ππ*→CT2	2.0×10^{-9}	−0.406	0.074	1.431	−1.025	0.026
CT1→CT2	7.4×10^{-9}	−1.397	0.077	1.493	−0.096	0.327

Table 5.4: Squared electronic coupling coefficients (Γ_{DA}^2), average ($\langle U\rangle_D^{\mathrm{Cl,eq}}$) and variance ($(\sigma_D^{\mathrm{Cl,eq}})^2$ (eV^2)) of Donor-Acceptor energy gap, reorganization energy (E_r), reaction free energy (ΔE), and activation energy (E_A) for a rigid triad in the bent conformation

	Γ_{DA}^2 (eV^2)	$\langle U\rangle_D^{\mathrm{Cl,eq}}$ (eV)	$(\sigma_D^{\mathrm{Cl,eq}})^2$ (eV^2)	E_r (eV)	ΔE (eV)	E_A (eV)
$\pi\pi^*\rightarrow$CT1	8.1×10^{-5}	-0.169	0.033	0.645	-0.477	0.011
$\pi\pi^*\rightarrow$CT2	4.0×10^{-8}	-0.425	0.088	1.703	-1.278	0.026
CT1$\rightarrow$CT2	1.0×10^{-6}	-0.631	0.074	1.431	-0.799	0.070

Table 5.5: Squared electronic coupling coefficients (Γ_{DA}^2), average ($\langle U\rangle_D^{\mathrm{Cl,eq}}$) and variance ($(\sigma_D^{\mathrm{Cl,eq}})^2$ (eV^2)) of Donor-Acceptor energy gap, reorganization energy (E_r), reaction free energy (ΔE), and activation energy (E_A) for a flexible triad in the linear conformation

note that $\langle\exp(\frac{i}{\hbar}\delta U(\mathbf{R}_0))\tau\rangle_D^{\mathrm{Cl,eq}} \approx \exp(-\frac{1}{2\hbar^2}(\sigma_D^{\mathrm{Cl,eq}})^2\tau^2))$. Thus, the timescale of the decay of $\langle\exp(\frac{i}{\hbar}\delta U(\mathbf{R}_0))\tau\rangle_D^{\mathrm{Cl,eq}}$ can be estimated by $\sqrt{2}\hbar/\sigma_D^{\mathrm{Cl,eq}}$. For the system under consideration here, those timescales are in the range of $(3-6)$ fs, which are indeed faster than the nuclear dynamics timescale.

Another interesting comparison is between the values of k_{DA}^{M} and $k_{DA}^{\mathrm{C}-0}$ obtained in the rigid and flexible cases. The results in Tables 5.1 and 5.2 show that freezing the triad's intramolecular DOF either has no effect (linear conformation) or a rather minor effect (bent conformation) on the values of k_{DA}^{M} and $k_{DA}^{\mathrm{C}-0}$. This suggests that CT in this system is driven by the intermolecular (solvent) DOF, rather than by the intramolecular (triad) DOF. Here too, it is not self-evident that this would be the case, in light of the triad's size and flexibility.

It should be noted that strictly speaking, treating the intramolecular vibrations as classical is an approximation, which may break down in the case of high frequency modes, particularly in the inverted region. However, as pointed up above, the only case that corresponds to the inverted region is $\pi\pi^*\rightarrow$CT1 in the bent conformation. Thus, even if the $\pi\pi^*\rightarrow$CT1 rate could have been made faster by accounting for the quantum nature of intramolecular vibrations, our conclusions would still hold. This is because the CT1$\rightarrow$CT2 rate in the bent conformation is significantly slower than that in the linear conformation. It should also be noted that the triad molecule is rather large and flexible. Thus, intramolecular reorganization is expected to be dominated by collective low-frequency modes for which one expect the classical treatment to be a reasonable approximation.

	Γ_{DA}^2 (eV^2)	$\langle U\rangle_D^{\mathrm{Cl,eq}}$ (eV)	$(\sigma_D^{\mathrm{Cl,eq}})^2$ (eV^2)	E_r (eV)	ΔE (eV)	E_A (eV)
$\pi\pi^*\rightarrow$CT1	8.1×10^{-5}	-0.177	0.038	0.728	-0.551	0.011
$\pi\pi^*\rightarrow$CT2	4.0×10^{-8}	-0.417	0.091	1.757	-1.340	0.025
CT1$\rightarrow$CT2	1.0×10^{-6}	-0.677	0.072	1.385	-0.708	0.083

Table 5.6: Squared electronic coupling coefficients (Γ_{DA}^2), average ($\langle U\rangle_D^{\mathrm{Cl,eq}}$) and variance ($(\sigma_D^{\mathrm{Cl,eq}})^2$ (eV^2)) of Donor-Acceptor energy gap, reorganization energy (E_r), reaction free energy (ΔE), and activation energy (E_A) for a rigid triad in the linear conformation

5.6 Concluding Remarks

In this chapter, we demonstrate the applicability of a LSC-based methodology for calculating EFGR CT rate constants in complex molecular systems described by general anharmonic force fields on a molecular model of the carotenoid–porphyrin–C_{60} triad solvated in a THF explicit liquid solvent. Starting with the LSC approximation of the equilibrium FGR expression for the CT rate constant, we derived a hierarchy of progressively more approximate expressions for the CT rate constant. The classical-like nature of the LSC-based FGR expression and approximations derived from it implies that they can be applied to complex molecular systems governed by anharmonic force fields of one's choice. As a result, it becomes possible to test the validity of the various approximations by comparing the CT rate constants obtained with and without them.

Here, we used this methodology to test the validity of the second-order cumulant approximation, which leads to a Marcus-like expression for the CT rate constant. We did so by calculating the CT rate constants between the three excited states of the triad ($\pi\pi$*, CT1, CT2) in its two conformations (bent and linear) with and without making the second-order cumulant approximation. The comparison confirmed that the second-order cumulant approximation is quantitatively accurate. The Marcus-like expression based on the second-order cumulant approximation was also found to be in agreement with previously reported Marcus theory rate constants[218] obtained for this system via a different scheme.[203,240,241] We also confirmed the strong dependence of CT dynamics on the triad's conformation reported in ref 218, which suggests that the bent→linear conformational reaction is the rate-determining step for CT in this system.

One of the advantages of being able to calculate CT rate constants within the framework of a molecular model is that it makes it possible to address questions of a truly molecular nature in a direct manner. This was demonstrated here by investigating the roles of intra-molecular versus inter-molecular DOF on the CT rate constant. We did so by comparing the calculated CT rate constants obtained with a flexible triad molecule to those obtained with a rigid triad molecule. The results of this comparison showed that CT in this system is driven by the inter-molecular (solvent) DOF, rather than by the intra-molecular (triad) DOF. This highlights the potentially important impact that interactions with the host can have on CT rates and thereby of the importance of calculating CT rates based on molecular models that include an explicit host as well as an accurate description of its interactions with the solute.

CHAPTER 6

Conclusion

6.1 Summary

Projection-based methods provide a general framework for formulating reduced electronically nonadiabatic dynamics. The QMEs studied in this thesis are based on a second-order perturbative approach to the projection-based dynamics. Under certain approximations, those QMEs reduce into various well-known dynamical theories, such as Redfield theory, modified Redfield theory, FGR, and Marcus theory. Within such perturbative QMEs all information regarding the bath DOF is encapsulated in memory kernels, which are given in terms of bath-only correlation functions (Eqs. 2.3a-2.3d and 2.7a-2.7c).

In the current dissertation, we focus on OD-QME which, unlike Redfield-like QME, has the ability of treating different parts of the Hamiltonian perturbatively by changing the electronic basis. However, this comes with the limitation of having to work in the interaction picture, the transformation to or from which is nontrivial, and alters the electronic coherences (the off diagonal elements of the electronic density operator). As a result, previous applications of OD-QME based methods were limited to population dynamics, which made the simulation of electronic spectra, or the electronic dynamics in different electronic basis in general, challenging. We overcame this limitation by employing a recently proposed projection-based technique that can take any interaction picture reduced dynamical inputs and yield the corresponding Schrödinger picture reduced density operator. In chapters 2 and 3, OD-QME and the technique to retrieve Schrödinger picture dynamics are applied to the simulation of reduced electronic dynamics and absorption spectroscopy, respectively, and the results are compared to numerically exact methods. For the model systems studied, the bath-only correlation functions, and thereby the memory kernels, are available analytically. It is found that OD-QMEs can be very accurate across a relatively wide parameter range. Especially, the results show that TNL OD-QME is consistently more accurate then TL OD-QME, especially when the population-only projection is used. This discrepancy is traced back to increasing memory times as a result of decreasing temperature or decreasing friction. Due to the fact that

the Schrödinger picture reduced dynamics is retrieved using a *first-order* perturbative technique, the accuracy of coherence by OD-QME is more sensitive to increasing perturbative parameter than population.

In chapters 4 and 5, we shift our attention to FGR, which is the Markovian limit of p-TL-OD-FGR and the historically most utilized variation of OD-QME. Chapter 4 studies the FGR rates of electronically nonadiabatic reactions enhanced by a microcavity. It is shown that the cavity-enhanced reaction rates can be evaluated from the cavity-free FGR correlation function with minimum additional effort. In particular, no additional propagation of a system together with the cavity mode is necessary. This method is applied to a model CT reaction, where it is shown that while a high-frequency cavity enhances reactions in the Marcus inverted region selectively, a low-frequency enhances reactions in all regions uniformly.

Chapter 5 reports a the calculation of FGR CT rate constants for a molecular triad system solvated in explicit solvent, without explicit mapping to a harmonic PES. To evaluate the bath correlation functions for such a anharmonic Hamiltonian, we apply a LSC-based methodology which, after applying a hierarchy of approximations, becomes a Marcus-like expression, such that the rate can be extracted from the equilibrium distribution of the donor-acceptor energy gap. The validity of the approximation leading to Marcus-like expression is tested by comparing the energy gap distribution to a Gaussian distribution. The rate constants calculated for the molecular triad is in good agreement with experimental values and previously reported Marcus theory values. The rates are shown to be deeply dependent on the conformation (bent/linear) of the triad molecule, and the bent-linear conformational reaction is the rate-determining step for CT in this system.

6.2 Outlook

The OD-QMEs under consideration in this dissertation are all given in terms of the diabatic local exciton basis. However, the formulation of OD-QMEs puts no restriction on the electronic basis being used. An obvious extension is to instead use the electronic eigen (i.e. delocalized exciton in some context) basis, which would treat the off-diagonal part of system-bath coupling as the perturbation. The TL variation of such OD-QME is more commonly known as the modified Redfield theory. By combining modified Redfield theory and the projection-based technique to recover the Schrödinger picture coherences, it may be possible to simulate electronic dynamics and spectra in the case of strong electronic coupling. More generally, the transformation to different electronic basis is equivalent to a rotation in the electronic Hilbert space, and can be described by continuous parameters instead of a discrete choice between diabatic or eigenbasis. The continuous rotation can be utilized to minimize the off-diagonal Hamiltonian, which can result in an enhancement of accuracy for OD-QME as a perturbative method.

Another possible extension is to the simulation of spectroscopy. Specifically, the application of OD-QMEs for calculating time resolved multidimensional non-linear spectra, where the material system interacts with multiple pulses before measurement. The challenge of simulating non-linear spectra lies in the fact that the material system interacts with the field between the initial pulse and the measurement, resulting in a time-dependent Hamiltonian. A straightforward approach that sees some application to Redfield QME is to treat the OD-QME as a generic propagator in Liouville space, and use it to simulate field-free dynamics in between pulses. This approach is however not rigorous, since OD-QME requires the initial overall state to be separable, and the initial bath state is required to construct the memory kernel. Neither of these assumptions are true after the second pulse. We intend to device a more general and rigorous approach which will be based on re-deriving OD-QME in the context of a time-dependent interaction Hamiltonian. The fact that field-matter interaction comes in short pulses may be utilized to simplify the resulting EOM significantly.

The application of OD-QME to cavity-modified charge transfer leaves many questions unanswered. Our current model describes only cavity-induced *enhancement* of the charge transfer process that always favors the inverted region. This contradicts with experimental results where cavity may also leads to *suppression* of reactions under some conditions. One possible way to reproduce the cavity-induced suppression is to explicitly include the permanent dipoles as well as the so-called dipole self energy term in the field Hamiltonian. These complications will lead to a different rate equation, but the most important characteristic can be kept unaffected: the cavity-modified rate can still be obtained from only the cavity-free correlation functions, without performing simulations of a compound material-field model. Another important generalization to be made is the inclusion of multiple photonic modes. This will be used to include higher harmonic modes other than the fundamental mode, which is especially important for low-frequency cavities.

The last extension to be covered here corresponds to the application of LSC. The current dissertation demonstrates the evaluation of FGR rate constants for a molecular system via LSC. This methodology can be extended to p-TNL-OD-QME and f-OD-QME, since LSC is capable of calculating generic bath correlation functions, allowing the applicability of OD-QME to extend to electronic nonadiabatic dynamics of complex molecular systems.

APPENDIX A

Evaluation of the bath correlation functions for the spin-boson model

In this appendix, we outline the derivation of the closed form expressions for $\langle \hat{V}_{jk}(t) \rangle$, $\langle \hat{V}_{ij}(t)\hat{V}_{kl}(\tau) \rangle$, $\langle \hat{S}_{jk}(t) \rangle$, and $\langle \hat{S}_{ij}(t)\hat{V}_{kl}(\tau) \rangle$ for a system governed by the GOA model Hamiltonian, Eq. (2.13), that starts at the initial state $\hat{\rho}(0) = \hat{\rho}_N(0) \otimes |D\rangle\langle D|$, where $\hat{\rho}_N(0) = e^{-\beta \hat{H}_D} / \operatorname{Tr}_B[e^{-\beta \hat{H}_D}]$ (see Eq. 2.14).

To this end, we note that $\hat{H}_D$, $\hat{H}_A$ and $\hat{\rho}_B(0)$ can be written in terms of single mode terms:

$$\begin{aligned} \hat{H}_D &= \sum_{n=1}^{N} \frac{P_n^2}{2} + \frac{1}{2} \sum_{n=1}^{N} \omega_n^2 R_n^2 + \hbar \omega_{DA} \\ &\equiv \sum_{n=1}^{N} \hat{H}_D^n + \hbar \omega_{DA} \end{aligned} \tag{A.1}$$

$$\begin{aligned} \hat{H}_A &= \sum_{n=1}^{N} \frac{P_n^2}{2} + \frac{1}{2} \sum_{n=1}^{N} \omega_n^2 \left(R_n - R_n^{eq}\right)^2 \\ &\equiv \sum_{n=1}^{N} \hat{H}_A^n \end{aligned} \tag{A.2}$$

$$\begin{aligned} \hat{\rho}_B(0) &= \frac{1}{Z_D} \exp\left\{ -\beta \left[\sum_{n=1}^{N} \frac{P_n^2}{2} + \frac{1}{2} \sum_{n=1}^{N} \omega_n^2 R_n^2 \right] \right\} \\ &= \prod_{n=1}^{N} \frac{1}{Z_n} \exp\left\{ -\beta \left[\frac{P_n^2}{2} + \frac{1}{2} \omega_n^2 R_n^2 \right] \right\} \\ &\equiv \prod_{n=1}^{N} \hat{\rho}_n(0) \end{aligned} \tag{A.3}$$

Here, the tilde indicating normal mode frequencies were dropped for simplicity and $Z_n =$

$[2\tanh(\beta\hbar\omega_n/2)\sinh(\beta\hbar\omega_n)]^{-1/2}$.

As a result, $\langle\hat{V}_{ij}(t)\hat{V}_{kl}(\tau)\rangle$ can also be cast as a product of single-mode terms:

$$\begin{aligned}\langle\hat{V}_{ij}(t)\hat{V}_{kl}(\tau)\rangle &= \Gamma^2 e^{i\omega_{ij}t}e^{i\omega_{kl}\tau} \\ &\quad\times\prod_{n=1}^{N}\mathrm{Tr}_n\big[\hat{\rho}_n(0)e^{\frac{i}{\hbar}\hat{H}_i^n t}e^{-\frac{i}{\hbar}\hat{H}_j^n t}e^{\frac{i}{\hbar}\hat{H}_k^n \tau}e^{-\frac{i}{\hbar}\hat{H}_l^n \tau}\big] \\ &\equiv \Gamma^2 e^{i\omega_{ij}t}e^{i\omega_{kl}\tau}\prod_{n=1}^{N}\langle\hat{V}_{ij}(t)\hat{V}_{kl}(\tau)\rangle_n \end{aligned} \tag{A.4}$$

The single-mode terms $\{\langle\hat{V}_{ij}(t)\hat{V}_{kl}(\tau)\rangle_n\}$ can then be evaluated by performing the trace within the position representation and inserting closure relations, so as to express them in terms of matrix elements of the single-mode initial density matrix, $\langle x|\,\hat{\rho}_n(0)\,|x'\rangle$, and the propagators, $\langle x|\,e^{\pm i\hat{H}t/\hbar}\,|x'\rangle$, all of which can be obtained in closed form, e.g. by using path integral techniques.[220]

To demonstrate, consider $\langle\hat{V}_{DA}(t)\hat{V}_{DA}(\tau)\rangle_n$, for which

$$\begin{aligned}\langle\hat{V}_{DA}(t)\hat{V}_{DA}(\tau)\rangle_n = &\int \mathrm{d}x_0\mathrm{d}x_1\mathrm{d}x_2\mathrm{d}x_3\mathrm{d}x_4 \\ &\times\langle x_0|\,\hat{\rho}_n(0)\,|x_1\rangle\,\langle x_1|\,e^{\frac{i}{\hbar}\hat{H}_D^n t}\,|x_2\rangle\,\langle x_2|\,e^{-\frac{i}{\hbar}\hat{H}_A^n t}\,|x_3\rangle\,\langle x_3|\,e^{\frac{i}{\hbar}\hat{H}_D^n \tau}\,|x_4\rangle\,\langle x_4|\,e^{-\frac{i}{\hbar}\hat{H}_A^n \tau}\,|x_0\rangle\end{aligned} \tag{A.5}$$

$$\begin{aligned}\langle x|\,\hat{\rho}_n(0)\,|x'\rangle = &\Big(2\tanh(\frac{\beta\hbar\omega}{2})\sinh(\beta\hbar\omega)\Big)^{1/2}\Big(\frac{\omega}{2\pi\hbar\sinh(\beta\hbar\omega)}\Big)^{1/2} \\ &\times\exp\Big\{-\frac{\omega}{2\pi\hbar\sinh(\beta\hbar\omega)}\Big[(x^2+x'^2)\cosh(\beta\hbar\omega)-2xx'\Big]\Big\}\end{aligned} \tag{A.6}$$

$$\langle x|\,e^{\frac{i}{\hbar}\hat{H}_D^n t}\,|x'\rangle = \Big(\frac{i\omega}{2\pi\hbar\sin(\omega t)}\Big)^{1/2}\exp\Big\{\frac{\omega}{2\pi i\hbar\sin(\omega t)}\Big[\big(x^2+x'^2\big)\cos(\omega t)-2xx'\Big]\Big\} \tag{A.7}$$

$$\begin{aligned}\langle x|\,e^{\frac{i}{\hbar}\hat{H}_A^n t}\,|x'\rangle = &\Big(\frac{i\omega}{2\pi\hbar\sin(\omega t)}\Big)^{1/2} \\ &\times\exp\Big\{\frac{\omega}{2\pi i\hbar\sin(\omega t)}\Big[((x-R^{eq})^2+(x'-R^{eq})^2)\cos(\omega t)-2(x-R^{eq})(x'-R^{eq})\Big]\Big\}\end{aligned} \tag{A.8}$$

Thus, $\langle\hat{V}_{DA}(t)\hat{V}_{DA}(\tau)\rangle_n$ can be written as a 5-dimensional Gaussian integral:

$$\begin{aligned}\langle\hat{V}_{DA}(t)\hat{V}_{DA}(\tau)\rangle_n = &\frac{\sqrt{2(\omega/\hbar)^5\tanh(\beta\hbar\omega/2)}}{\sin(\omega t)\sin(\omega\tau)\sqrt{\det\mathbf{A}}} \\ &\times\int\mathrm{d}\mathbf{x}\exp\left(-\frac{1}{2}\mathbf{x}^T\mathbf{A}\mathbf{x}+\mathbf{b}^T\mathbf{x}+c\right)\end{aligned} \tag{A.9}$$

Here, $\mathbf{x}^T = [x_0, x_1, x_2, x_3, x_4]$, and the matrix $\mathbf{A}$, vector $\mathbf{b}$, and constant c are given by:

$$\mathbf{A} = \frac{\omega}{\hbar}\begin{pmatrix} \coth(\beta\hbar\omega) - i\cot(\omega\tau) & -\operatorname{csch}(\beta\hbar\omega) & 0 & 0 & i\csc(\omega\tau) \\ -\operatorname{csch}(\beta\hbar\omega) & \coth(\beta\hbar\omega) + i\cot(\omega t) & -i\csc(\omega t) & 0 & 0 \\ 0 & -i\csc(\omega t) & 0 & i\csc(\omega t) & 0 \\ 0 & 0 & i\csc(\omega t) & i\cot(\omega\tau) - i\cot(\omega t) & -i\csc(\omega\tau) \\ i\csc(\omega\tau) & 0 & 0 & -i\csc(\omega\tau) & 0 \end{pmatrix} \tag{A.10}$$

$$\mathbf{b} = i\frac{\omega R_{eq}}{\hbar}\begin{pmatrix} \dfrac{1-\cos(\omega\tau)}{\sin(\omega\tau)} \\ 0 \\ \dfrac{1-\cos(\omega t)}{\sin(\omega t)} \\ \dfrac{1-\cos(\omega t)}{\sin(\omega t)} \\ \dfrac{1-\cos(\omega\tau)}{\sin(\omega\tau)} \end{pmatrix} \tag{A.11}$$

$$c = -i\frac{\omega(R^{eq})^2}{\hbar}\left[\frac{1-\cos(\omega t)}{\sin(\omega t)} + \frac{1-\cos(\omega\tau)}{\sin(\omega\tau)}\right]$$

The 5-dimensional Gaussian integral can then be evaluated analytically, to obtain the following closed form expression for $\langle \hat{V}_{DA}(t)\hat{V}_{DA}(\tau)\rangle_n$:

$$\begin{aligned} &\langle \hat{V}_{DA}(t)\hat{V}_{DA}(\tau)\rangle_n \\ &\quad = \exp\left\{\frac{\omega(R^{eq})^2}{2\hbar}\coth\left(\frac{1}{2}\beta\hbar\omega\right)\Big[2\cos(\omega t) \right. \\ &\qquad \left. + 2\cos(\omega\tau) - 3 - \cos(\omega(t-\tau))\Big]\right\} \\ &\quad \times \exp\left\{i\frac{\omega(R^{eq})^2}{\hbar}\left[\frac{1}{2}\sin(\omega(t-\tau)) - \sin(\omega t)\right]\right\} \end{aligned} \tag{A.12}$$

Closed form expressions for the remaining three cases, $\langle \hat{V}_{DA}(t)\hat{V}_{AD}(\tau)\rangle_n$, $\langle \hat{V}_{AD}(t)\hat{V}_{DA}(\tau)\rangle_n$, and $\langle \hat{V}_{AD}(t)\hat{V}_{AD}(\tau)\rangle_n$ can be derived following a similar procedure, and are given in terms of a 5-dimensional Gaussian integral of the form of Eq. A.9, where the vector $\mathbf{b}$ and the constant c differ from one case to another, while the matrix $\mathbf{A}$ remains the same.

The quantities $\langle \hat{V}_{jk}(t)\rangle$ can also be evaluated in a similar way, by casting them in terms of

single-mode terms, $\{\langle \hat{V}_{jk}(t)\rangle_n\}$. For example, $\langle \hat{V}_{DA}(t)\rangle$, can be shown to be given in terms of a 3-dimensional Gaussian integral, which upon solving yields the following closed form expression:

$$\begin{aligned}\langle \hat{V}_{DA}(t)\rangle_n = & \left(\frac{\omega}{\hbar}\right)^{3/2} \frac{\sqrt{2\tanh(\beta\hbar\omega/2)}}{\sin(\omega t)\sqrt{\det \mathbf{A}}} \\ & \times \exp\left(\frac{1}{2}\mathbf{b}^T\mathbf{A}^{-1}\mathbf{b} + c\right)\end{aligned} \tag{A.13}$$

$$\mathbf{A} = \frac{\omega}{\hbar}\begin{pmatrix} \coth(\beta\hbar\omega) & -\operatorname{csch}(\beta\hbar\omega) & \csc(\omega t) \\ -i\cot(\omega t) & & \\ -\operatorname{csch}(\beta\hbar\omega) & \coth(\beta\hbar\omega) & -i\csc(\omega t) \\ & +i\cot(\omega t) & \\ \csc(\omega t) & -i\csc(\omega t) & 0 \end{pmatrix} \tag{A.14}$$

$$\mathbf{b} = i\frac{\omega R^{eq}}{\hbar}\begin{pmatrix} \dfrac{1-\cos(\omega t)}{\sin(\omega t)} \\ 0 \\ \dfrac{1-\cos(\omega t)}{\sin(\omega t)} \end{pmatrix} \tag{A.15}$$

$$c = -i\frac{\omega (R^{eq})^2}{\hbar}\frac{1-\cos(\omega t)}{\sin(\omega t)} \tag{A.16}$$

APPENDIX B

Bath discretization procedure

In this appendix, we outline the procedure used for obtaining a discrete set of frequencies from a spectral density $J(\omega)$. To this end, we start out by defining the density of modes,

$$\rho_b(\omega) \equiv \sum_{j=1}^{N_b} \delta\left(\omega - \omega_j\right) \,, \tag{B.1a}$$

where the number of bath modes to be generated by the discretization is given by N_b. $\rho_b(\omega)$ can be defined arbitrarily as long as the normalization condition

$$\int_0^\infty \mathrm{d}\omega \rho_b(\omega) = N_b \tag{B.1b}$$

is satisfied. In the current dissertation, the density of modes is defined as $\rho_b(\omega) = N_b J(\omega)/\omega U_b(\infty)$, where

$$U_b(\omega) = \int_0^\omega \mathrm{d}\omega' \, \frac{J(\omega')}{\omega'} \,. \tag{B.2}$$

The next step is to choose the discrete frequencies $\{\omega_1, \omega_2, \cdots, \omega_{N_b}\}$ from $\rho_b(\omega)$. These discrete frequencies divide the overall domain of frequencies into $N_b + 1$ intervals

$$\left[0, \infty\right) \to \left[0, \omega_1\right) \,,\ \left(\omega_1, \omega_2\right) \,, \cdots \,,\ \left(\omega_n, \omega_{n+1}\right) \,, \cdots \,,\ \left(\omega_{N_b - 1}, \omega_{N_b}\right) \,,\ \left(\omega_{N_b}, \infty\right) \,,$$

and the frequencies are chosen such that the $N_b + 1$ intervals divides the density of modes evenly, that is, $\left[0, \omega_1\right)$ and $\left(\omega_{N_b}, \infty\right)$ contain $1/2$ modes each, and each of $\left(\omega_n, \omega_{n+1}\right)$ contains 1 mode. As a result,

$$\int_0^{\omega_j} \mathrm{d}\omega \ \rho_b(\omega) = j - \frac{1}{2} \,, \tag{B.3}$$

which can be solved to give ω_j.

In the case of the GOA model, the spectral density defines the frequencies and coupling coeffi-

cients for the secondary modes, as given by Eq. 2.12. The coupling coefficients $\{c_j\}$ are evaluated by requiring that

$$\frac{J(\omega_j)}{\rho_b(\omega_j)} = \frac{\pi c_j^2}{2\omega_j} \,. \tag{B.4}$$

Substituting in the Ohmic form of the spectral density, the explicit forms of $\{\omega_j, c_j\}$ can be derived:

$$\omega_j = -\omega_c \ln\left(\frac{N_s + \frac{1}{2} - j}{N_s}\right) \tag{B.5a}$$

$$c_j = \sqrt{\frac{2\eta\omega_c}{\pi N_s}}\omega_j \tag{B.5b}$$

In the case of the Frenkel biexciton model, Eqs. 3.7c, 3.9, a similar procedure can be applied to yield the explicit forms of $\{\omega_j, R_j\}$ for the Ohmic-Lorentzian spectral density:

$$\omega_j = \omega_c\Big(\sqrt{\cot^2(\frac{j-\frac{1}{2}}{N_b}\pi) + 1} - \cot(\frac{j-\frac{1}{2}}{N_b}\pi)\Big) \tag{B.6a}$$

$$R_j = \sqrt{\frac{2\lambda}{N_b}}\omega_j^{-1} \,, \tag{B.6b}$$

where N_b is the number of modes for one site in this context, and the site index is omitted.

APPENDIX C

The 4th-order Runge-Kutta algorithm for solving TNL-OD-QMEs

In this appendix, we outline the numerical procedure that was used for solving the TNL-OD-QMEs Eq. 1.8. This corresponds to integro-differential equations of the form:

$$\dot{y}(t) = F\Big(t, y(t), \int_0^t \mathrm{d}s\; K(t, s, y(s))\Big) \tag{C.1}$$

The results reported in this paper were obtained by solving such equations via the 4th order Runge-Kutta algorithm proposed in Ref. 115.

Let $t^{(\alpha)} = \alpha h$, with $\alpha = 0, 1, \cdots$, and $y^{(\alpha)} = y(t^{(\alpha)})$. Then $y^{(\alpha+1)}$ is given by:[115]

$$\begin{aligned}
y^{(\alpha+1)} &= y^{\alpha} + h\sum_{i=1}^{s} b_i F(t^{\alpha} + c_i h, Y_i^{\alpha}, M_i^{\alpha} + N_i^{(\alpha)}) \\
Y_i^{(\alpha)} &= y^{\alpha} + h\sum_{j=1}^{s} a_{ij} F(t^{\alpha} + c_j h, Y_j^{\alpha}, M_j^{\alpha} + N_j^{(\alpha)}) \\
M_i^{(\alpha)} &= h\sum_{\beta=0}^{\alpha-1}\sum_{j=1}^{s} b_j K(t^{\alpha} + c_i h, t^{\beta} + c_j h, Y_j^{(\beta)}) \\
N_i^{(\alpha)} &= h\sum_{j=1}^{s} \bar{a}_{ij} K(t^{\alpha} + d_{ij} h, t^{\alpha} + c_j h, Y_j^{(\alpha)})
\end{aligned} \tag{C.2}$$

where $s > 0$ is the number of stages, and $a, \bar{a}, b, c, d$ are parameters that dictate the order of the Runge-Kutta solution. For this study, we use the following explicit 4th-order algorithm where

$a_{ij} = \bar{a}_{ij}, d_{ij} = e_j$:[115]

$$
\begin{array}{cccccccc}
e_i & c_i & & a_{ij} & & & & \\
\frac{1}{2} & 0 & 0 & & & & & \\
\frac{1}{2} & \frac{1}{2} & \frac{1}{2} & 0 & & & & \\
1 & \frac{1}{2} & 0 & \frac{1}{2} & 0 & & & \\
- & 1 & 0 & 0 & 1 & 0 & & \\
 & & \frac{1}{6} & \frac{1}{3} & \frac{1}{3} & \frac{1}{6} & & b_j
\end{array}
\tag{C.3}
$$

APPENDIX D

Dynamics in the rotating frame

We start from the complete form of the Hamiltonian $\hat{H}_{\mathrm{tot}} = \hat{H} + \hat{H}_{\mathrm{b}}$ without omitting the band gap:

$$\hat{H} = \sum_j \hat{H}_j^g \hat{B}_j \hat{B}_j^\dagger + \sum_j \left(\Delta_j + \hat{H}_j^e\right) \hat{B}_j^\dagger \hat{B}_j + \sum_{j \neq k} \Gamma_{jk} \hat{B}_j^\dagger \hat{B}_k \tag{D.1a}$$

$$\hat{H}_{\mathrm{b}} = \hbar\omega_0 \sum_j \hat{B}_j^\dagger \hat{B}_j \tag{D.1b}$$

It is easy to show that the band gap Hamiltonian $\hat{H}_{\mathrm{b}}$ commutes with $\hat{H}$, therefore we can define the dynamics in the rotating frame as

$$\begin{aligned} \hat{\rho}^{\mathrm{rot}}(t) &= e^{\frac{i}{\hbar}\hat{H}_{\mathrm{b}}t} \hat{\rho}(t) e^{-\frac{i}{\hbar}\hat{H}_{\mathrm{b}}t} && \text{(D.2a)} \\ &= e^{\frac{i}{\hbar}\hat{H}_{\mathrm{b}}t} e^{-\frac{i}{\hbar}\hat{H}_{\mathrm{b}}t} e^{-\frac{i}{\hbar}\hat{H}t} \hat{\rho}(0) e^{\frac{i}{\hbar}\hat{H}t} e^{\frac{i}{\hbar}\hat{H}_{\mathrm{b}}t} e^{-\frac{i}{\hbar}\hat{H}_{\mathrm{b}}t} \\ &= e^{-\frac{i}{\hbar}\hat{H}t} \hat{\rho}^{\mathrm{rot}}(0) e^{\frac{i}{\hbar}\hat{H}t}\,, && \text{(D.2b)} \end{aligned}$$

that is, the dynamics in the rotating frame is governed by the rotating frame Hamiltonian Eq. 3.1, where the band gap is ignored.

We now turn to the absorption lineshape, which is defined as the Fourier transform of the linear optical response function

$$\begin{aligned} I(\omega) &= 2\pi \mathrm{Im} \int_0^\infty \mathrm{d}t\, \frac{i}{\hbar} \mathrm{Tr}\left[\hat{\mu}\, e^{-\frac{i}{\hbar}\hat{H}_{\mathrm{tot}}t} [\hat{\mu}, \hat{\rho}^{\mathrm{eq}}] e^{\frac{i}{\hbar}\hat{H}_{\mathrm{tot}}t}\right] e^{i\omega t} && \text{(D.3a)} \\ &= \mathrm{Re} \int_0^\infty \mathrm{d}t\, \mathrm{Tr}\left[e^{\frac{i}{\hbar}\hat{H}_{\mathrm{b}}t} \hat{\mu} e^{-\frac{i}{\hbar}\hat{H}_{\mathrm{b}}t}\, e^{-\frac{i}{\hbar}\hat{H}t} [\hat{\mu}, \hat{\rho}^{\mathrm{eq}}] e^{\frac{i}{\hbar}\hat{H}t}\right] e^{i\omega t}\,, && \text{(D.3b)} \end{aligned}$$

where the prefactor is ignored in Eq. D.3b since only the relative strength of the lineshape is

important, and the dipole operator in the rotating frame is given as:

$$\begin{aligned} e^{\frac{i}{\hbar}\hat{H}_{\mathrm{b}}t}\hat{\mu}e^{-\frac{i}{\hbar}\hat{H}_{\mathrm{b}}t} &= \sum_j e^{i\omega_0 t\hat{B}_j^\dagger\hat{B}_j}\left[\hat{B}_j\mu_j + \hat{B}_j^\dagger\mu_j^*\right]e^{-i\omega_0 t\hat{B}_j^\dagger\hat{B}_j} \\ &= \sum_j \left[\hat{B}_j^\dagger\hat{B}_j e^{i\omega_0 t} + \hat{B}_j\hat{B}_j^\dagger\right]\left[\hat{B}_j\mu_j + \hat{B}_j^\dagger\mu_j^*\right]\left[\hat{B}_j^\dagger\hat{B}_j e^{-i\omega_0 t} + \hat{B}_j\hat{B}_j^\dagger\right] \\ &= \sum_j \hat{B}_j\mu_j e^{-i\omega_0 t} + \hat{B}_j^\dagger\mu_j^* e^{i\omega_0 t} = \hat{\mu}_{\mathrm{u}}e^{-i\omega_0 t} + \hat{\mu}_{\mathrm{u}}^\dagger e^{i\omega_0 t} \end{aligned} \tag{D.4}$$

On the other hand, only the inter-band coherence will be populated after the initial interaction with the dipole operator:

$$\hat{\mu}\hat{\rho}^{\mathrm{eq}} = \sum_j \mu_j\hat{\rho}_N^{\mathrm{eq}} \otimes \hat{B}_j^\dagger \prod_{k\neq j}\hat{B}_k\hat{B}_k^\dagger \,. \tag{D.5a}$$

Since the Hamiltonian does not contain inter-band coupling, no other matrix elements of the electronic density will be populated throughout the dynamics, whose general form can be written as

$$e^{-\frac{i}{\hbar}\hat{H}t}\hat{\mu}\hat{\rho}^{\mathrm{eq}}e^{\frac{i}{\hbar}\hat{H}t} = \sum_j \zeta_j(t)\hat{\rho}_{N,j}(t) \otimes \hat{B}_j^\dagger \prod_{k\neq j}\hat{B}_k\hat{B}_k^\dagger \,, \tag{D.5b}$$

which can be confirmed by inspecting $[\hat{H}, \exp(\frac{i}{\hbar}\hat{H}t)\hat{\mu}\hat{\rho}^{\mathrm{eq}}\exp(\frac{i}{\hbar}\hat{H}t)]$. Hence, only two terms survive in Eq. D.3b:

$$\begin{aligned} I(\omega) = \mathrm{Re}\int_0^\infty \mathrm{d}t\ \mathrm{Tr}\left[\hat{\mu}_{\mathrm{u}}\, e^{-\frac{i}{\hbar}\hat{H}t}\hat{\mu}\hat{\rho}^{\mathrm{eq}}e^{\frac{i}{\hbar}\hat{H}t}\right]e^{i(\omega-\omega_0)t} \\ - \mathrm{Re}\int_0^\infty \mathrm{d}t\ \mathrm{Tr}\left[\hat{\mu}_{\mathrm{u}}^\dagger\, e^{-\frac{i}{\hbar}\hat{H}t}\hat{\rho}^{\mathrm{eq}}\hat{\mu}e^{\frac{i}{\hbar}\hat{H}t}\right]e^{i(\omega+\omega_0)t} \,. \end{aligned} \tag{D.6}$$

Since the band gap $\hbar\omega_0$ is assumed to be much larger than either the detuning Δ or the electronic coupling Γ, the lineshape consists of two sets of features centered around ω_0 and $-\omega_0$ (this is often referred to as the rotating wave approximation). Here, we will focus on the lineshape around ω_0, removing the $\exp\{i(\omega+\omega_0)t\}$ term and shifting the frequency coordinate to originate from $\omega = \omega_0$, yielding Eq. 3.2a.

BIBLIOGRAPHY

[1] A. Nitzan, *Chemical Dynamics in Condensed Phases* (Oxford University Press, New York, 2006).

[2] S. Mukamel, *Principles of Nonlinear Optical Spectroscopy* (Oxford University Press, Oxford, 1995).

[3] V. May, O. Kühn, *Charge and Energy Transfer Dynamics in Molecular Systems* (Willey-VCH, Berlin, 2000).

[4] H.-D. Meyer, F. Gatti, G. Worth, *Multidimensional Quantum Dynamics*, MCTDH Theory and Applications (John Wiley & Sons, 2009).

[5] N. Makri, *Annu. Rev. Phys. Chem.* **50**, 167 (1999).

[6] J. Jin, X. Zheng, Y. Yan, *J. Chem. Phys.* **128**, 234703 (2008).

[7] Y. Tanimura, R. Kubo, *J. Phys. Soc. Jpn.* **58**, 101 (1989).

[8] S. M. Greene, V. S. Batista, *J. Chem. Theory Comput.* **13**, 4034 (2017).

[9] A. McLachlan, *Mol. Phys.* **8**, 39 (1964).

[10] J. Tully, *J. Chem. Phys.* **93**, 1061 (1990).

[11] J. Tully, R. Preston, *J. Chem. Phys.* **55**, 562 (1971).

[12] E. Bittner, P. Rossky, *J. Chem. Phys.* **103**, 8130 (1995).

[13] O. Prezhdo, P. Rossky, *J. Chem. Phys.* **107**, 5863 (1997).

[14] I. Horenko, C. Salzmann, B. Schmidt, C. Schutte, *J. Chem. Phys.* **117**, 11075 (2002).

[15] J. E. Subotnik, N. Shenvi, *J. Chem. Phys.* **134**, 024105 (2011).

[16] P. Shushkov, R. Li, J. Tully, *J. Chem. Phys.* **137**, 22A549 (2012).

[17] L. Wang, D. Trivedi, O. Prezhdo, *J. Chem. Theory Comput.* **10**, 3598 (2014).

[18] H. Jaeger, S. Fischer, O. Prezhdo, *J. Chem. Phys.* **137**, 22A545 (2012).

[19] L. Wang, O. Prezhdo, *J. Phys. Chem. Lett.* **5**, 713 (2014).

[20] W. Ouyang, W. Dou, J. Subotnik, *J. Chem. Phys.* **142**, 084109 (2015).

[21] M. Bedard-Hearn, R. Larsen, B. Schwartz, *J. Chem. Phys.* **123**, 234106 (2005).

[22] C. Martens, J.-Y. Fang, *J. Chem. Phys.* **106**, 4918 (1997).

[23] A. Donoso, C. Martens, *J. Phys. Chem. A* **102**, 4291 (1998).

[24] R. Kapral, G. Ciccotti, *J. Chem. Phys.* **110**, 8919 (1999).

[25] S. Nielsen, R. Kapral, G. Ciccotti, *J. Chem. Phys.* **112**, 6543 (2000).

[26] Q. Shi, E. Geva, *J. Chem. Phys.* **121**, 3393 (2004).

[27] D. MacKernan, R. Kapral, G. Ciccotti, *J. Phys.: Condens. Matter* **14**, 9069 (2002).

[28] D. MacKernan, G. Ciccotti, R. Kapral, *J. Phys. Chem. B* **112**, 424 (2008).

[29] H. Meyer, W. Miller, *J. Chem. Phys.* **70**, 3214 (1979).

[30] G. Stock, M. Thoss, *Phys. Rev. Lett.* **78**, 578 (1997).

[31] A. Kelly, R. van Zon, J. Schofield, R. Kapral, *J. Chem. Phys.* **136**, 084101 (2012).

[32] S. J. Cotton, W. H. Miller, *J. Chem. Phys.* **139**, 234112 (2013).

[33] S. Cotton, W. Miller, *J. Phys. Chem. A* **117**, 7190 (2013).

[34] S. Cotton, K. Igumenshchev, W. Miller, *J. Chem. Phys.* **141**, 084104 (2014).

[35] S. Cotton, W. Miller, *J. Phys. Chem. A* **119**, 12138 (2015).

[36] S. Cotton, W. Miller, *J. Chem. Theory Comput.* **12**, 983 (2016).

[37] S. Cotton, W. Miller, *J. Chem. Phys.* **145**, 144108 (2016).

[38] Y. Liu, X. Gao, Y. Lai, E. Mulvihill, E. Geva, *J. Chem. Theory Comput.* **16**, 4479 (2020).

[39] J. Runeson, J. Richardson, *J. Chem. Phys.* **151**, 044119 (2019).

[40] X. Gao, *et al.*, *J. Chem. Theory Comput.* **16**, 2883 (2020).

[41] M. Saller, A. Kelly, J. Richardson, *J. Chem. Phys.* **150**, 071101 (2019).

[42] M. Saller, A. Kelly, J. Richardson, *Faraday Discuss.* **221**, 150 (2020).

[43] R. D. Coalson, D. G. Evans, A. Nitzan, *J. Chem. Phys.* **101**, 436 (1994).

[44] A. Izmaylov, *et al.*, *J. Chem. Phys.* **135**, 234106 (2011).

[45] X. Sun, E. Geva, *J. Phys. Chem. A* **120**, 2976 (2016).

[46] X. Sun, E. Geva, *J. Chem. Theory Comput.* **12**, 2926 (2016).

[47] X. Sun, E. Geva, *J. Chem. Phys.* **144**, 244105 (2016).

[48] X. Sun, E. Geva, *J. Chem. Phys.* **145**, 064109 (2016).

[49] X. Sun, *et al.*, *J. Phys. Chem. C* **122**, 11288 (2018).

[50] A. Trushechkin, *J. Chem. Phys.* **151**, 074101 (2019).

[51] A. Pereverzev, E. R. Bittner, *J. Chem. Phys.* **125**, 104906 (2006).

[52] V. M. Kenkre, R. S. Knox, *Phys. Rev. B* **9**, 5279 (1974).

[53] I. I. Abram, R. Silbey, *J. Chem. Phys.* **63**, 2317 (1975).

[54] M. Sparpaglione, S. Mukamel, *J. Chem. Phys.* **88**, 3263 (1988).

[55] P. de Bree, D. A. Wiersma, *J. Chem. Phys.* **70**, 790 (1979).

[56] D. Egorova, A. Kühl, W. Domcke, *Chem. Phys.* **268**, 105 (2001).

[57] A. Ishizaki, G. R. Fleming, *Proc. Natl. Acad. Sci. U.S.A.* **106**, 17255 (2009).

[58] A. Kühl, W. Domcke, *J. Chem. Phys.* **116**, 263 (2002).

[59] V. Novoderezhkin, A. Yakovlev, R. van Grondelle, V. Shuvalov, *J. Phys. Chem. B* **108**, 7445 (2004).

[60] W. Pollard, R. Friesner, *J. Chem. Phys.* **100**, 5054 (1994).

[61] S. Nakajima, *Prog. Theor. Phys.* **20**, 948 (1958).

[62] R. Zwanzig, *J. Chem. Phys.* **33**, 1338 (1960).

[63] Q. Shi, E. Geva, *J. Chem. Phys.* **119**, 12063 (2003).

[64] Q. Shi, E. Geva, *J. Chem. Phys.* **120**, 10647 (2004).

[65] M.-L. Zhang, B. J. Ka, E. Geva, *J. Chem. Phys.* **125**, 044106 (2006).

[66] A. Kelly, T. Markland, *J. Chem. Phys.* **139**, 014104 (2013).

[67] L. Kidon, E. Wilner, E. Rabani, *J. Chem. Phys.* **143**, 234110 (2015).

[68] A. Montoya-Castillo, D. Reichman, *J. Chem. Phys.* **144**, 184104 (2016).

[69] J. Cerrillo, J. Cao, *Phys. Rev. Lett.* **112**, 110401 (2014).

[70] A. Kananenka, C.-Y. Hsieh, J. Cao, E. Geva, *J. Phys. Chem. Lett.* **7**, 4809 (2016).

[71] E. Mulvihill, A. Schubert, X. Sun, B. Dunietz, E. Geva, *J. Chem. Phys.* **150**, 034101 (2019).

[72] E. Mulvihill, *et al.*, *J. Chem. Phys.* **151**, 074103 (2019).

[73] Z. Tong, *et al.*, *J. Chem. Phys.* **153**, 044105 (2020).

[74] D. Brian, Z. Liu, B. Dunietz, E. Geva, X. Sun, *J. Chem. Phys.* **154**, 174105 (2021).

[75] B. Ka, M.-L. Zhang, E. Geva, *J. Chem. Phys.* **125**, 124509 (2006).

[76] G. Cohen, E. Rabani, *Phys. Rev. B* **84**, 075150 (2011).

[77] E. Y. Wilner, H. Wang, G. Cohen, M. Thoss, E. Rabani, *Phys. Rev. B* **88**, 045137 (2013).

[78] G. Cohen, E. Y. Wilner, E. Rabani, *New J. Phys.* **15**, 073018 (2013).

[79] G. Cohen, E. Gull, D. R. Reichman, A. J. Millis, E. Rabani, *Phys. Rev. B* **87**, 195108 (2013).

[80] W. C. Pfalzgraff, A. Kelly, T. E. Markland, *J. Chem. Phys.* **6**, 4743 (2015).

[81] A. Kelly, N. Brackbill, T. E. Markland, *J. Chem. Phys.* **142**, 094110 (2015).

[82] A. Kelly, A. Montoya-Castillo, L. Wang, T. Markland, *J. Chem. Phys.* **144**, 184105 (2016).

[83] L. Kidon, H. Wang, M. Thoss, E. Rabani, *J. Chem. Phys.* **149**, 104105 (2018).

[84] W. Pfalzgraff, A. Montoya-Castillo, A. Kelly, T. Markland, *J. Chem. Phys.* **150**, 244109 (2019).

[85] E. Mulvihill, *et al.*, *J. Chem. Phys.* **154**, 204109 (2021).

[86] H.-P. Breuer, F. Petruccione, *The Theory of Open Quantum Systems* (Oxford University Press, New York, 2006).

[87] F. Shibata, Y. Takahashi, N. Hashitsume, *J. Stat. Phys.* **17**, 171 (1977).

[88] S. Chaturvedi, F. Shibata, *Z. Phys. B* **35**, 297 (1979).

[89] F. Shibata, T. Arimitsu, *J. Phys. Soc. Jpn.* **49**, 891 (1980).

[90] A. G. Redfield, *IBM J. Res. Dev.* **1**, 19 (1957).

[91] W. T. Pollard, A. K. Felts, R. A. Friesner, *Adv. Chem. Phys.* **XCIII**, 77 (1996).

[92] C. Meier, D. Tannor, *J. Chem. Phys.* **111**, 3365 (1999).

[93] A. Ishizaki, G. Fleming, *J. Chem. Phys.* **130**, 234110 (2009).

[94] S. J. Jang, *Dynamics of Molecular Excitons* (Elsevier, 2020).

[95] C. Baiz, K. Kubarych, E. Geva, *J. Phys. Chem. B* **115**, 5322 (2011).

[96] B. B. Laird, J. Budimir, J. L. Skinner, *J. Chem. Phys.* **94**, 4391 (1991).

[97] W. M. Zhang, T. Meier, V. Chernyak, S. Mukamel, *J. Chem. Phys.* **108**, 7763 (1998).

[98] M. Yang, G. Fleming, *Chem. Phys.* **282**, 163 (2002).

[99] M. Schröder, U. Kleinekathöfer, M. Schreiber, *J. Chem. Phys.* **124**, 084903 (2006).

[100] D. Xu, K. Schulten, *Chem. Phys.* **182**, 91 (1994).

[101] Y. Ohta, A. V. Soudackov, S. Hammes-Schiffer, *J. Chem. Phys.* **125**, 144522 (2006).

[102] Y. Zhao, W. Liang, *Chem. Soc. Rev.* **41**, 1075 (2012).

[103] Y. Lai, E. Geva, *J. Chem. Phys.* **155**, 204101 (2021).

[104] R. Zwanzig, *Nonequilibrium Statistical Mechanics* (Oxford University Press, New York, 2001).

[105] S. Mukamel, *Principles of Nonlinear Optical Spectroscopy* (Oxford, New York, 1995).

[106] A. A. Golosov, D. R. Reichman, *J. Chem. Phys.* **115**, 9848 (2001).

[107] A. A. Golosov, D. R. Reichman, *J. Chem. Phys.* **115**, 9862 (2001).

[108] J. Seibt, T. Mančal, *J. Chem. Phys.* **146**, 174109 (2017).

[109] Z. Gong, J. Wu, *J. Chem. Phys.* **148**, 234107 (2018).

[110] D. G. Evans, R. D. Coalson, *J. Chem. Phys.* **102**, 5658 (1995).

[111] S. Jang, S. Hoyer, G. Fleming, K. B. Whaley, *Phys. Rev. Lett.* **113**, 188102 (2014).

[112] M. Cho, R. J. Silbey, *J. Chem. Phys.* **103**, 595 (1995).

[113] A. Garg, J. N. Onuchic, V. Ambegaokar, *J. Chem. Phys.* **83**, 4491 (1985).

[114] X. Sun, E. Geva, *J. Chem. Phys.* **144**, 044106 (2016).

[115] C. Lubich, *Numer. Math.* **40**, 119 (1982).

[116] G. A. Worth, M. H. Beck, A. Jäckle, O. Vendrell, H.-D. Meyer, The MCTDH Package, Version 8.2, (2000). H.-D. Meyer, Version 8.3 (2002), Version 8.4 (2007). O. Vendrell and H.-D. Meyer Version 8.5 (2013). Version 8.5 contains the ML-MCTDH algorithm. Current versions: 8.4.18 and 8.5.11 (2020). See http://mctdh.uni-hd.de/.

[117] S. Jang, T. C. Berkelbach, D. R. Reichman, *New J. Phys.* **15**, 105020 (2013).

[118] C. H. Fleming, N. I. Cummings, *Phys. Rev. E* **83**, 031117 (2011).

[119] S. Jang, J. Cao, R. J. Silbey, *J. Chem. Phys.* **116**, 2705 (2002).

[120] D. M. Jonas, *Annu. Rev. Phys. Chem.* **54**, 425 (2003).

[121] M. Cho, *Chem. Rev.* **108**, 1331 (2008).

[122] J. Ogilvie, K. Kubarych, *Advances in Atomic, Molecular, and Optical Physics* **57**, 249 (2009).

[123] S. Mukamel, H. Bakker, *J. Chem. Phys.* **142**, 212101 (2015).

[124] B. Ka, E. Geva, *J. Chem. Phys.* **125**, 214501 (2006).

[125] P. McRobbie, E. Geva, *J. Phys. Chem. A* **113**, 10425 (2009).

[126] P. McRobbie, G. Hanna, Q. Shi, E. Geva, *Acc. Chem. Res.* **42**, 1299 (2009).

[127] G. Hanna, E. Geva, *J. Phys. Chem. B* **112**, 12991 (2008).

[128] G. Hanna, E. Geva, *J. Phys. Chem. B* **112**, 15793 (2008).

[129] G. Hanna, E. Geva, *J. Phys. Chem. B* **113**, 9278 (2009).

[130] G. Hanna, E. Geva, *Chem. Phys.* **370**, 201 (2010).

[131] G. Hanna, E. Geva, *J. Phys. Chem. B* **115**, 5191 (2010).

[132] C. Baiz, K. Kubarych, E. Geva, *J. Phys. Chem. A* **113**, 9617 (2009).

[133] C. Baiz, K. Kubarych, E. Geva, E. Sibert III, *J. Phys. Chem. A* **115**, 5354 (2011).

[134] K. Kwac, E. Geva, *J. Phys. Chem. B* **116**, 2856 (2012).

[135] K. Kwac, E. Geva, *J. Phys. Chem. B* **117**, 7737 (2013).

[136] K. Kwac, E. Geva, *J. Phys. Chem. B* **117**, 9996 (2013).

[137] K. Kwac, E. Geva, *J. Phys. Chem. B* **117**, 14457 (2013).

[138] S. Bai, W. Xie, L. Zhu, Q. Shi, *J. Chem. Phys.* **140**, 084105 (2014).

[139] S. Gruenbaum, R. Loring, *J. Chem. Phys.* **129**, 124510 (2008).

[140] A. Petit, J. Subotnik, *J. Chem. Theory Comput.* **11**, 4328 (2015).

[141] A. Jain, A. Petit, J. Anna, J. Subotnik, *J. Phys. Chem. B* **123**, 1602 (2019).

[142] C. van der Vegte, A. Dijkstra, J. Knoester, T. Jansen, *J. Phys. Chem. A* **117**, 5970 (2013).

[143] R. Tempelaar, C. van der Vegte, J. Knoester, T. Jansen, *J. Chem. Phys.* **138**, 164106 (2013).

[144] J. Provazza, F. Segatta, M. Garavelli, D. Coker, *J. Chem. Theory Comput.* **14**, 856 (2018).

[145] M. Richter, B. Fingerhut, *J. Chem. Theory Comput.* **12**, 3284 (2016).

[146] V. I. Novoderezhkin, M. A. Palacios, H. van Amerongen, R. van Grondelle, *J. Phys. Chem. B* **108**, 10363 (2004).

[147] V. I. Novoderezhkin, J. P. Dekker, R. van Grondelle, *Biophysical Journal* **93**, 1293 (2007).

[148] Z. Wang, A. Pakoulev, Y. Pang, D. D. Dlott, *Chem. Phys. Lett.* **378**, 281 (2003).

[149] Timothy Berkelbach, pyrho: A python package for reduced density matrix techniques. https://github.com/berkelbach-group/pyrho.

[150] X. Gao, Y. Lai, E. Geva, *J. Chem. Theory Comput.* **16**, 6465 (2020).

[151] J. H. Fetherolf, T. C. Berkelbach, *J. Chem. Phys.* **147**, 244109 (2017).

[152] D. Lidzey, D. Bradley, A. Armitage, S. Walker, M. Skolnick, *Science* **288**, 1620 (2000).

[153] J. Tischler, M. Bradley, V. Bulović, J. Song, A. Nurmikko, *Phys. Rev. Lett.* **95**, 1 (2005).

[154] S. Kéna-Cohen, M. Davanço, S. Forrest, *Phys. Rev. Lett.* **101**, 1337 (2008).

[155] S. Kéna-Cohen, S. Forrest, *Nat. Photonics* **4**, 371 (2010).

[156] J. Hutchison, *et al.*, *Adv. Mater.* **25**, 2481 (2013).

[157] J. Bellessa, *et al.*, *Electronics* **3**, 303 (2014).

[158] T. Schwartz, J. Hutchison, C. Genet, T. Ebbesen, *Phys. Rev. Lett.* **106**, 196405 (2011).

[159] S. Kéna-Cohen, S. Maier, D. Bradley, *Adv. Opt. Mater.* **1**, 827 (2013).

[160] M. Mazzeo, *et al.*, *Appl. Phys. Lett.* **104**, 233303 (2014).

[161] J. George, *et al.*, *Faraday Discuss.* **178**, 281 (2015).

[162] P. A. M. Dirac, *The principles of quantum mechanics* (Oxford, Clarendon Press, 1958).

[163] W. H. Louisell, *Radiation and Noise in Quantum Electronics* (Mcgraw-Hill, N.Y., 1964).

[164] R. Loudon, *The quantum theory of light* (Oxford University Press, New York, 1986).

[165] H. Walther, B. Varcoe, B.-G. Englert, T. Becker, *Rep. Prog. Phys.* **69**, 1325 (2006).

[166] P. Andrew, W. L. Barnes, *Science* **290**, 785 (2000).

[167] J. Hutchison, T. Schwartz, C. Genet, E. Devaux, T. Ebbesen, *Angew. Chem. Int.* **51**, 1592 (2012).

[168] P. Törmä, W. Barnes, *Rep. Prog. Phys.* **78**, 013901 (2014).

[169] J. Flick, M. Ruggenthaler, H. Appel, A. Rubio, *Proc. Natl. Acad. Sci. USA* **112**, 15285 (2015).

[170] J. Feist, F. Garcia-Vidal, *Phys. Rev. Lett.* **114**, 196402 (2015).

[171] J. Schachenmayer, C. Genes, E. Tignone, G. Pupillo, *Phys. Rev. Lett.* **114**, 196403 (2015).

[172] A. Shalabney, *et al.*, *Nat. Commun.* **6**, 217 (2015).

[173] E. Orgiu, *et al.*, *Nat. Mater.* **14**, 1123 (2015).

[174] J. Long, B. Simpkins, *ACS Photonics* **2**, 130 (2015).

[175] T. Ebbesen, *Acc. Chem. Res.* **49**, 2403 (2016).

[176] A. Thomas, *et al.*, *Angew. Chem.* **128**, 11634 (2016).

[177] X. Zhong, *et al.*, *Angew. Chem.* **128**, 6310 (2016).

[178] F. Herrera, F. Spano, *Phys. Rev. Lett.* **116**, 238301 (2016).

[179] S. Casey, J. Sparks, *J. Phys. Chem. C* **120**, 28138 (2016).

[180] D. Sanvitto, S. Kéna-Cohen, *Nat. Mater.* **15**, 1061 (2016).

[181] M. Kowalewski, K. Bennett, S. Mukamel, *J. Phys. Chem. Lett.* **7**, 2050 (2016).

[182] M. Kowalewski, K. Bennett, S. Mukamel, *J. Chem. Phys.* **144**, 054309 (2016).

[183] J. Flick, M. Ruggenthaler, H. Appel, A. Rubio, *Proc. Natl. Acad. Sci. USA* **114**, 3026 (2017).

[184] X. Zhong, *et al.*, *Angew. Chem. Int. Ed.* **56**, 9034 (2017).

[185] L. Martínez-Martínez, R. Ribeiro, J. Campos-González-Angulo, J. Yuen-Zhou, *ACS Photonics* **5**, 167 (2017).

[186] J. Fregoni, G. Granucci, E. Coccia, M. Persico, S. Corni, *Nat. Commun.* **9**, 2613 (2018).

[187] R. Sáez-Blázquez, J. Feist, A. Fernández-Domínguez, F. García-Vidal, *Phys. Rev. B* **97**, 241407 (2018).

[188] J. Flick, D. Welakuh, M. Ruggenthaler, H. Appel, A. Rubio, *ACS Photonics* **6**, 2757 (2019).

[189] J. Galego, C. Climent, F. Garcia-Vidal, J. Feist, *Phys. Rev. X* **9**, 021057 (2019).

[190] J. Lather, P. Bhatt, A. Thomas, T. Ebbesen, J. George, *Angew. Chem. Int. Ed.* **58**, 10635 (2019).

[191] C. Schäfer, M. Ruggenthaler, H. Appel, A. Rubio, *Proc. Natl. Acad. Sci. USA* **116**, 4883 (2019).

[192] N. Hoffmann, C. Schäfer, A. Rubio, A. Kelly, H. Appel, *Phys. Rev. A* **99**, 063819 (2019).

[193] N. Hoffmann, *et al.*, *J. Chem. Phys.* **151**, 244113 (2019).

[194] L. Lacombe, N. Hoffmann, N. Maitra, *Phys. Rev. Lett.* **123**, 083201 (2019).

[195] A. Mandal, P. Huo, *J. Phys. Chem. Lett.* **10**, 5519 (2019).

[196] N. Hoffmann, L. Lacombe, A. Rubio, N. Maitra, *arXiv e-prints* p. arXiv:2001.07330 (2020).

[197] J. Flick, N. Rivera, P. Narang, *Nanophotonics* **7**, 1479 (2020).

[198] B. Gu, S. Mukamel, *Chem. Sci.* **11**, 1290 (2020).

[199] A. Mandal, T. Krauss, P. Huo, *J. Phys. Chem. B* **124**, 6321 (2020).

[200] M. A. C. Saller, A. Kelly, E. Geva, *J. Phys. Chem. Lett.* **12**, 3163 (2021).

[201] S. N. Chowdhury, A. Mandal, P. Huo, *J. Chem. Phys.* **154**, 044109 (2021).

[202] N. Makri, *J. Phys. Chem. B* **103**, 2823 (1999).

[203] I. Muegge, P. X. Qi, A. J. Wand, Z. T. Chu, A. Warshel, *J. Chem. Phys. B* **101**, 825 (1997).

[204] E. Romero, V. I. Novoderezhkin, R. van Grondelle, *Nature* **543**, 355 (2017).

[205] G. Bottari, G. de la Torre, D. M. Guldi, T. Torres, *Chem. Rev.* **110**, 6768 (2010).

[206] A. Rizzi, *et al.*, *J. Phys. Chem. A* **112**, 4215 (2008).

[207] H. Tian, Z. Yu, A. Hagfeldt, L. Kloo, L. Sun, *J. Am. Chem. Soc.* **133**, 9413 (2011).

[208] A. Mishra, M. Fischer, P. Bäuerle, *Angew. Chem. Int. Ed.* **48**, 2474 (2009).

[209] S. M. Feldt, *et al.*, *J. Am. Chem. Soc.* **132**, 16714 (2010).

[210] R. A. Marcus, *J. Chem. Phys.* **24**, 966 (1956).

[211] R. A. Marcus, *J. Chem. Phys.* **24**, 979 (1956).

[212] R. Marcus, *Rev. Mod. Phys.* **65**, 599 (1993).

[213] P. F. Barbara, T. J. Meyer, M. A. Ratner, *J. Phys. Chem.* **100**, 13148 (1996).

[214] A. J. Leggett, *et al.*, *Rev. Mod. Phys.* **59**, 1 (1987).

[215] J. Cao, G. A. Voth, *J. Chem. Phys.* **102**, 3337 (1995).

[216] U. Weiss, *Quantum dissipative systems* (World Scientific, Singapore, 1999).

[217] Q. Shi, E. Geva, *J. Phys. Chem. A* **108**, 6109 (2004).

[218] A. Manna, D. Balamurugan, M. Cheung, B. Dunietz, *J. Phys. Chem. Lett.* **6**, 1231 (2015).

[219] R. P. Feynman, A. R. Hibbs, *Quantum Mechanics and Path Integrals* (McGraw-Hill, New York, 1965).

[220] L. S. Schulman, *Techniques and applications of path integration* (Wiley, New York, 1981).

[221] H. Kleinert, *Path integrals in quantum mechanics, statistics and polymer physics* (World Scientific, New Jersey, 1995).

[222] Q. Shi, E. Geva, *J. Chem. Phys.* **118**, 8173 (2003).

[223] Q. Shi, E. Geva, *J. Chem. Phys.* **129**, 124505 (2008).

[224] M. Hillery, R. F. O'Connell, M. O. Scully, E. P. Wigner, *Phys. Rep.* **106**, 121 (1984).

[225] W. H. Press, B. P. Flannery, S. A. Teukolsky, W. T. Vetterling, *Numerical Recipes* (Cambridge University Press, Cambridge, 1986).

[226] P. Liddell, *et al.*, *J. Am. Chem. Soc.* **119**, 1400 (1997).

[227] D. Carbonera, M. Di Valentin, C. Corvaja, *J. Am. Chem. Soc.* **120**, 4398 (1998).

[228] D. Gust, T. A. Moore, A. L. Moore, *Acc. Chem. Res.* **34**, 40 (2001).

[229] A. A. Voityuk, N. Rösch, *J. Chem. Phys.* **117**, 5607 (2002).

[230] D. Balamurugan, *et al.*, *J. Phys. Chem. B* **117**, 12065 (2013).

[231] A. Jakalian, D. B. Jack, C. I. Bayly, *J. Comp. Chem.* **23**, 1623 (2002).

[232] D. Case, *et al.*, *AMBER 14* (University of California, San Francisco, 2014).

[233] O. N. Starovoytov, P. Zhang, P. Cieplak, M. S. Cheung, *Phys. Chem. Chem. Phys.* **19**, 22969 (2017).

[234] W. D. Cornell, *et al.*, *J. Am. Chem. Soc.* **117**, 5179 (1995).

[235] W. Cornell, *et al.*, *J. Am. Chem. Soc.* **118**, 2309 (1996).

[236] J. Wang, R. M. Wolf, J. W. Caldwell, P. A. Kollamn, D. A. Case, *J. Comput. Chem.* **25**, 1157 (2004).

[237] G. Ciccotti, J. P. Ryckaert, *Computer Physics Reports* **4**, 345 (1986).

[238] T. Darden, D. York, L. Pedersen, *J. Chem. Phys.* **98**, 10089 (1993).

[239] S. N. Smirnov, *et al.*, *J. Phys. Chem. A* **107**, 7567 (2003).

[240] G. King, A. Warshel, *J. Chem. Phys.* **93**, 8682 (1990).

[241] K. Schulten, M. Tesch, *Chemical Physics* pp. 441–446 (1991).

[242] M. H. Lee, B. D. Dunietz, E. Geva, *J. Phys. Chem. C* **117**, 23391 (2013).